MULTIPLICITY OF MUON IN $2\,\mathrm{M} \times 2\,\mathrm{M}$ DETECTOR AND CHARGE RATIO OF COSMIC MUON AT MADURAI

By

Suryanarayan Mondal

Enrollment Number: PHYS01201404020

BHABA ATOMIC RESEARCH CENTRE, MUMBAI

A thesis submitted to the
Board of Studies in Physical Sciences

In partial fulfillment of the requirements
for the Degree of

DOCTOR OF PHILOSOPHY

of

HOMI BHABA NATIONAL INSTITUTE

June 28, 2021

Homi Bhabha National Institute

Recommendations of the Viva Voce Board

As members of the Viva Voce Committee, we certify that we have read the dissertation prepared by **Suryanarayan Mondal, entitled "Multiplicity of muon in 2m X 2m detector and charge ratio of cosmic muon at Madurai"** and recommend that it may be accepted as fulfilling the thesis requirement for the award of Degree of Doctor of Philosophy.
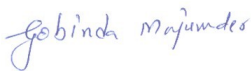
Composition	Name	Signature	Date
Chairman	Amol Dighe		28/06/2021
Guide&Convener	Prashant Shukla		28/06/2021
Co-guide	Gobinda Majumder		28/06/2021
Examiner	Supriya Das		28.06.2021
Member	Subhasish Chattopadhyay		28/06/2021
Member	Supratik Mukhopadhyay		28/06/2021

Final approval and acceptance of this thesis is contingent upon the candidate's submission of the final copies of the thesis to HBNI.

We hereby certify that we have read this thesis prepared under our direction and recommend that it may be accepted as fulfilling the thesis requirement.

Date: June 28, 2021

Place: Mumbai
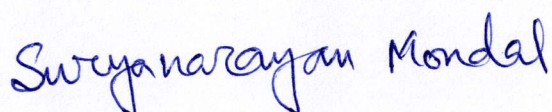
(Co-guide)   **(Guide)**

STATEMENT BY THE AUTHOR

This dissertation has been submitted in partial fulfillment of requirements for an advanced degree at Homi Bhabha National Institute (HBNI) and is deposited in the Library to be made available to borrowers under rules of the HBNI.

Brief quotations from this dissertation are allowable without special permission, provided that accurate acknowledgement of source is made. Requests for permission for extended quotation from or reproduction of this manuscript in whole or in part may be granted by the Competent Authority of HBNI when in his or her judgement the proposed use of the material is in the interests of scholarship. In all other instances, however, permission must be obtained from the author.

Date: June 28, 2021

Place: Mumbai

Suryanarayan Mondal

(Enrolment Number: PHYS01201404020)

DECLARATION

I, hereby declare that the investigation presented in the thesis has been carried out by me. The work is original and has not been submitted earlier as a whole or in part for a degree/diploma at this or any other Institution/University.

Date: June 28, 2021

Place: Mumbai

Suryanarayan Mondal

Suryanarayan Mondal

(Enrolment Number: PHYS01201404020)

LIST OF PUBLICATIONS ARISING FROM THE THESIS

Publications in Refereed Journal:

a. Published:

1) **Suryanarayan Mondal**, V. M. Datar, Gobinda Majumder, N. K. Mondal, K. C. Ravindran and B. Satyanarayana, *Leak test of Resistive Plate Chamber gap by monitoring absolute pressure*, *Journal of Instrumentation, Vol* **14** (April 2019) P04009 DOI: 10.1088/1748-0221/14/04/P04009

2) **Suryanarayan Mondal**, V. M. Datar, Gobinda Majumder, N. K. Mondal, S. Pethuraj, K. C. Ravindran and B. Satyanarayana, *Study of Particle Multiplicity of Cosmic Ray Events using 2 m × 2 m Resistive Plate Chamber Stack at IICHEP-Madurai*, *Experimental Astronomy, Vol*, **51** (19 November 2020) 17–32, DOI: 10.1007/s10686-020-09685-6

Other Publications:

a. Conference/Symposium

1) **S. Mondal**, V. M. Datar, S. D. Kalmani, G. Majumder, N. K. Mondal and B. Satyanarayana, *Leak Rate Estimation of a Resistive Plate Chamber Gap by Monitoring Absolute Pressure in 13th Workshop on Resistive Plate Chambers and Related Detectors (RPC2016)*, *Journal of Instrumentation, Volume* **11** (Nov 2016) C11009

2) **Suryanarayan Mondal**, V. M. Datar, S. D. Kalmani, G. Majumder, N. K. Mondal and B. Satyanarayana, *Estimation of Leak of a Resistive Plate Chamber by Monitoring Absolute Pressure in XXII DAE High Energy Physics Symposium*, *Springer Proceedings in Physics, Volume* **203** (May 2018) 851–853

3) **Suryanarayan Mondal**, V. M. Datar, Gobinda Majumder, N. K. Mondal, S. Pethuraj, K. C. Ravindran and B. Satyanarayana, *Study of Particle Multiplicity by 2 m × 2 m Resistive Plate Chamber Stack at IICHEP-Madurai in XXIII DAE High Energy Physics Symposium*, *Springer Proceedings in Physics, Volume* **261** (May 2021) 1155–1158

4) G. Majumder and **S. Mondal**, *Design, construction and performance of magnetised mini-ICAL detector module in The 39th International Conference on High Energy Physics (ICHEP2018), Proceedings of Science, Volume* **340** (2019) 360

5) S. Pethuraj, V. M. Datar, S. D. Kalmani, G. Majumder, N. K. Mondal, **S. Mondal**, P. Nagaraj, Pathaleswar, K. C. Ravindran, M. N. Saraf, B. Satyanarayana, R. R. Shinde, Dipankar Sil, S. H. Thoker, S. S. Upadhya, P. Verma and E. Yuvaraj, *Measurement of Angular Distribution and Integrated Flux of Cosmic Ray Muons Using 2 m × 2 m RPC Stack at IICHEP Madurai in XXII DAE High Energy Physics Symposium, Springer Proceedings in Physics, Volume* **203** (2018) 845–846

6) G. Majumder, V. M. Datar, S. D. Kalmani, N. K. Mondal, **S. Mondal**, B. Satyanarayana and R. R. Shinde, *Development of a Resistive Plate Chamber with Heat Strengthened Glass in XXII DAE High Energy Physics Symposium, Springer Proceedings in Physics, Volume* **203** (2018) 575–578

7) G. Majumder, V. M. Datar, S. D. Kalmani, N. K. Mondal, **S. Mondal**, B. Satyanarayana and R. R. Shinde, *Development of a Resistive Plate Chamber with heat strengthened glass in 13th Workshop on Resistive Plate Chambers and Related Detectors (RPC2016), Journal of Instrumentation, Volume* **11** (2016) C09019

8) S. D. Kalmani, **S. Mondal**, R. R. Shinde and P. V. Hunagund, *Some Studies Using Capillary for Flow Control in a Closed Loop Gas Recirculation System in XXII DAE High Energy Physics Symposium, Springer Proceedings in Physic, Volume* **203** (2018) 913–915

Date: June 28, 2021

Place: Mumbai

Suryanarayan Mondal

Suryanarayan Mondal

(Enrolment Number: PHYS01201404020)

ACKNOWLEDGEMENTS

DEDICATED TO...

Mother

Contents

List of Tables

List of Figures

SUMMARY

The 50 kton INO-ICAL [1] is a proposed underground high energy physics experiment at Theni, India (9°57′ N, 77°16′ E) to study the neutrino oscillation parameters using atmospheric neutrinos. The Resistive Plate Chamber (RPC) has been chosen as the active detector element for the ICAL detector, interspersed with 5.6 cm thick iron plates. Approximately 30000 RPC gaps of dimension $2\,\text{m} \times 2\,\text{m}$ will be placed in between the 151 layers of iron plates. The iron plates will be magnetised up-to about 1.5 Tesla. The detector will be housed inside a cavern under a rock overburden of 1 km to reduce the atmospheric muon background. The ICAL will search mainly for ν_μ induced charged current interactions in the iron target. The primary aim of the experiment is to determine the sign of the mass-squared difference $\Delta m^2_{32} \left(= m^2_3 - m^2_2\right)$ using matter effects. The ICAL detector can also be used to probe the value of leptonic CP-phase $\left(\delta_{cp}\right)$ and last but not the least to search for physics beyond the standard model using neutrino oscillations.

The INO Project is proposed to operate at-least for 20 years. Various tests are performed during and after production of the RPCs to arrest the ageing of RPCs. The RPCs are going to be operated in avalanche mode with a gas mixture of R134a (95.2%), iso-C_4H_{10} (4.5%) and SF_6 (0.3%). During the active operation of the ICAL detector, ~200,000 litres of the gas mixtures will be circulating inside the 30,000 RPCs. Any contamination leaking inside the RPCs as well as leaking of the gas mixture outside, can affect the performance of the detector. Due to this, a proper leak test has to be performed on all the glass gaps at the time of production as well as during operation and a proper gas monitoring system for the Closed-loop System has to be implemented to detect impurities in the gas-mixture during operation. The leak-test setups, both wired and wireless, are operational and are being used at various facilities and industries working along with INO-Collaboration and with the help of the prepared document even a novice can test a large number of RPCs in a short time. The knowledge gained in this study also gives us more opportunity to better understand the structural integrity of the glass RPCs against various atmospheric parameters.

As a part of the ICAL R&D program, a 12 layer stack of $2\,\text{m} \times 2\,\text{m}$ Resistive Plate Chambers (RPCs) with an inter-layer gap of 16 cm has been operational at IICHEP, Madurai since the

last few years to study the cosmic ray muons. The data obtained by this setup is also used to study the flux and angular distribution of muons with the help of an extreme air shower (EAS) simulation program and detector simulation program. To further test the capability of the Simulation Packages, the charged-particle multiplicity in the obtained data is compared with it with the air shower simulation. The results of the current study reflect that the current physics models of interactions at the Earth's atmosphere are unable to reproduce the air showers accurately. The earlier measurements of muon multiplicity which also showed more muon multiplicity in data along with the present result can be used to improve the parameters of the hadronic model at high energies and/or cosmic ray spectral index.

The study of atmospheric muon charge ratio $\left(R_\mu = N_{\mu^+}/N_{\mu^-}\right)$ is important to the measurement of the neutrino flux precisely, alongside the relevant information in the composition of the primary cosmic rays and the different mechanisms of particle physics. One of the main aspects of ICAL detector is to distinguish between the μ^+ and μ^- passing through the magnetised iron medium, which in turns helps in determining the mass-hierarchy of the neutrinos. As a part of the ICAL R&D program, a magnetised detector (mini-ICAL) with 10 layers of RPCs has been built and operational at IICHEP, Madurai situated near the INO site. Being a scale-down model of the ICAL detector, the mini-ICAL is being studied as the prototype of the magnetised ICAL. The cosmic ray data collected by the detector setup is also used to calculate the charge ratio (R) of the number of μ^+ to μ^- arriving at the Earth's surface. The testing of the reconstruction algorithms is also another motivation behind this study. By comparing the result from cosmic ray data with extreme air shower (EAS) simulation, this study also signifies the ability of the magnet in identifying the charge of the particle. From the study, it is seen that the ratio more or less matches in the range of 0.8-3 GeV with BESS-TeV'02 calculation [2]. A new detector setup, named as Engineering Module is going to be built in the near future with 20 layers of RPCs where the momentum should be reconstructed up-to ~12 GeV.

Chapter 1

Introduction

In this chapter, we are going to recapitulate the concept of the neutrinos (ν) and the experimental milestones placed so far on the path of understanding of this elusive particle. This chapter also focuses briefly on the India-based Neutrino Observatory (INO), an effort to dive into the mysteries of the neutrinos.

1.1 Neutrinos

The road to the neutrino[3], even though the existence of it was unknown at the beginning, started with the discovery of radioactivity by Henri Becquerel in 1896[4], followed by the identification of the β-particle by Ernest Rutherford in 1899[5]. After that, it took almost 30 years to establish the fact that the energy spectrum of the electrons emitted in the β-decay is continuous, confirmed with the results published by Charles Drummond Ellis and William Alfred Wooster in 1927[6]. In 1929, Meitner and Wilhelm Orthmann verified the results published by Ellis and William with improved apparatus[7], and then Meitner wrote to Ellis, "We have verified your results completely. .... But I do not understand this result at all."[8] To explain the continuous energy spectrum of the electron in the β-decay, in 1930, Wolfgang Pauli's 'desperate way out' was the suggestion of a very light, neutral and spin $^1/_2$ particle emitted along with the electron that became known as the neutrino. This did not contradict with the law of energy, momentum and spin conservation. Convinced by this, Enrico Fermi incorporated the putative neutrino into a successful theory of β-decay. Finally, in 1956, Frederick Reines and Clyde Cowan delivered

the experimental evidence of the existence of the neutrino (or the Poltergeist, as Reines called it) by observing the inverse β-decay, $p + \bar{\nu}_e = e^+ + n$, in the high neutrino flux near a reactor[9]. The discovery of the ν_μ and ν_τ were made at the Brookhaven National Accelerator Laboratory in 1962[10] and at the DONuT collaboration in 2000[11], respectively.

The neutrinos are the second most abundant particles in the known universe, after the photon. They are till now known to exist in three different flavours, verified experimentally in e^+e^--collisions[12], named the electron neutrino (ν_e), the muon neutrino $\left(\nu_\mu\right)$ and the tau neutrino (ν_τ).

1.1.1   Neutrinos in the Standard Model

The Standard Model (SM) of Particle Physics, formulated by S. Glashow, S. Weinberg and A. Salam, represents the descriptions of the elementary particles and the fundamental forces in nature (except gravitational force)[13, 14, 15]. The model is based on $\mathrm{SU}(2) \times \mathrm{U}(1)$ gauge theory which speculated the existence of the weak neutral currents[16]. The discovery of the neutral current neutrino interactions in 1973 by the Gargamelle experiment at CERN delivered the validation of the Standard Model[17, 18, 19], which is also confirmed by Fermilab independently[20]. According to the SM, the fundamental building blocks of the observable universe are made of 12 fermions with spin $\frac{1}{2}$ (6 leptons and 6 quarks) and their anti-particles. The fermions interact between each other via 4 gauge bosons with spin 1 which are called as carriers of interactions. These particles were discovered in various experiments around the world. The most interesting discovery which relates directly to the neutrinos is the measurement of the invisible decay width of Z boson, performed accurately by the LEP experiment at CERN[12]. This measurement has constrained the number of neutrino flavours to three with satisfactory uncertainty.

According to the Standard Model, all the fermions acquire masses via the Higgs mechanism. A fermion mass term thus must require a coupling of the left-handed and the right-handed fields. As the neutrinos have left-handed helicity and the anti-neutrinos have right-handed helicity, the SM neutrinos are massless and they favour leptonic number conservation. However, the neutrino experiments have strongly settled the phenomenon of the neutrino flavour mix-

ing (also called as the neutrino oscillations) which confirms the masses of the neutrinos to be non-zero. Hence, the understanding of the mechanism via which the neutrinos gain masses, as well as the neutrino oscillations are beyond the scope of the Standard Model. Therefore, the neutrinos are very crucial objects to solve the puzzles of the new physics lying beyond the Standard Model.

1.1.2 Neutrino Interactions

The neutrinos are weakly interacting particles, which means that they only interact via $W^\pm$ and Z^0 bosons and the interactions are called charged-current (CC) and neutral-current (NC) interactions, respectively. As the $W^\pm$ and Z^0 are much heavier members in the family of inter-mediating particles, the "week interactions" which means that the probability of interaction is very less.

In CC interactions, the neutrino exchanges charge with a nucleon via $W^\pm$ and turns into a charged lepton associated with the neutrino. When a high energetic neutrino interacts with the nucleons, the gluons inside the nucleons also takes part in the interactions, which leads to the productions of one or many hadrons, apart from the charged lepton. Unlike CC interactions, the charged leptons are absent in the final state in the case of NC interactions. In an experiment, the presence of the charged leptons in the final state distinguishes between CC and NC events.

1.1.3 Sources of Neutrinos

The neutrinos are produced at numerous different sources, both man-made and natural, over a wide-range of energy. The estimated abundance of neutrinos from different sources can be found in the Figure 1.1.

The neutrinos in the energy range of μeV to meV or the so-called "relic" neutrinos are understood to originate at the big-bang nucleosynthesis [22]. The neutrinos originated in the sun[23], the supernovas, the the Earth[24, 25] and the nuclear reactors are of the energy range of keV to MeV. The neutrinos, being produced by the interaction of cosmic rays with atmosphere, have energies ranging from MeV to TeV. The neutrinos produced at supernova remnants, gamma-ray bursts, active galactic nuclei and from interactions of ultra-energetic cosmic
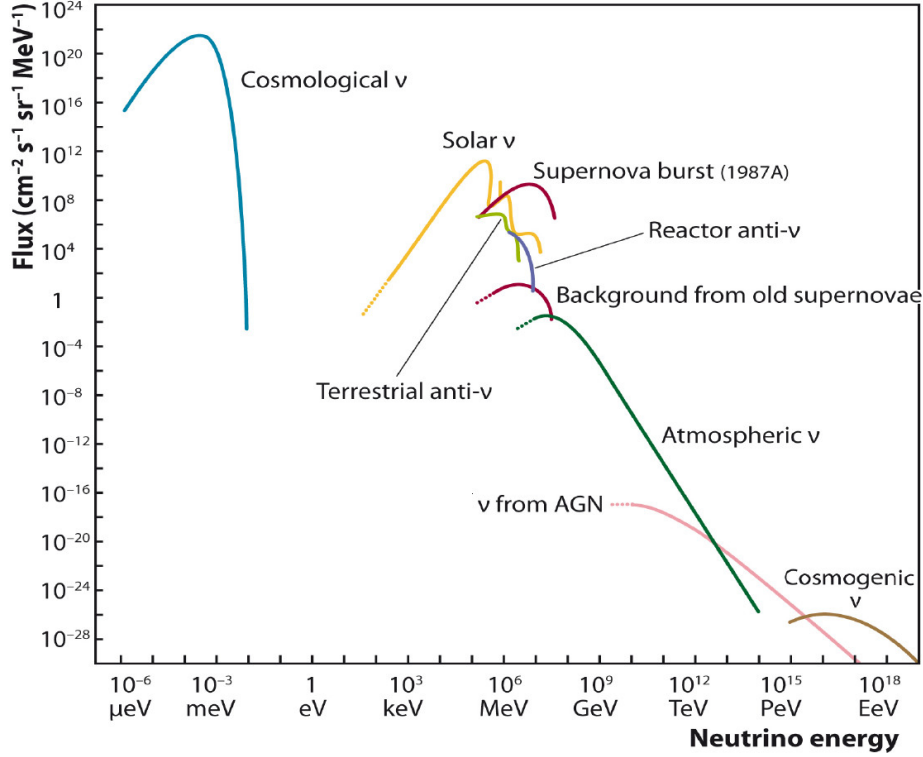
Figure 1.1: Predicted flux of neutrinos from different sources [21].

rays with cosmic microwave background occupy the higher range of energies.

A few sources being studied in the different experiments are discussed in the following.

- **Solar Neutrinos:** The sun is the most abundant source of the electron neutrinos. The Standard Solar Model (SSM)[26] predicts the production of the neutrinos to be occurring through the exothermic nuclear fusion at the core of the sun mainly in two processes: (i) proton-proton (pp) cycle and (ii) carbon-nitrogen-oxygen (CNO) cycle.

  The Solar neutrinos detected at the Earth serve as the direct telescope to the core of the sun.

- **Atmospheric Neutrinos:** The atmosphere of the Earth is exposed to high energetic primary cosmic rays originating in outer space. These cosmic rays consist of mostly protons with a smaller fraction of higher Z-Nuclei elements[27]. The energy spectrum of the primary cosmic rays follows a power-law, $E^{-\gamma}$ where $\gamma \simeq 2.7$ for sub-TeV energy and 3 for beyond. The incoming cosmic rays interact with the constituents of the atmosphere producing showers of secondary particles. The secondaries are consisting mainly of pions $\left(\pi^{\pm,0}\right)$ and kaons ($K^{\pm}$). The neutral pions mainly decay via electro-magnetic in-

teractions, $\pi^0 \rightarrow \gamma + \gamma$ whereas the charged pions decay to muons and neutrinos via weak-interactions, $\pi^+ \rightarrow \mu^+ + \nu_\mu$ and $\pi^- \rightarrow \mu^- + \bar{\nu}_\mu$. The resultant muons may also decay into electrons and neutrinos, $\mu^+ \rightarrow e^+ + \nu_e + \bar{\nu}_\mu$ and $\mu^- \rightarrow e^- + \bar{\nu}_e + \nu_\mu$. The kaons also decay to muons and neutrino and to pions in different branching fractions, but this contribution to the atmospheric neutrino flux (Φ) is small compared to the pions. The production of (ν_τ) is negligible in the atmosphere as the production needs mesons with heavier quarks.

The ratio, R, between $N_\mu \left(\propto \Phi\left(\nu_\mu\right) + \Phi\left(\bar{\nu}_\mu\right) \right)$ and $N_e \left(\propto \Phi\left(\nu_e\right) + \Phi\left(\bar{\nu}_e\right) \right)$ is predicted to be around 2, near the surface of the Earth. The value of R increases with energy as muons with high energy reach the surface of the Earth before decaying.

The plentiful atmospheric neutrinos, for its wide range of energy and for being 'cost-free', are very important in the field of neutrino research.

- **Reactor Neutrinos:** The fission reactions of heavy nuclei like U^{235}, U^{238}, P^{239}, P^{241}, etc. produce $\bar{\nu}_e$ through the process of β-decay in the reactor cores. As the reactor neutrinos derive their energy from these fission reaction, the energy of these $\bar{\nu}_e$s are in the MeV range, typically within 2-3 MeV with a significant tail till about 8 MeV.

  The high flux of neutrinos near a reactor provides a brilliant experimental scope of studying the properties of neutrinos. So, the importance of the reactor neutrinos dates back to the experiment by Reines and Cowan which provided the first experimental evidence of the existence of the neutrinos.

- **Accelerator Neutrinos:** Accelerator neutrinos are produced at large scale particle accelerators. When a high energy proton beam collides with a heavy nuclei target, a bunch of pions and kaons are produced. These pions and kaons eventually decay into neutrinos, electrons/muons and mesons. There are long shields placed before the detector to filter the mesons from the neutrino beam. Mainly, $\bar{\nu}_\mu$s and ν_μ are produced at the accelerators, but the beam may get contaminated by the production of $\bar{\nu}_e$ and ν_e from the decay of a certain fraction of kaons. By the selection and manipulation of the beam of pions and kaons, proper control on neutrino type and energy can be achieved, making the accelera-

tor neutrinos one of the vital source for the detailed study of neutrino phenomenon.

1.1.4   Neutrino Oscillations

The pioneer work by Bruno Pontecorvo was neutrino-antineutrino oscillation[28, 29]. The neutrino oscillation in the two generations was first proposed by Maki, Nakagawa and Sakata[30]. The neutrino oscillation is of great theoretical and experimental interest as it implies that neutrino has non-zero mass, which leads to modification of the Standard Model of particle physics. The neutrino oscillations occur due to the mixing of the flavour eigenstates and mass eigenstates of neutrinos. The visual flavour eigenstates ($|\nu_\alpha\rangle$; $\alpha = e, \mu, \tau$) can be expressed as a linear combination of the mass eigenstates $\left(|\nu_j\rangle$ with mass m_j; $j = 1, 2, 3\right)$ as shown in the following equation.

$$|\nu_\alpha\rangle = \sum_j U_{\alpha j} |\nu_j\rangle \tag{1.1}$$

The unitary mixing matrix, U, called the PMNS matrix, is named after Pontecorvo, Maki, Nakagawa and Sakata. The mixing of three flavours of neutrinos can be defined with 3 mixing angles and 6 phases. Five of the phases can be absorbed into fermion fields in the Kobayashi-Maskawa mechanism[31]. Only one phase has an effect which leads to CP Violation in neutrino oscillations. In the case of neutrino being a Majorana particle, two more phases are introduced, although the measurement of neutrino oscillation is not sensitive to the Majorana phases.

The mixing matrix with mixing angles (θ_{12}, θ_{23} and θ_{13}), mixing phase (δ_{CP}) and Majorana phases (α_{21} and α_{31}) is represented in the following,

$$U_{PMNS} = \underbrace{\begin{bmatrix} 1 & 0 & 0 \\ 0 & c_{23} & s_{23} \\ 0 & -s_{23} & c_{23} \end{bmatrix}}_{\text{Atmospheric } (\theta_{23} \sim 48°)} \underbrace{\begin{bmatrix} c_{13} & 0 & s_{13}e^{-i\delta_{CP}} \\ 0 & 1 & 0 \\ -s_{13}e^{i\delta_{CP}} & 0 & c_{13} \end{bmatrix}}_{\text{Reactor } (\theta_{13} \sim 8.5°)} \underbrace{\begin{bmatrix} c_{12} & s_{12} & 0 \\ -s_{12} & c_{12} & 0 \\ 0 & 0 & 1 \end{bmatrix}}_{\text{Solar } (\theta_{12} \sim 34°)} \begin{bmatrix} 1 & 0 & 0 \\ 0 & e^{\frac{i\alpha_{21}}{2}} & 0 \\ 0 & 0 & e^{\frac{i\alpha_{31}}{2}} \end{bmatrix} \tag{1.2}$$

where, $c_{jk} = \cos\theta_{jk}$ and $s_{jk} = \sin\theta_{jk}$.

The time evolution of the states in equation 1.1 is given by the following equation,

$$|\nu_\alpha(t)\rangle = \sum_j U_{\alpha j} e^{-iE_j t} |\nu_j\rangle \tag{1.3}$$

where, E_j is the energy eigenvalues correspond to the vacuum propagation Hamiltonian (H_0).

The probability of oscillating from the flavour state ν_α to the state ν_β is given in the following equation,

$$P_{\nu_\alpha \to \nu_\beta}(t) = \left|\langle \nu_\beta | \nu_\alpha(t)\rangle\right|^2 = \sum_{j,k} U_{\alpha j} U_{\beta j}^* U_{\alpha k}^* U_{\beta k} e^{-i(E_j - E_k)t}. \tag{1.4}$$

If $\nu_\alpha = \nu_\beta$, then P is called the 'survival probability', and 'oscillation probability' if otherwise.

The equation 1.4 also can be expressed in the following form,

$$P_{\nu_\alpha \to \nu_\beta}(L) = \delta_{\alpha\beta} - 4\sum_{j>k} \Re\left[U_{\alpha j} U_{\beta j}^* U_{\alpha k}^* U_{\beta k}\right] \sin^2\left(\frac{\Delta m_{jk}^2 L}{4E}\right)$$
$$+ 2\sum_{j>k} \Im\left[U_{\alpha j} U_{\beta j}^* U_{\alpha k}^* U_{\beta k}\right] \sin\left(\frac{\Delta m_{jk}^2 L}{2E}\right) \tag{1.5}$$

where, $\Delta m_{jk}^2 = m_j^2 - m_k^2$, L is the total distance travelled and E is the neutrino energy.

The oscillation probability for the anti-neutrinos thus given by

$$P_{\bar{\nu}_\alpha \to \bar{\nu}_\beta}(L) = \delta_{\alpha\beta} - 4\sum_{j>k} \Re\left[U_{\alpha j}^* U_{\beta j} U_{\alpha k} U_{\beta k}^*\right] \sin^2\left(\frac{\Delta m_{jk}^2 L}{4E}\right)$$
$$+ 2\sum_{j>k} \Im\left[U_{\alpha j}^* U_{\beta j} U_{\alpha k} U_{\beta k}^*\right] \sin\left(\frac{\Delta m_{jk}^2 L}{2E}\right). \tag{1.6}$$

The equations 1.5 and 1.6 show that the neutrino oscillations can only exist if the masses of neutrinos are non-zero. It is also seen that the real parts of the equations 1.5 and 1.6 are CP invariant. So, the CP asymmetry can be interpreted as,

$$P_{\nu_\alpha \to \nu_\beta}(L) - P_{\bar{\nu}_\alpha \to \bar{\nu}_\beta}(L) = 4\sum_{j>k} \Im\left[U_{\alpha j} U_{\beta j}^* U_{\alpha k}^* U_{\beta k}\right] \sin\left(\frac{\Delta m_{jk}^2 L}{2E}\right). \tag{1.7}$$

It is to be noted that the equation 1.7 does not provide any resolution about the sign of the Δm_{jk}^2s or the absolute values of m_js.

• **Neutrino Oscillations in Matter**

When neutrinos pass through matter, then probabilities of oscillations can also be altered due to the 'matter-effect'. The neutrinos face coherent forward scattering with the electrons, protons and neutrons present in the matter [32]. The potential arising due to this effect modifies the vacuum propagation Hamiltonian (H_0), affecting the mixing of neutrinos.

This phenomenon of altering neutrino flavour during propagation in the matter was introduced by Mikhaev, Smirnov and Wolfenstein (MSW)[33]. The ν_es have both CC with electrons and NC elastic scattering interactions with electrons, protons, neutrons present in matter, but the ν_μs and ν_τs have only NC interactions with matter. In matter, the number of protons and electrons are the same, thus their contributions in neutral current are cancelled out. The potential V_{NC} is experienced by all three flavours. The additional CC interactions account for an extra potential V_{CC}. Hence, the matter Hamiltonian is given as,

$$H_{\mathrm{m}} = H_0 + V_{\mathrm{m}} \tag{1.8}$$

where, V_{m} is represented as,

$$V_{\mathrm{m}} = \begin{bmatrix} V_{\mathrm{CC}} + V_{\mathrm{NC}} & 0 & 0 \\ 0 & V_{\mathrm{NC}} & 0 \\ 0 & 0 & V_{\mathrm{NC}} \end{bmatrix}. \tag{1.9}$$

where, $V_{\mathrm{CC}} = \sqrt{2}G_{\mathrm{F}}n_e$ and $V_{\mathrm{NC}} = -\frac{1}{\sqrt{2}}G_{\mathrm{F}}n_n$ are called the effective potentials. Here, n_e and n_n are the number densities of electrons and neutrons, respectively and G_{F} is the Fermi coupling constant. The normalised eigenvectors of the diagonalised matter Hamiltonian form the modified mixing matrix. Thus, the effective mass-squared differences and mixing angles can be computed in matter. If two flavour mixing is considered, the matter affected mass-squared difference $\left(\Delta m_m^2\right)$ and mixing angle (θ_m) are given by,

$$\tan 2\theta_m = \frac{\Delta m^2 \sin 2\theta}{\Delta m^2 \cos 2\theta - A} \quad \text{and} \quad \Delta m_m^2 = \sqrt{\left(\Delta m^2 \cos 2\theta - A\right)^2 + \left(\Delta m^2 \sin 2\theta\right)^2} \tag{1.10}$$

where, $A = 2\sqrt{2}G_F n_e E$ for neutrinos and $A = -2\sqrt{2}G_F n_e E$ for anti-neutrinos. Here, some points are to be noted.

- Assumption of $n_e \to 0$ in the equation 1.10 makes the matter affected mass-squared difference and mixing angle the same as those are in the vacuum. This means that the values of the mass-squared differences and the mixing angles from vacuum remain unchanged in matter.

- If $n_e \to \infty$ and $\theta \neq 0$, then $\theta_m \to \frac{\pi}{2}$. Hence, even if the vacuum mixing angle is very small, maximum mixing of neutrino can be observed in matter.

- When $A = \Delta m^2 \cos 2\theta$, then the value of θ_m goes to $\frac{\pi}{4}$. This phenomenon is called the MSW resonance effect. The neutrinos going through MSW resonance have the maximal probability of changing its flavour. Depending on whether the value of Δm^2 is positive or negative, the resonance occurs for the neutrinos or anti-neutrinos, respectively.

For three flavours mixing or in the case of non-uniform matter density, the oscillation probabilities are required to be calculated numerically.

The survival probability of solar neutrinos and predicted by MSW theory and confirmed by several experiments [34, 35, 36, 37, 38, 24]. The positive sign of δm_{21}^2 was confirmed from the observation of resonance oscillation of solar neutrino, but the sign of Δm_{32}^2 is still unknown. Thus, two different mass-ordering of the neutrinos are possible: (i) $m_1 < m_2 < m_3$ called as normal hierarchy (NH) or normal ordering (NO) and (ii) $m_3 < m_1 < m_2$ called inverted hierarchy (IH) or inverted ordering (IO).

1.1.5   Status of Neutrino Oscillations Parameters

Many experiments worldwide are in constant effort to improve the best-fit values of the oscillation parameters. The detailed summary on the oscillation parameters from the global analysis, updated in 2018, can be found in [39].

The best-fit values of mixing angles are reported as $\theta_{12} \sim 34°$, $\theta_{23} \sim 48°$ and $\theta_{13} \sim 8.5°$ along with the mass-squared differences as $\Delta m_{21}^2 \sim 7.5 \times 10^{-5}\,\text{eV}^2$, $\left|\Delta m_{31}^2\right| \sim 2.5 \times 10^{-3}\,\text{eV}^2$.[1]

---

[1]Please refer to [39] for the current accepted/updated values of the oscillations parameters with the uncertainties.

The global analysis have found preference for the value of δ_{CP} in the range between π and 2π at more than 4σ[39]. The current combined analysis prefers the octant of θ_{23} to be the second octant, slightly. Most interestingly for the first time, the global analysis favours the normal mass ordering over the inverted one at 3.4σ[39].

1.1.6 Study of the Atmospheric Neutrinos

Unlike the reactor-based or accelerator-based neutrino experiments, the atmospheric neutrino detectors are not limited by the fixed-length (L) between the detector and source of neutrinos or by the narrow range of energy (E). The detectors for atmospheric neutrinos are usually built under a depth of the Earth's surface to reduce the cosmic muon background. Thus, the distances travelled by the neutrinos detected in these detectors vary up-to a distance equivalent to the Earth's diameter ($\sim 12000\,\mathrm{km}$) after being produced in the atmosphere. Moreover, the energy of the atmospheric neutrinos ranges from hundreds of MeV to TeV. This qualifies the atmospheric neutrino detectors to study the neutrinos over widely varying baselines ranging upto the diameter of the Earth.

There have been two types of detectors commissioned in atmospheric neutrino research, till date; water Cherenkov detectors and tracking calorimeter detectors. The INO-ICAL which belongs to the latter type is discussed in the next section.

1.2 The India-based Neutrino Observatory

The India-based Neutrino Observatory (INO)[1, 40] is a multi-institutional effort to build an underground laboratory to study atmospheric neutrinos. The proposed observatory will be located at West Bodi Hills near Pottipuram Village (9°57′36″ N, 77°16′24″ E). The detectors will be housed inside several caverns with an overburden of ~1 km rock in order to reduce the background due to cosmic muons produced along with the neutrinos. One big cavern will encase the Iron CALorimeter (ICAL) along with several small caverns facilitating a few daughter experiments.

1.2.1   Physics Aspects of INO-ICAL

The ICAL is primarily designed to observe the charged-current interactions of the $\nu_\mu/\bar{\nu}_\mu$s with the ability to distinguish between the charged leptons, mainly μ^+ and μ^-, which are being produced in the interactions. This ability gives ICAL advantage to study matter-effect in details and hence to determine the neutrino mass ordering. The baselines of ICAL vary up-to $\sim 10000\,$km with wide range of energy from hundreds of MeV to TeV, which also makes ICAL suited for precise measurement of atmospheric oscillation parameters.

1.2.2   The ICAL Detector

The ICAL detector, with a target medium of $\sim 50\,$kton iron, is a magnetised calorimeter designed to detect the charge and momentum of the leptons, mainly $\mu^\pm$, produced by the CC interactions by $\nu_\mu/\bar{\nu}_\mu$ with detector volume. The Resistive Plate Chamber (RPC) has been chosen as the active detector element for the ICAL detector, interspersed with 5.6 cm thick iron plates. Approximately 30000 RPC gaps of dimension $2\,\text{m} \times 2\,\text{m}$ will be placed in between the 151 layers of iron plates. The iron plates will be magnetised up-to about 1.5 Tesla. The dimensions of the detector are 48 m, 16 m and 15 m. A schematics of ICAL is shown in the Figure 1.2. A few important constituents of the ICAL detector are discussed below.

• **The Resistive Plate Chamber**

The RPC is basically a gas based parallel-plate detector[41]. The basic components of RPC are shown in the Figure 2.1. The RPC is constructed using two parallel plates of glass having a bulk resistivity of the order of 10^{10}-$10^{12}\,\Omega\,$cm with a gas gap of 2 mm. Uniform spacing between two glass plates is maintained using button spacers. Ideally, the whole chamber has to be leakproof. The outer surfaces of the glass plates are made conductive using graphite coating to form the electrodes where high voltages can be applied. The signal is readout by copper pickup panels on both sides of the RPC. In ICAL detector, the RPCs are going to be operated in avalanche mode with a gas mixture of R134a (95.2%), iso-C_4H_{10} (4.5%) and SF_6 (0.3%). R134a gas acts as a target for the ionising particles passing through the gas gap. The iso-C_4H_{10} absorbs the photons emitted in the recombination processes limiting the formation of secondary
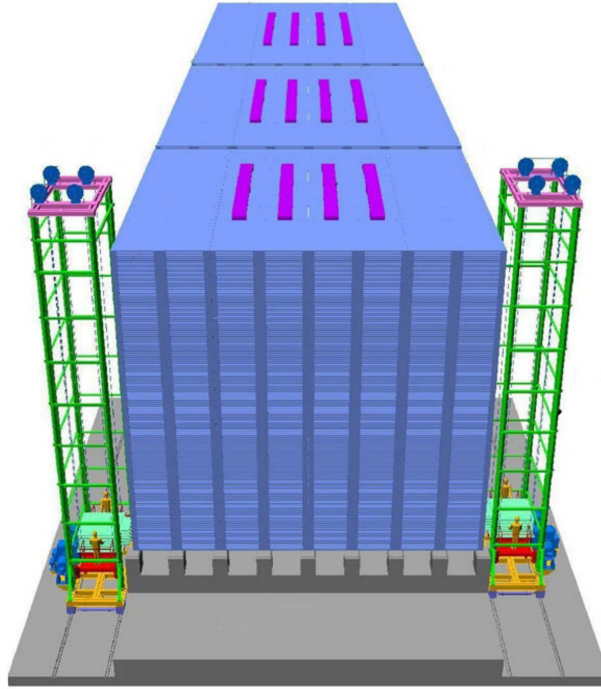
Figure 1.2: A Schematics of the ICAL detector[40].
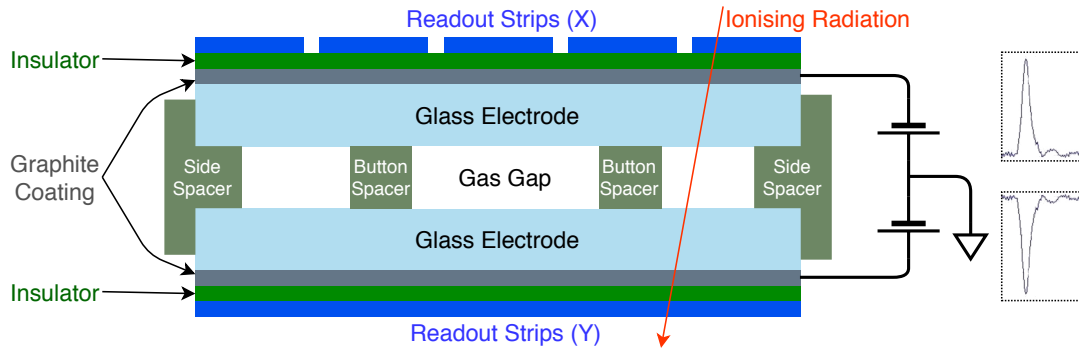
Figure 1.3: Schematic of a Resistive Plate Chamber.

avalanches. SF_6, being an electronegative gas, localises the signal in a small area to have better position resolution.

During the active operation of the ICAL detector, more than 200,000 litres of the gas mixtures will be circulating inside the 30,000 RPCs. To achieve this, a closed-loop gas circulation system (CLS) is designed whose main purpose is to recirculate the gas mixture, minimising wastage of gas which reduces the operational cost.

The RPCs are good charged particle detectors with detection efficiency greater than 95 %. Descent detection efficiency along with the time resolution of ~ 1 ns makes the RPC an excellent component of a tracker-type detector. Also the RPC is cheaper and requires less mainte-

nance than other detectors used in this field of study. Hence, it is advantageous to deploy RPCs in a large scale experiment.

• **The ICAL Magnet**

The iron layers in ICAL serves a dual purpose; as the target for the neutrinos and to carry the solenoidal magnetic field in the detector[42]. The iron carries a magnetic field up to 1.5 Tesla. The particles produced by the interactions of the neutrinos with iron layers propagate in a curved path through the detector. The curvature of the propagation delivers information about the charge and momentum of the propagated particle.

The ICAL is divided into three modules as shown in the Figure 1.4(a). Each of the modules
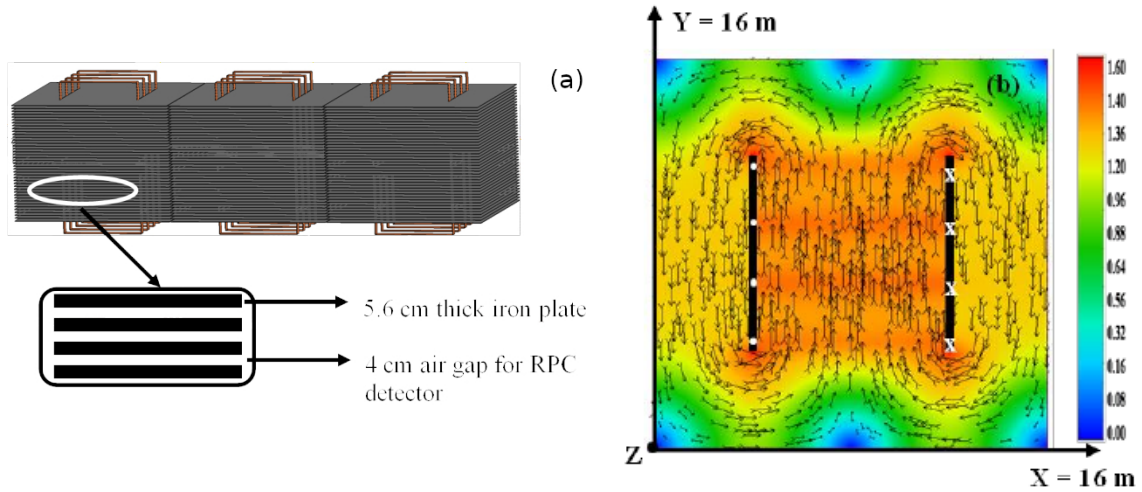
Figure 1.4: (a) A Schematics of the ICAL Magnet and (b) Horizontal Projection of the Magnetic field[42].

will have two vertical slots cut into the module to accommodate the winding of the current-carrying copper coils. The style of the winding makes each of the modules 'shell-type'[43] magnets, thus making the magnetic field toroidal. The horizontal projection of the magnetic field is shown in the Figure 1.4(b).

1.3 Prototype Detector

As the part of the ICAL R&D program, several prototype detector stacks have been built to study the long term stability and performance of the glass RPC detectors using cosmic muons.

The design, fabrication and characterisation of large-size glass RPCs have already been examined and reported[44]. One of the stacks was built at the IICHEP transit campus in Madurai which is shown in the Figure 1.5. This setup is also used as the test-bench for the data acquisition system (DAQ) schemes which are going to be used in ICAL detector. The stack is made

Figure 1.5: Detector Stack with 12 Layers of $2\,\mathrm{m} \times 2\,\mathrm{m}$ RPCs.

of 12 layers of $2\,\mathrm{m} \times 2\,\mathrm{m}$ RPCs with an inter-layer gap of $16\,\mathrm{cm}$.

The detector stack is used intensively to study various properties of the RPCs like strip multiplicities, detector efficiency, detector noise rate, position resolution, time resolution, etc. The stack also allows us to study the cosmic ray muons near the equator of the Earth. The data of the cosmic muons collected using these detectors are analysed to study a few important aspects of cosmic rays. These include the flux of the cosmic ray muons at Madurai[45], magnetic rigidity cutoff for the primary cosmic rays at Madurai, particle multiplicity of secondary cosmic rays at the surface, etc. All of the knowledge gained by studying the data obtained using this detector stack is used as the input parameters for the most realistic Monte-Carlo simulations of the ICAL detector.

1.4   miniICAL

Various tests to study the performance of the magnet assembly are also performed. To study the magnetic field in the detector and the performance of the electronics in the presence of magnetic fringe-field, a detector of the size of $\sim 1/600$ times of ICAL, named miniICAL, is built at IICHEP transit campus in Madurai. The detector consists of 11 layers of soft iron plates of thickness 5.6 cm with an interlayer gap of 4.5 cm. The detector is magnetised using two copper coils with 18 turns each up-to 1.5 T. The RPCs are placed in the interlayer gaps.

The magnetic field profile inside the iron plates is simulated using 2D Simulation with the help of MAGNET6.26 Software[46]. To validate the result from the simulation, the actual measurement of the magnetic field is carried out at several strategic locations of the detector using the help of pick-up coils and hall probes. The atmospheric muon data is recorded in miniICAL and analysed in order to study various detector components. The performance of the RPCs and the supporting electronics are assessed under the influence of the magnetic field.

The atmospheric muons passing through the detector leave tracks in the RPC layers. In the presence of the magnetic field, the muons follow curved trajectories. A suitable reconstruction algorithm is developed to extract the momentum and directional information of the muons from each event. The charge-dependent momentum information of the muons is computed from this and compared with simulation. This current measurement along with the existing phenomenological models can be used to improve the estimation of neutrino flux at the INO Site.

1.5   Chapter Summary

The chapter starts with the brief history of the neutrinos followed by the status of the neutrino oscillations in the global picture. The INO project is then discussed along with its aim to contribute vital physics towards the understanding of neutrinos. A brief discussion is followed afterwards on the RPCs which are being considered as the sensitive detector in the ICAL detector. The construction and the physics potential of the ICAL detector is then discussed. Simultaneously, the scope of the present thesis along with the prototype detectors are highlighted.

Chapter 2

Quality Control of RPCs

The Resistive Plate Chamber (RPC) is chosen as the sensitive detector of the ICAL. The ICAL requires approximately 30000 RPCs to function at its full capacity. The INO Project is proposed to operate for at-least for 20 years. All the RPCs thus must operate without showing any significant ageing during the period of operation. Hence, various tests are performed during and after production of the RPCs.
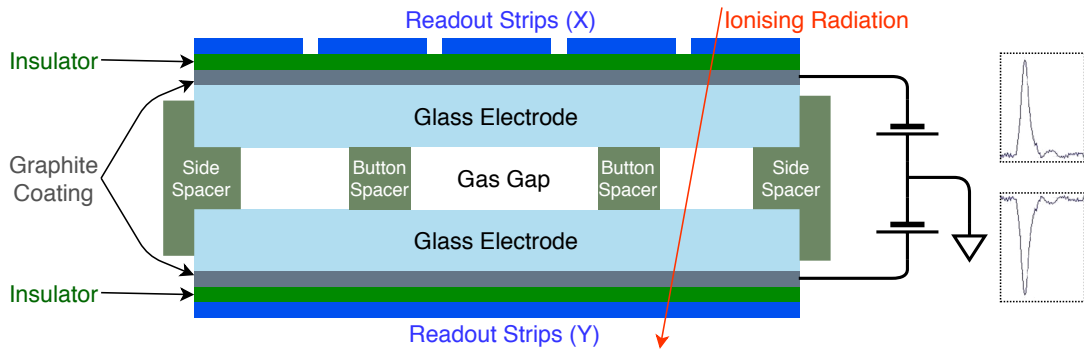
Figure 2.1: Schematic of a Resistive Plate Chamber.

The RPCs that are going to be used in the ICAL are made of glass. The two glass plates, kept at a uniform distance of 2 mm using the help of poly-carbonate buttons, are sealed from four sides to create a leak-tight gas-gap. Both of the outer sides of the gap are coated with semi-resistive graphite paint to form the electrodes where the high voltages can be applied. A mixture of gas is then flown inside the gap via strategically placed nozzles. In the ICAL, the gas mixture is composed of R134a (95.2%), iso-C_4H_{10} (4.5%) and SF_6 (0.3%).[1] The R134a acts

---

[1]R134a is a commercial name of 1,1,1,2-Tetrafluoroethane.

as the target medium for the incident particles. The electrons emitted in the ionisation process initiated by the passing particles create an avalanche under the influence of the applied electric field. The induced signal of the avalanche is then detected by two copper pickup panels on both sides of the gap. The iso-C_4H_{10} act as a photon-quencher which absorbs the emitted photons in the recombination process limiting the formation of secondary avalanches. On the other hand, the SF_6 being an electro-negative gas acts as an electron-quencher which localises the signal within a small area yielding better position resolution.

During the up-time of the ICAL detector, more than 200000 litres of the gas mixture will be circulating inside the 30000 RPCs. A closed-loop gas circulating system (CLS) is designed for this purpose whose main aim is to recirculate the gas mixture, minimising the wastage of gas. The CLS and the plumbings operate at much higher pressure than the atmosphere, but the RPCs are proposed to be operated at an excess pressure of just 10 mmWC above atmospheric pressure. Thus the RPCs pose an additional challenge of keeping the CLS free of contamination because of this little pressure barrier. The leakage of outside atmosphere into the system will introduce water vapour and oxygen inside the RPCs which can increase the risk of damaging the RPCs[47, 48]. The fluorine present in the RPC gas mixture can produce hydrofluoric after reacting with the water vapour during the avalanche. The hydrofluoric acid which is corrosive to glass can damage the inside surface of the gas gaps. On the other hand, the oxygen being an electro-negative in nature can affect the performance of the detector. Due to these reasons, a proper leak test is required to be performed on all the glass gaps during the production as well as the time of operation. Moreover, the impurities in the CLS also needed to be monitored during the operation of ICAL.

2.1   Leak Test of RPCs

To estimate the leakage, the RPC is first pressurised up-to 45 mmWC above the atmospheric pressure and then sealed.[2] The pressure inside the RPC is monitored over a long period. The schematics of a typical leak test setup is shown in the Figure 2.2. A conventional choice of the

---

[2]Millimetres water column, abbreviated to mmH_2O or mmWC, is a unit of pressure. It is the pressure required to support a water column of the specified height. $1\,mmWC \simeq 0.098\,mbar$.
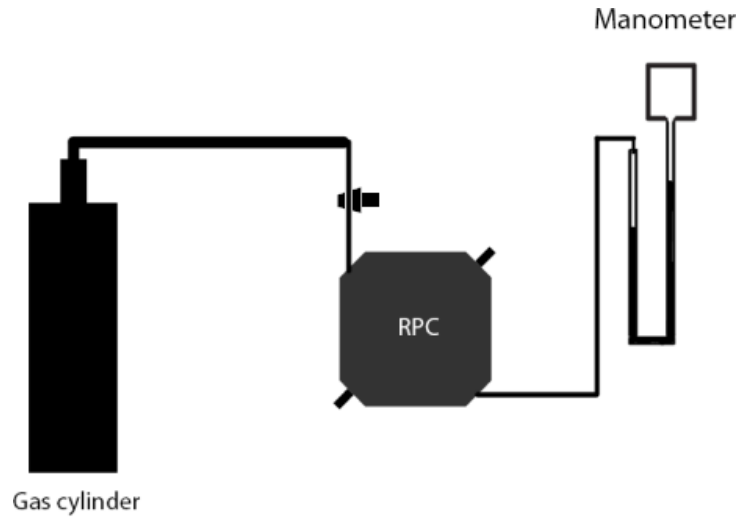
Figure 2.2: Schematics of a typical leak test setup.

sensor to monitor the pressure inside the RPC is the manometer setup as shown in Figure 2.2. Now, the limitation of leak rate estimation using the manometer comes from its observable quantity. The manometer measures the difference between two pressures (ΔP), the atmospheric pressure $\left(P_{\text{rpc}}\right)$ and the RPC pressure (P_{atm}), which can be widely affected by the change of the atmospheric pressure, the room temperature and the volume of the chamber. Hence, the estimation of leak rate using a manometer is only valid in two scenarios, (i) if the atmospheric pressure, the room temperature and the volume of the chamber are kept constant and/or (ii) if the leak rate is very large.

But both the atmospheric pressure and room temperature are constantly affected by the solar atmospheric tides and changes in weather. [3] In the following, it will be established that the volume of the RPC gaps also changes with the variation of the ambient pressure and temperature. Moreover, if the leak from the RPCs is very small then it is nearly impossible to detect.

Hence, a different leak test method along with the test setup is developed to overcome the aforesaid limitations. The setup and technique discussed in the following not only helps to determine whether the RPC is leaking but also allows to estimate the magnitude of the leakage. As the number of the RPCs needed to be tested is large, the setup is required to be simple, portable and cost-effective. The method is also able to test multiple RPCs simultaneously

---

[3]The solar atmospheric tides are generated by the periodic heating of the atmosphere by the Sun. This regular diurnal cycle in heating generates tides in the atmosphere that have periods related to the solar day.
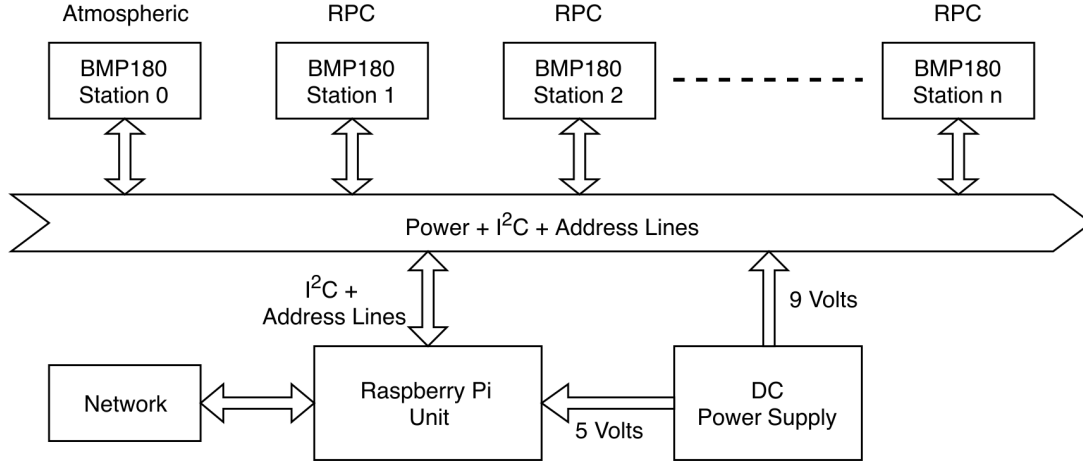
Figure 2.3: Schematics of the 'standalone' leak test setup.

without moving them out of the storage area, which thus limits the possibility of damage to the fragile large glass gaps.

2.1.1 Defining the Leak Rate of RPCs

As per the Poiseuille's law[49], the laminar flow rate of a fluid through a leak path is given in the equation 2.1.

$$\text{(Flow Rate)} = \text{(Leak Constant)} \times \text{(Effective Pressure Difference)} \tag{2.1}$$

where, the *Leak Constant* depends on the path of leakage (i.e. crack, hole, etc) and the viscosity of the gas mixture. The *Leak Constant* quantifies the leakage in the system. The setup and techniques to calculate the *Leak Constant*s for the gas gaps are discussed in the following.

Assuming that the leakage from an RPC is very small, it allows the flow of gas through the leak path to be considered as laminar flow. Also, the variation of ambient pressure and temperature does not affect the viscosity of the gas significantly. The equation 2.1 thus can be used for the case of RPCs.

2.1.2 Experimental Setups

The schematics of the 'standalone' leak-test setup is shown in the Figure 2.3. In this setup, instead of measuring the differential pressure using the conventional manometer, the absolute

(a) Leak Test Module.   (b) Raspberry Pi B & Power Supply Module.

Figure 2.4: Leak Test Setup.

pressure and temperature inside and outside of the gas gap are measured using the sensor module, BMP180 manufactured by BOSCH[50]. The BMP180 is a piezo-resistive sensor having an accuracy of 0.7 mmWC and 0.05 °C in the measurement of pressure and temperature respectively. This sensor is capable of recording data samples for the minimum time interval of 76 ms. The leak test module is shown in the Figure 2.4(a). Each of such modules will record the pressure and temperature for one gas gap. The pressure and temperature data recorded by the module is readout using a *Raspberry Pi v2 B* (Pi) unit[51] shown in the Figure 2.4(b). The data is stored on the on-board memory of the Pi unit. As shown in Figure 2.4(a), each module has two bus ports. This allows to daisy-chain several leak test modules and can be controlled from a single Pi unit.

The common bus mainly consists of Power, Data and Address lines. To avoid the voltage drop in the supply line over a long distance, 9 V DC is supplied from the Pi End and converted to the required voltage at each test module. A 4-bit DIP switch is used on each module to set a unique address for itself. The Pi acquires the data from each station by selecting its unique address. So, only one test module is allowed to communicate with the control unit at a time. As 4-bit address lines are used in this setup, a maximum of fifteen gas gaps can be tested simultaneously. The system is scalable to handle more gas gaps simultaneously, by simply adding more address lines. One of the leak test modules are dedicated to record the ambient pressure and temperature for the test duration.

The data from the BMP180s can also be acquired without wires by microcontrollers equipped with WiFi modules (i.e. NodeMCU module[52]), eliminating the need of the wired common
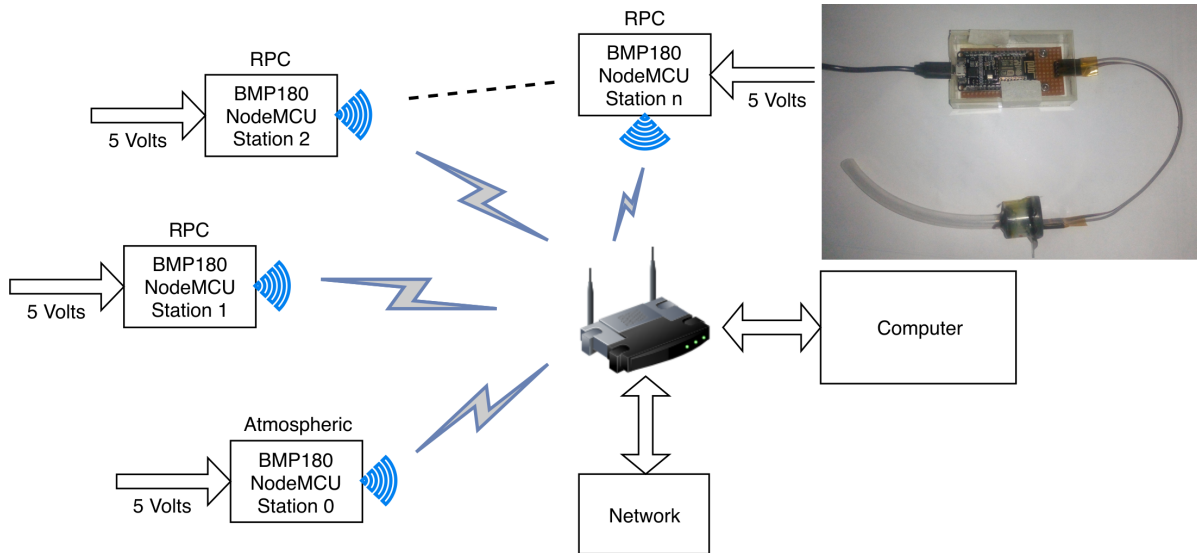
Figure 2.5: Schematics of the WiFi-based leak test setup and one of the test-modules (in the inset).

bus and Pi Unit. One such setup is shown in Figure 2.5. This setup requires an operational WiFi network at the premises to send the data to a computer on the same network. If the network is connected to the internet, then the data can be stored at any remote location also. The test-modules, being low-power devices, can also be powered with small power banks which makes it hugely advantageous while being used at large warehouses. Also, the elimination of the long wires makes this setup immune to electromagnetic interference from other sources. Though this setup is not 'standalone', it is truly scalable which can handle any number of RPC gaps being tested without changing any of the basic design elements.

In the current setup, the pressure and temperature data from each sensor along with the atmospheric pressure and temperature data are recorded continuously with a specified interval of 3 seconds. The final data recorded for a gas gap include the values of the ambient pressure and temperature, the gas gap pressure and temperature and the time stamp for each measurement. The method to quantify the leakage using these data is discussed in the section 2.1.4.

2.1.3   Detection of Button Pop-Ups

The structural stability of the RPC is maintained by the polycarbonate buttons. However, it is observed that sometimes the glue which is used to attach the buttons to the glass plates, fails
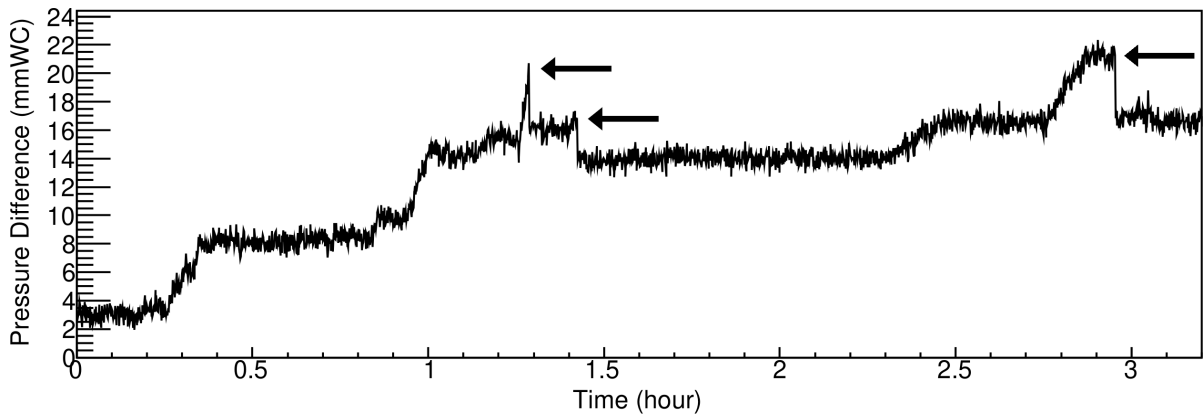
Figure 2.6: Variation of pressure difference with time showing button pop-ups.

to hold under pressure which results in detaching of the buttons from the glass plates.[4] This weakens the structure of RPC. Also during detector operations, this will increase the spacing between the glass plates, thus decreasing the effective electric field resulting in reduced signal strength. Also, for any working RPC, the glue used to attach the buttons to the glass plates must continue to hold under pressure. For any RPC gas gap, even if only one button is not attached, that glass gap will not be suitable to hold more pressure as eventually the glue for more and more buttons will give away, making the gas gap weaker. Hence, it is essential to detect any 'button pop-up' events during the leak test.

With each 'button pop-up' event, the volume of the RPC gap increases which in turn results in a decrease in the pressure inside the gap. Thus the pressure difference between the outside and inside of the gap decreases. In the plot of pressure difference with time, this effect will be observed as a sudden drop in the pressure difference. The Figure 2.6 shows the variation of pressure difference with time for an RPC where there are 'button pop-up' events. It can be observed in the figure that there are three 'button pop-up' events (pointed by arrows) in this RPC and also seen that these 'button pop-up' events result in a decrease in the pressure difference within a very short time. These events cannot be detected with conventional manometers unless the pressure is recorded continuously using a precise differential pressure sensor. Hence, the apparatus, described in the current paper, is very helpful in detecting the 'button pop-up' events during the test.

It is also to be noted that the method to quantify the leakage discussed in the following, fails

---

[4]Hereafter such an event is referred to as 'button pop-up'.

if the data includes button-pop event(s) in it.

2.1.4   Leak Rate Calculation

The variation of temperature of the gas gap and variation of pressure in the gas gap as well as

atmosphere respectively with time are illustrated in the Figure 2.7(a) and 2.7(b). The periodic
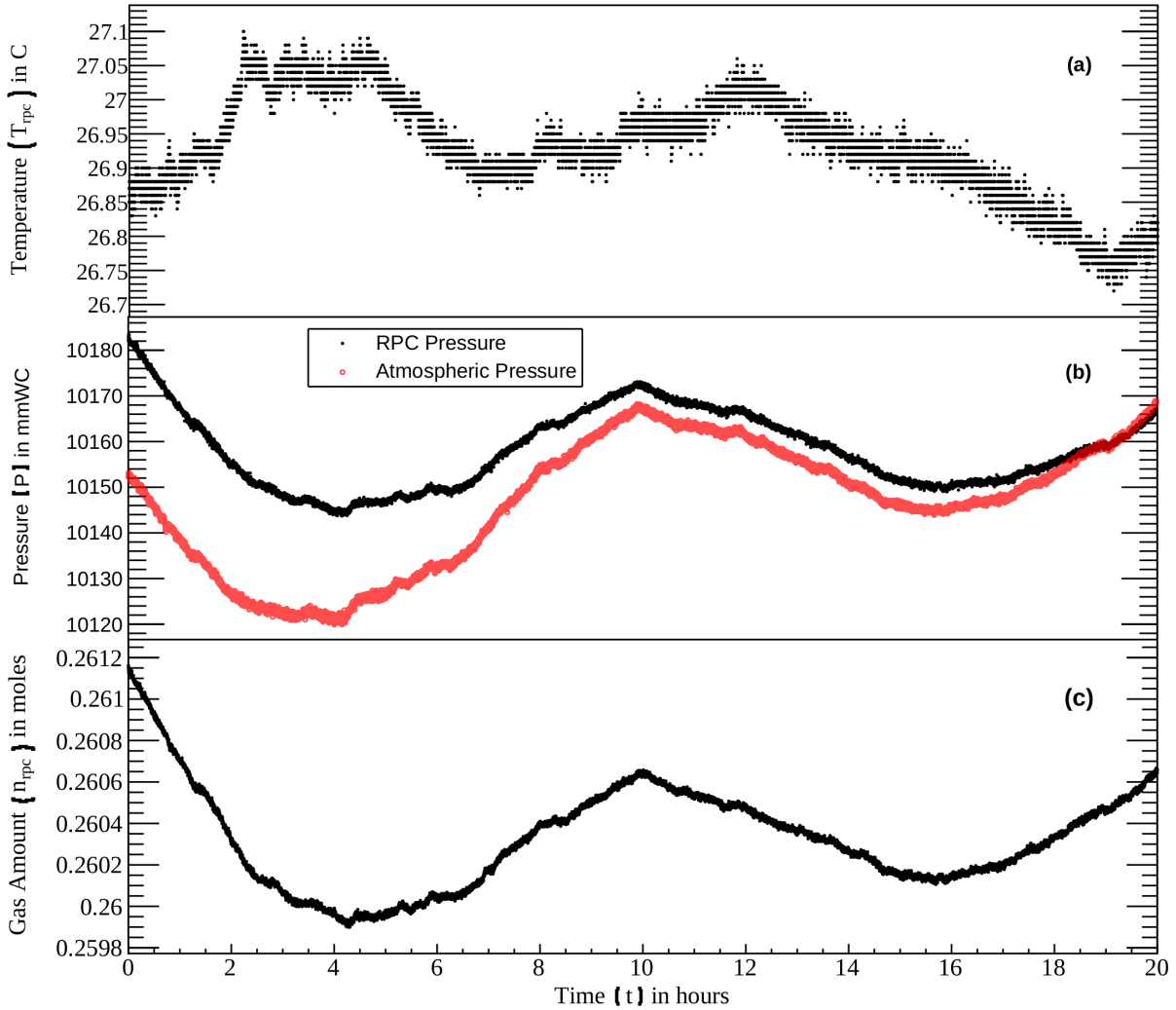
Figure 2.7:   **(a)** Variation of temperature $\left(T_{\mathrm{rpc}}\right)$ with time, **(b)** Variation of atmospheric (P_{atm} : Black) and RPC $\left(P_{\mathrm{rpc}}$: Red$\right)$ pressure with time, **(c)** Amount of gas in the RPC with time assuming $V_{\mathrm{rpc}} = 6.3$ litres for sample RPC gap-1.

variation of the atmospheric pressure shown in the Figure 2.7(b) is called the Solar Atmospheric

Tide. It can be observed that the pressure inside the gap is following the trend of atmospheric

pressure. This implies that the volume of the gap changes with the change of atmospheric

pressure. The change in room temperature also affects the pressure inside the RPC, again

affecting the volume of the RPC gap. This change of the volume during the leak test poses the main difficulty in calculating the leak rate.

Now, from the Ideal Gas Law, the amount of gas (n), inside a chamber of volume V, can be calculated at time t using the following equation,[5]

$$n_{\text{rpc}|t} = \frac{P_{\text{rpc}|t} V_{\text{rpc}|t}}{R T_{\text{rpc}|t}} \tag{2.2}$$

where, R is the ideal gas constant having the value $8.314 \, \text{J mole}^{-1} \, \text{K}^{-1}$. From the dimensions of the gas gap, the volume of the RPC is estimated to approximately 6.3 litres. Taking this into consideration, the amount of gas inside the gap can be calculated using the equation 2.2. The Figure 2.7(c) shows the apparent variation of the amount of gas within the gap with respect to time. The instantaneous leak rate of a gap can be quantified as the slope of this plot at any particular instant.

To estimate the absolute leak rate, Poiseuille's equation for compressible fluids[49] is used. The Poiseuille's equation of Leak Rate at time t for compressible fluids is given in the equation 2.3,

$$\underbrace{\frac{\mathrm{d}n_{\text{rpc}}}{\mathrm{d}t}\bigg|_t}_{\text{flow/leak rate}} = \underbrace{C_{\text{Leak}}}_{\text{flow/leak constant}} \times \underbrace{\left(\frac{P_{\text{rpc}|t}^2 - P_{\text{atm}|t}^2}{2 P_{\text{rpc}|t}} \right)}_{\text{effective pressure difference}} \tag{2.3}$$

where, C_{Leak} depends on the path of leakage (i.e. crack, hole, etc) and the viscosity of the gas mixture and it quantifies the leakage in the system.[6] The Figure 2.8 shows the leak rate $\left(\frac{\mathrm{d}n_{\text{rpc}}}{\mathrm{d}t} \right)$ which is calculated from Figure 2.7(c) as a function of the effective pressure difference $\left(\frac{P_{\text{rpc}}^2 - P_{\text{atm}}^2}{2 P_{\text{rpc}}} \right)$.[7]

According to the equation 2.3, it is expected to behave like a straight line passing through the origin with the slope (C_{Leak}) quantifying the leakage in the system but the observed distribution is not a straight line. Also, the gas gap under test is sealed from the inlet. Hence, no more gas is getting filled but the Figure 2.7(c) shows an apparent increase in the amount of gas inside the gap. This discrepancy is appearing as the change in the volume of the RPC is not

---

[5]All the values of P, V and T are converted suitably to calculate the value of n in mole.

[6]The viscosity of the gas is assumed to be constant over the small changes of room temperature during the test period. In case of large changes in temperature, the changes in the value of viscosity are also needed to be considered.

[7]It is assumed that mole $\simeq 22.4$ litres for better visualisation.
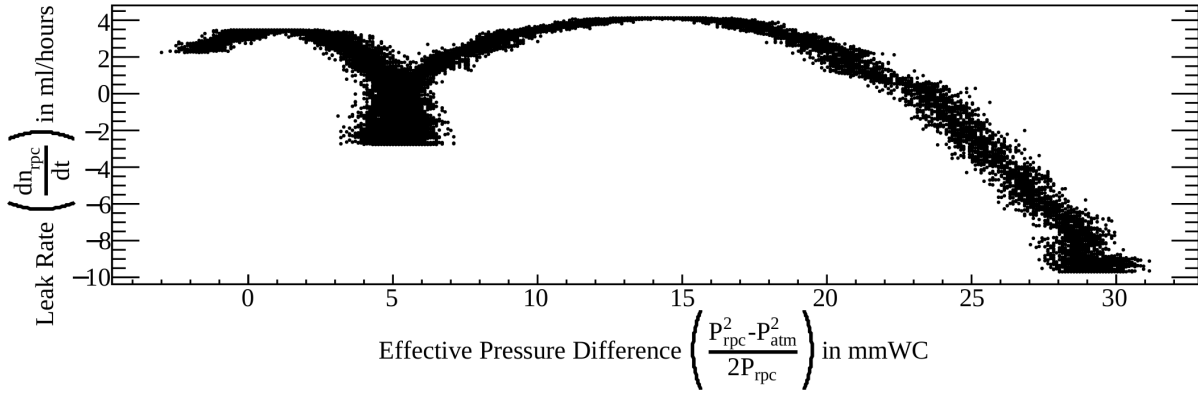
Figure 2.8: $\frac{\mathrm{d}n_{\mathrm{rpc}}}{\mathrm{d}t}$ vs $\frac{P_{\mathrm{rpc}}^2 - P_{\mathrm{atm}}^2}{2P_{\mathrm{rpc}}}$ for the sample RPC gap-1 without any correction.

accounted for in the calculation. Now, as the change in the volume of the RPC gap cannot be measured directly during the test period, a different approach is adopted.

To compensate for this change in volume, the volume of the RPC gap at time t is represented by the equation 2.4,

$$V_{\mathrm{rpc}|t} = \underbrace{V_{\mathrm{rpc}}}_{\text{Approx. Volume}} \times \underbrace{\left(1 - x_T \left(T_{\mathrm{rpc}|t} - T_{\mathrm{rpc}|t=0}\right)\right)}_{\text{Correction for Temperature Change}} \times \underbrace{\left(1 - x_P \left(P_{\mathrm{atm}|t} - P_{\mathrm{atm}|t=0}\right)\right)}_{\text{Correction for Pressure Change}} \qquad (2.4)$$

where, $T_{\mathrm{rpc}|t=0}$ and $P_{\mathrm{atm}|t=0}$ are equal to T_{rpc} and P_{atm} at time $t = 0$, respectively.[8] Assuming that the change in volume is linear in both the atmospheric pressure and the room temperature, two independent linear correction terms (x_P and x_T) are introduced.[9] Using the equation 2.4 in the equation 2.2, the n_{rpc} is represented in the equation 2.5.

$$n_{\mathrm{rpc}|t} = \left(\frac{V_{\mathrm{rpc}}}{R}\right)\left(\frac{P_{\mathrm{rpc}|t}}{T_{\mathrm{rpc}|t}}\right)\left(1 - x_T \left(T_{\mathrm{rpc}|t} - T_{\mathrm{rpc}|t=0}\right)\right)\left(1 - x_P \left(P_{\mathrm{atm}|t} - P_{\mathrm{atm}|t=0}\right)\right) \qquad (2.5)$$

Now, in order to calculate the n_{rpc} for the test period using the equation 2.5, it is required to find the suitable values for the correction factor, x_P and x_T. The value of these correction factors are found (or minimised) against the plot in the Figure 2.8. The method to find the values is described below.

a. For a chosen combination of values of x_T and x_P, n_{rpc} is calculated using equation 2.5 and

---

[8]Suffix 'atm' denotes the measurements acquired from atmosphere.
[9]Present method of estimation of leak cannot handle change in volume caused by 'button pop-up' event during the period of leak test.

then is plotted against time.

b. The plot of $\frac{dn_{rpc}}{dt}$ vs $\frac{P^2_{rpc} - P^2_{atm}}{2P_{rpc}}$ is then prepared using the plot described in the process [a].

c. The same plot is then fitted with a straight line and χ^2/ndf is calculated.

d. The processes [a–c] are repeated for different combination of x_T and x_P, and χ^2/ndf's are obtained for each combination. The χ^2/ndf values for each combination of x_T and x_P are shown in the Figure 2.9. For a particular combination of x_T and x_P, the χ^2/ndf will be minimum which is shown in the Figure 2.9.
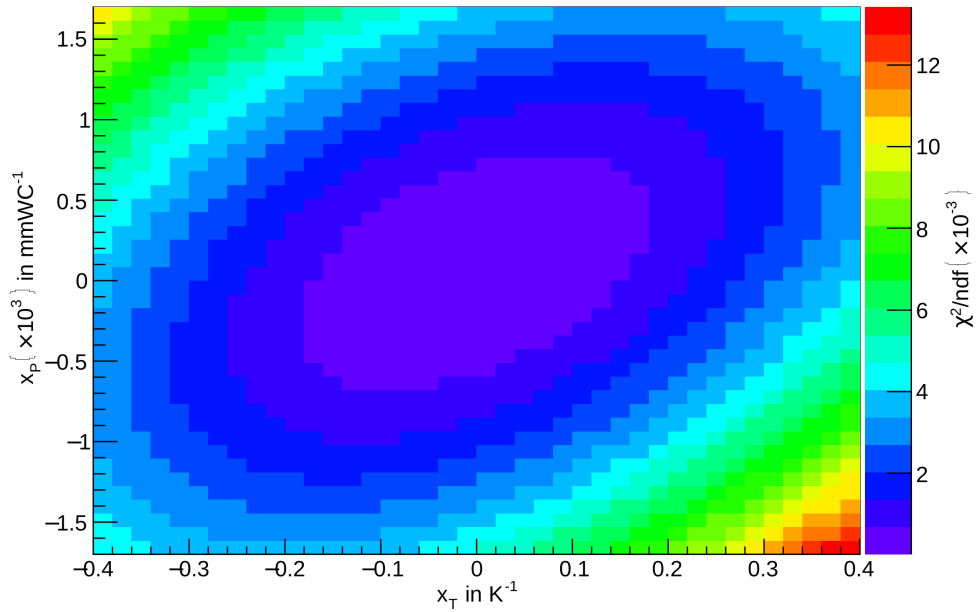
Figure 2.9: χ^2/ndf values of the straight line fit for the plots of $\frac{dn_{rpc}}{dt}$ vs $\frac{P^2_{rpc} - P^2_{atm}}{2P_{rpc}}$ for different combinations of x_T and x_P for sample RPC gap-1.

e. In order to reduce the uncertainties at the minimum χ^2/ndf, the procedures [a–d] are repeated for multiple iterations with subsequently smaller range of x_T and x_P to obtain the final values.

In the current case of sample RPC gap-1, the correction terms at minimum χ^2/ndf are found to be

$$x_T = -3.23 \times 10^{-3} \, \text{K}^{-1} \text{ and } x_P = 7.83 \times 10^{-5} \, \text{mmWC}^{-1}.$$

The negative value of the x_T denotes that the volume of the gas-gap increases with increase in room temperature and the positive value of the x_P denotes that the volume of the gap de-

creases with increase in atmospheric pressure. In both cases, the values do not contradict with the Ideal Gas Law. After including the best-fit values of x_T and x_P in the equation 2.5, the amount of gas inside the RPC gap $\left(n_{\text{rpc}}\right)$ against time is shown in the Figure 2.10. It can be
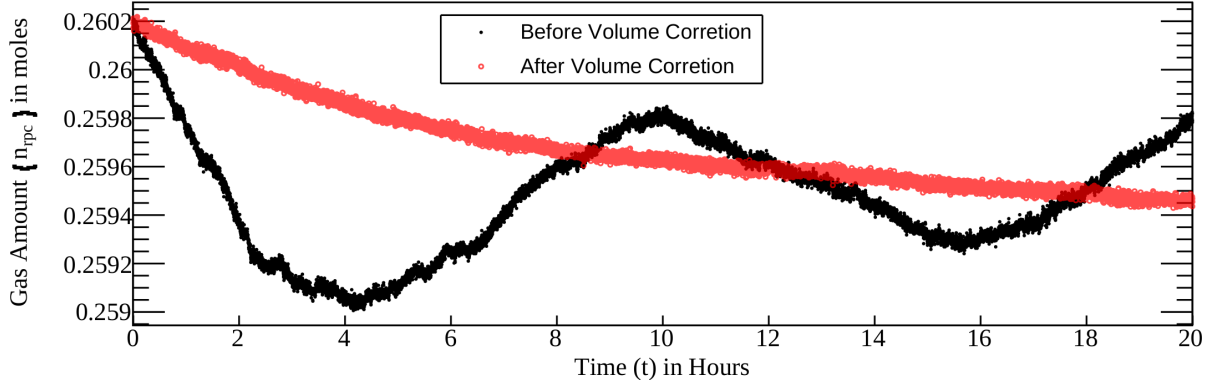
Figure 2.10: Amount of gas in the RPC before (Black) and after (Red) correction for sample RPC gap-1.

noted in the Figure 2.10 that the apparent increase of gas amount seen earlier without the correction is resolved after applying the volume correction. The effect of the volume correction also can be observed in the plot of $\frac{dn_{\text{rpc}}}{dt}$ vs $\frac{P^2_{\text{rpc}}-P^2_{\text{atm}}}{2P_{\text{rpc}}}$ in the Figure 2.11 which follows a nice straight line as expected from Poiseuille's equation.
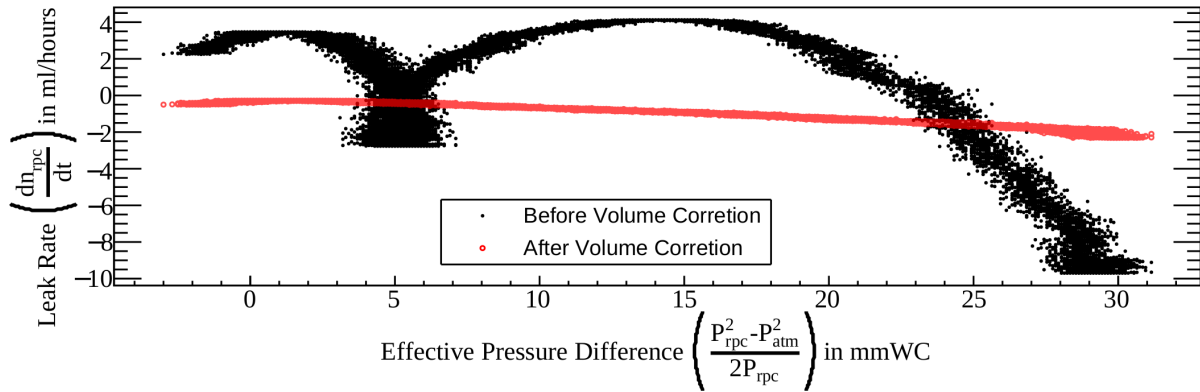
Figure 2.11: $\frac{dn_{\text{rpc}}}{dt}$ vs $\frac{P^2_{\text{rpc}}-P^2_{\text{atm}}}{2P_{\text{rpc}}}$ plots before (Black) and after (Red) correction for sample RPC gap-1.

The value of C_{Leak} calculated from the Figure 2.11 is

$$C_{\text{Leak}} = -\left(6.73 \pm 0.007\,(\text{stat})\right) \times 10^{-2}\,\text{ml}\,\text{hour}^{-1}\,\text{mmWC}^{-1}.$$

The negative value of C_{Leak} implies that the leakage of gas is from inside to outside, which
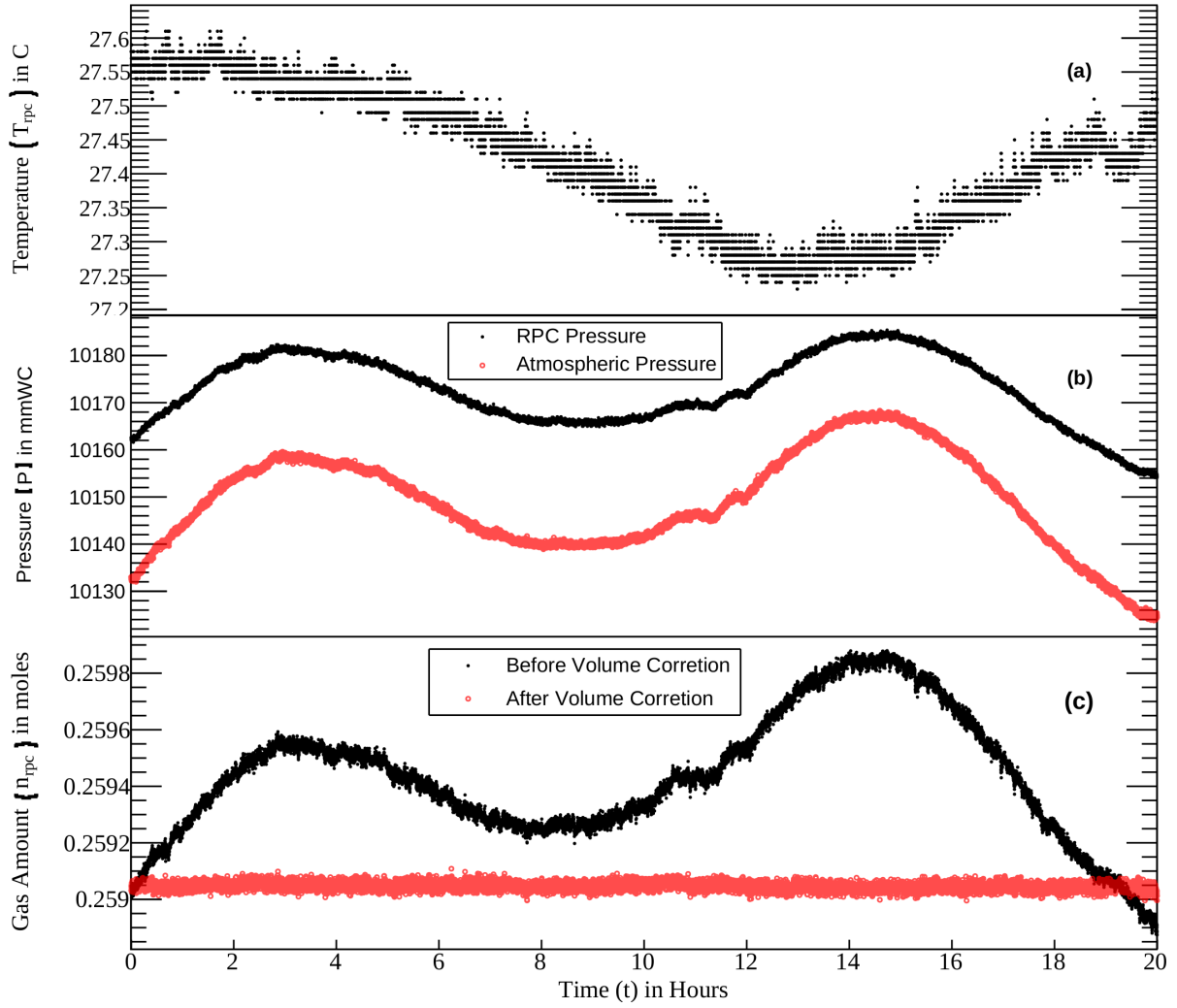
Figure 2.12: **(a)** Variation of temperature (T_{rpc}) with time, **(b)** Variation of atmospheric (P_{atm} : Black) and RPC (P_{rpc} : Red) pressure with time, **(c)** Amount of gas in the RPC before (Black) and after (Red) correction for sample RPC gap-2.

again agrees with the value of the pressure difference. Now, if this RPC gap is kept under a constant pressure difference of 20 mmWC, then it would leak a total of 1.442 $m$mol or 32.3 ml gas in 24 hours. This RPC gap thus can be tagged as leaky.[10]

The Figure 2.12 and 2.13 show the test results for another RPC gap (namely, gap-2). From the Figure 2.13, the value of C_{Leak} for this RPC gap is estimated to be

$$C_{Leak} = -(5.1 \pm 0.15\,(\text{stat})) \times 10^{-4}\,\text{ml}\,\text{hour}^{-1}\,\text{mmWC}^{-1}.$$

In this case, the total leak would be $10.93\,\mu$mol or 0.245 ml of gas within 24 hours if a constant

---

[10]The accepted value of the leak rate is greater than -0.02 ml hour^{-1} mmWC^{-1} and detailed are given in the section 2.2.
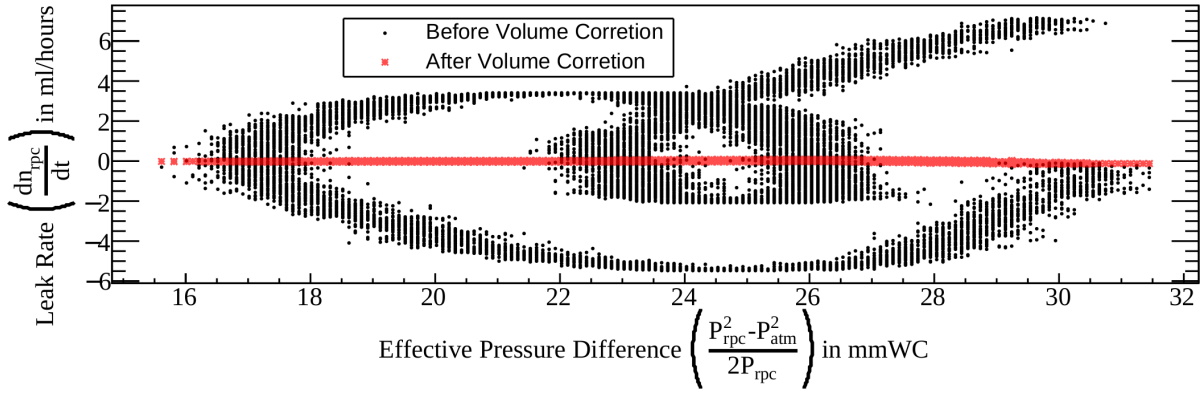
Figure 2.13: $\frac{dn_{rpc}}{dt}$ vs $\frac{P_{rpc}^2 - P_{atm}^2}{2P_{rpc}}$ plots before (Black) and after (Red) correction for sample RPC gap-2.
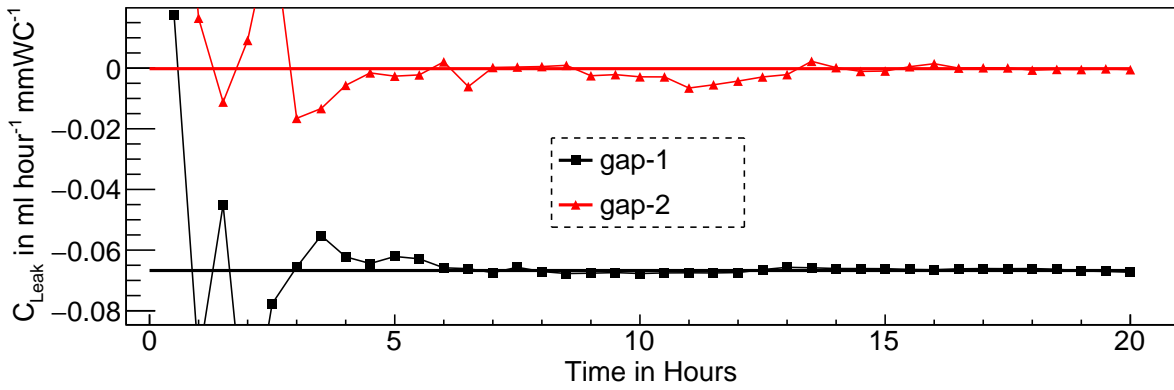
Figure 2.14: Leak rate estimation for data sets of different length for gap-1 and and gap-2.

pressure difference of 20 mmWC is maintained. The leak from this RPC gap is much smaller than the one discussed earlier.

One of the aims of this study is to estimate the optimum (or minimum) time required for calculating the leak rate satisfactorily. As seen in the Figure 2.7, the duration of the test is about 20 hours. Several calculations of the leak rate (C_{Leak}) are performed starting with the same data set, but up-to different lengths. In the Figure 2.14, the value of C_{Leak} for different duration of data is plotted. For RPC gap-1, it can be observed that a minimum of 7-8 hours is required to estimate the leakage without significant uncertainty. This method requires a significant amount of data to fit the $\frac{dn_{rpc}}{dt}$ vs $\frac{P_{rpc}^2 - P_{atm}^2}{2P_{rpc}}$ plots in order to get proper results. Hence, the minimal time required for a test will depend on the quantity of the leakage and also the environmental conditions during the test. If the leak rate is very small then more time is needed. In the case of RPC gap-2, it can be observed from Figure 2.14 that about 7 hours is required to estimate leak rate with an uncertainty of $\sim 2 \times 10^{-3}$ ml hour^{-1} mmWC^{-1}, but about 15 hours is
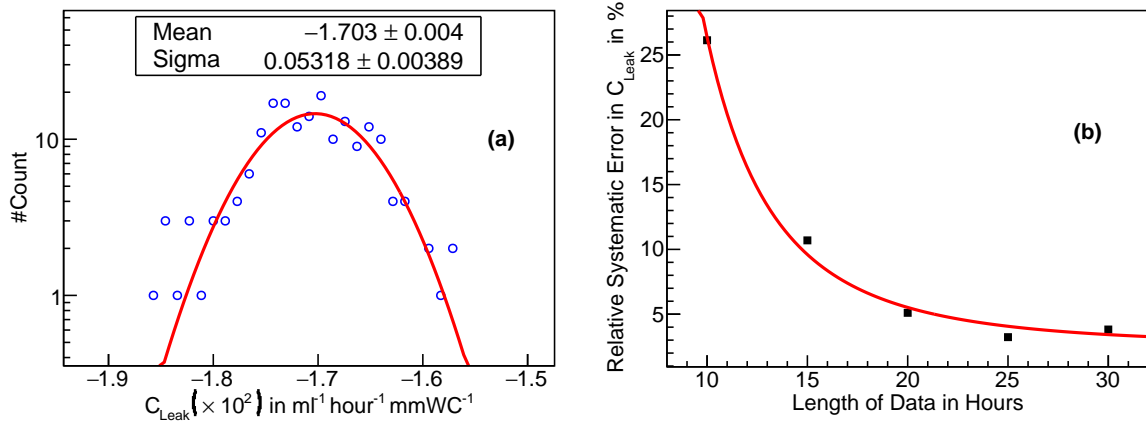
Figure 2.15: **(a)** Systematic error with data sets with length of 25 hours, **(b)** Variation of relative systematic error with length of data.

needed to have a result with uncertainty less than $\sim 2 \times 10^{-4}\,\mathrm{ml\,hour^{-1}\,mmWC^{-1}}$.

It would also be noted that the calculation of C_{Leak} directly depends on the value of V_{rpc}. The relative error in measurement of V_{rpc} will directly propagate to the relative error in calculation of C_{Leak}.

2.1.5   Systematic Error

A well defined method should be able to reproduce the same result in a repeated test under different test conditions. The success of this procedure depends on the periodic changes of ambient pressure and temperature which are largly unpredictable. To estimate the systematic error in the estimation of C_{Leak}, one of the RPC gaps is tested for 48 hours. Several data samples of equal duration have been generated from this large data sample and 'C_{Leak}'s are estimated in each case. The Figure 2.15(a) shows the distribution of the estimated 'C_{Leak}'s for data samples of the duration of 25 hours. The relative width of C_{Leak} for the different duration of time is presented in Figure 2.15(b), which is considered a systematic error of this measurement. For a longer duration it is about 3.1%. As expected, it can be observed that by lengthening the test duration, the relative systematic uncertainty in the measurement of C_{Leak} decreases significantly.

2.1.6   Result of the Tested RPC Gaps

The set-up and the procedures described in this chapter have been used to test eighty RPC gaps.
The results of these tests are summarised in the Figure 2.16 and general findings are listed here.
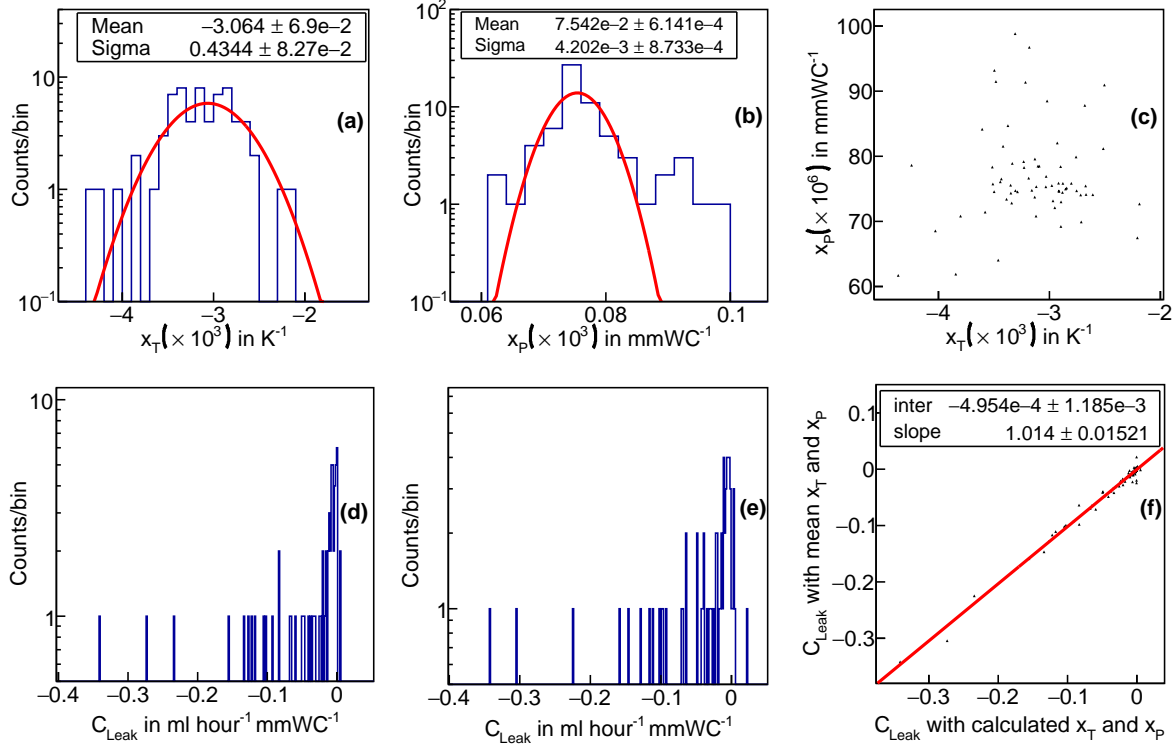
Figure 2.16: **(a)** x_T values of eighty RPC gaps, **(b)** x_P values of eighty RPC gaps, **(c)** Correlation between minimised values of x_T and x_P for eighty RPC gaps, **(d)** C_{Leak} of eighty RPC gaps with calculated values of x_T and x_P, **(e)** C_{Leak} of eighty RPC gaps with mean values of x_T and x_P, **(f)** Correlation between C_{Leak} obtained by both calculated and mean values of x_T and x_P for eighty RPC gaps.

- The correction parameters depend on the structure of each of the RPC gaps. The values of x_T and x_P should ideally be the same for similar type of RPC gaps, but it is almost impossible to manufacture inch-perfect replicas. Any gap with popped up button spacers(s) ('button pop-up' is discussed in Section 2.1.3) will also reflect higher values of these two parameters. This causes the spread in the values of x_T and x_P which can be seen in the Figure 2.16(a) and 2.16(b), respectively.

- The minimised values of x_T and x_P for a gas gap are two independent parameters. As expected, it can be seen in the Figure 2.16(c) that there is no correlation between these two parameters for eighty RPC gaps which were tested.

- The Figure 2.16(d) shows the values of C_{Leak} for eighty RPC gaps where the values of x_T and x_P are calculated explicitly for each RPC gap. The Figure 2.16(e) shows the same but with the mean values of x_T and x_P obtained from 2.16(a) and 2.16(b), respectively.

- Figure 2.16(f) shows correlation between C_{Leak} obtained by calculated x_T and x_P values explicitly for each chamber (shown in the Figure 2.16(d)) and by mean x_T and x_P values (shown in the Figure 2.16(e)). The nature of correlation is direct. So, mean values of x_T and x_P can also be used for a quick calculation saving CPU time.

2.2   Chapter Summary

The method outlined above can give a quantitative estimation of the leak of an RPC with higher precision and in much less time compared to what may be obtained using a conventional manometer. This method can be used for any kind of sealed chambers other than RPC where the structure of the chamber is prone to deform due to variation in ambient pressure and temperature. As discussed in the reference [53], it is possible to eliminate the effect caused by ambient temperature by the use of an enclosure where the temperature is controlled precisely in case of abrupt and/or irregular changes in ambient temperature, causing difficulties in the calculation of volume correction factors. It should be noted that the minimum time required for a test will depend on extent of the leakage. If the leak rate is very small then more time is needed, but most of the gaps were possible to be tested within 7-8 hours with an accuracy of $\sim 2 \times 10^{-3}$ ml hour^{-1} mmWC^{-1}. Currently, a gas gap is considered as usable if its C_{Leak} value is greater than -0.02 ml hour^{-1} mmWC^{-1}. If the RPCs are operated at an excess pressure of 10 mmWC above atmospheric pressure, the total leakage from ICAL detector will be approximately 6 litres/hour during its active operation.

The leak-test setups, both wired and wireless, are built and tested. The setups are now being used at various facilities and industries working along with INO-Collaboration. With the help of the prepared document, even a novice can test a large number of RPCs in a short time. The difficulty in handling a glass RPC increases significantly with its size. As the present method does not require the RPC to be moved during the tests. Also, the knowledge gained in this

study gives us more opportunity to better understand the structural integrity of the glass RPCs
against various atmospheric parameters.

The work presented in this chapter is published in [54].

Chapter 3

Study of Particle Multiplicity of Cosmic Ray Events using $2\,\mathrm{m} \times 2\,\mathrm{m}$ Resistive Plate Chamber Stack at IICHEP-Madurai

One of the main notions of the INO Project is to collaborate with Indian Industries in order to streamline the production and the procurement of various components as well as the RPC detectors. Transfer of technologies and experiences in between industries and research teams is the key aspect of this effort. An experimental setup consisting of 12 layers of glass Resistive Plate Chambers (RPCs) of size $2\,\mathrm{m} \times 2\,\mathrm{m}$ has been built at IICHEP-Madurai ($9°56'14.5''$ N $78°0'47.9''$ E, on the surface) to study the long term performance and stability of RPCs produced on large scale in Indian industry. This setup has been collecting data triggered by the passage of charged particles. The data is analysed to understand the behaviour of the RPCs as well as the electronics used to run and collect data from the setup. The data is also utilised to gain knowledge of the cosmic ray muons reaching the surface of the Earth. The measurement of the multiplicity of charged particles due to cosmic ray interactions are presented here. The results are compared with different hadronic models of the CORSIKA simulation. The data collected near the magnetic equator gives us vital information regarding the capabilities of the simulation packages. As the current experimental setup is located within 81 km from INO-Site and nearly at the same latitude, in depth analysis of this data also improves the prediction power

of the Monte-Carlo simulations of neutrino events for this project.

3.1   Cosmic showers at the Earth surface

The upper atmosphere of the Earth gets a large dose of exposure of high energy primary cosmic rays originating in outer space. These primary cosmic rays consist of mostly protons with a smaller fraction of higher Z-Nuclei elements[27]. The angular distributions of the primary cosmic rays are more or less isotropic at the top of the atmosphere. The energy spectrum of the primary cosmic rays follow the power-law, $dN/dE \propto E^{-\gamma}$, where $\gamma \sim 2.7$. The shower of secondary particles consisting mainly of pions $\left(\pi^{\pm}/\pi^{0}\right)$ and kaons $(K^{\pm})$ which are produced due the interactions of primary cosmic rays with atmospheric nuclei. The neutral pions mainly decay via electro-magnetic interactions, $\pi^{0} \rightarrow \gamma + \gamma$ whereas the charged pions decay to muons and neutrinos via weak-interactions, $\pi^{+} \rightarrow \mu^{+} + \nu_{\mu}$ and $\pi^{-} \rightarrow \mu^{-} + \bar{\nu}_{\mu}$. The kaons also decay to muons, neutrinos and to pions following different branching fractions. Most of the pions and kaons decay in flight and do not reach the Earth's surface. A small fraction of resultant muons decay into electrons and neutrinos, $\mu^{+} \rightarrow e^{+} + \nu_{e} + \bar{\nu}_{\mu}$ and $\mu^{-} \rightarrow e^{-} + \bar{\nu}_{e} + \nu_{\mu}$. The γ, $e^{\pm}$ do not reach the detector directly as they interact with the roof of the laboratory and generate electromagnetic showers. Thus, muons are the most abundant charged particle from cosmic ray showers detected in the present setup. These atmospheric muons are produced at high altitude (average height of $20\,\mathrm{km}$) in the atmosphere and lose almost $2\,\mathrm{GeV}$ energy via ionisation loss in the air before reaching the ground. The density of charged particles (mainly muons) per unit surface area at the Earth's surface depends on the composition of primary cosmic ray, power-law parameter (γ) as well as the model of hadronic interactions at high energy which is not accessible in the laboratory.

The principal aim of this work is to observe the charged-particle multiplicity in the atmospheric muon data collected at IICHEP, Madurai and compare it with the air shower simulation.

In this study, the detector setup has been described in the Section 3.2. The Monte-Carlo simulation techniques used to study the multiplicity has been explained in Section 3.3, where primary cosmic ray interactions are simulated using the CORSIKA Package[55] and interac-

tions of the particle with detector material are simulated using the GEANT4 toolkit[56].

3.2   Detector Setup

The RPC stack used in this study was in operational at IICHEP, Madurai consisting of 12 RPCs

stacked horizontally with an inter-layer gap of 16 cm is shown in Figure 3.1 where the *X*-axis of

the detector is making an angle of $-10°$ with the geographic south. An RPC gap is made of two
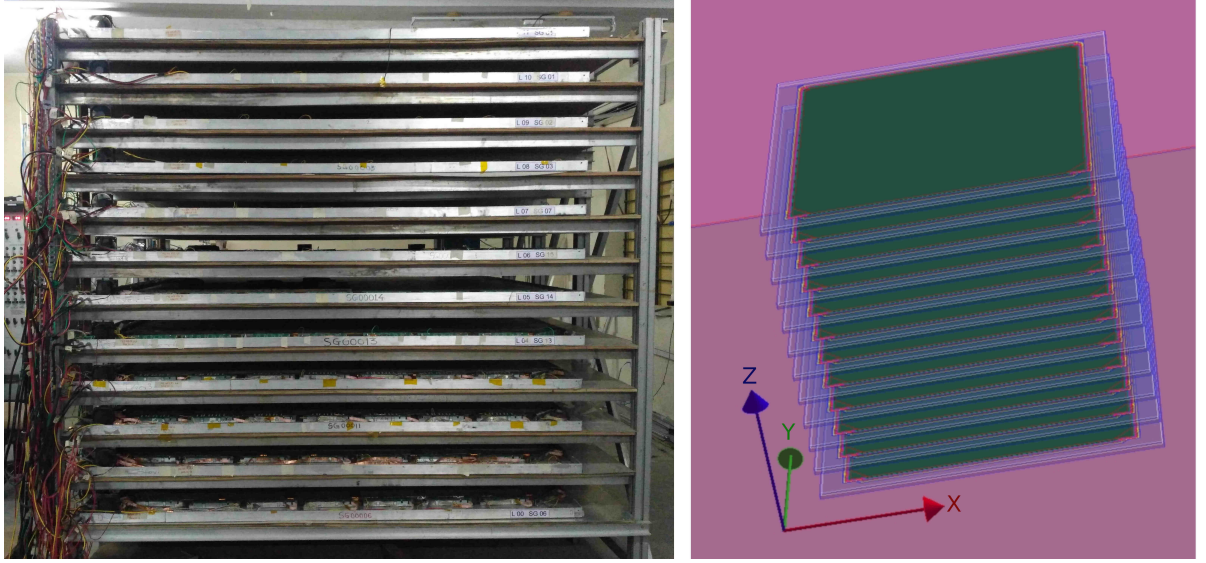
Figure 3.1: The detector stack with 12 layers of RPCs where the *X*-axis of the detector is
making an angle of $-10°$ with the geographic south, (left) experimental setup and (right) Geant4
detector geometry of stack.

glass electrodes of thickness 3 mm with a gap of 2 mm between them. Uniform gap between

these two electrodes is maintained using an array of 2 mm thick poly-carbonate buttons. The

glass gap is sealed on the outer edges to make it air-tight. A non-flammable mixture of gas

is continuously flown inside the glass gaps via strategically placed nozzles. This mixture of

gasses serves as the active medium of the detector. The RPCs are operated in avalanche mode.

In this case, the mixture of gases consists of R134a (95.2%), iso-C_4H_{10} (4.5%) and SF_6 (0.3%).

Both the outer surfaces of the glass gap are coated with a thin layer of graphite. The RPCs

are operated by applying a differential supply of $\sim \pm 5$ kV to the graphite layers to achieve the

desired electric field. A small variation in applied HV is due to the variation of gain in different

RPC. The target gas inside the RPCs gets ionised by the transit of charged particles. This

ionisation eventually evolves into an avalanche in the presence of the high electric field between

the glass electrodes. The avalanche in the RPCs induces signals in the two orthogonal pickup panels placed on both sides of the glass gaps labelled as X-side (bottom) and Y-side (top). The pickup panels are made of parallel copper strips of width 28 mm with 2 mm gap between two consecutive strips. The RPCs used in this detector stack are of the size of 1790 mm × 1890 mm. There are 60 strips on the X side and 63 strips on the Y side for each layer.

The induced signals from the pickup strips are amplified and discriminated by a charge sensitive NINO[57] amplifier-discriminator board. Only in layer 11 (topmost layer), ANUS-PARSH ASIC[58] which is a CMOS, 8-channel, high speed, low power amplifier-discriminator designed for avalanche mode of operation for RPCs is used to study its performance. The discriminated signals from these boards are passed to the FPGA-based RPCDAQ-board. The individual signals from every 8th strips are *OR*ed to get pre-trigger signals (S0 to S7), which are passed to the Trigger system module via Signal Router Board. The four-fold coincidence is done for X- and Y- sides independently in the Trigger Logic Boards. The Global Trigger is then generated by the Global Trigger Logic Board (GTLB) by *OR*ing the coincidences formed in X- and Y-side. The trigger scheme of the detector setup contributed by 4 RPC layers is illustrated in the Figure 3.2.
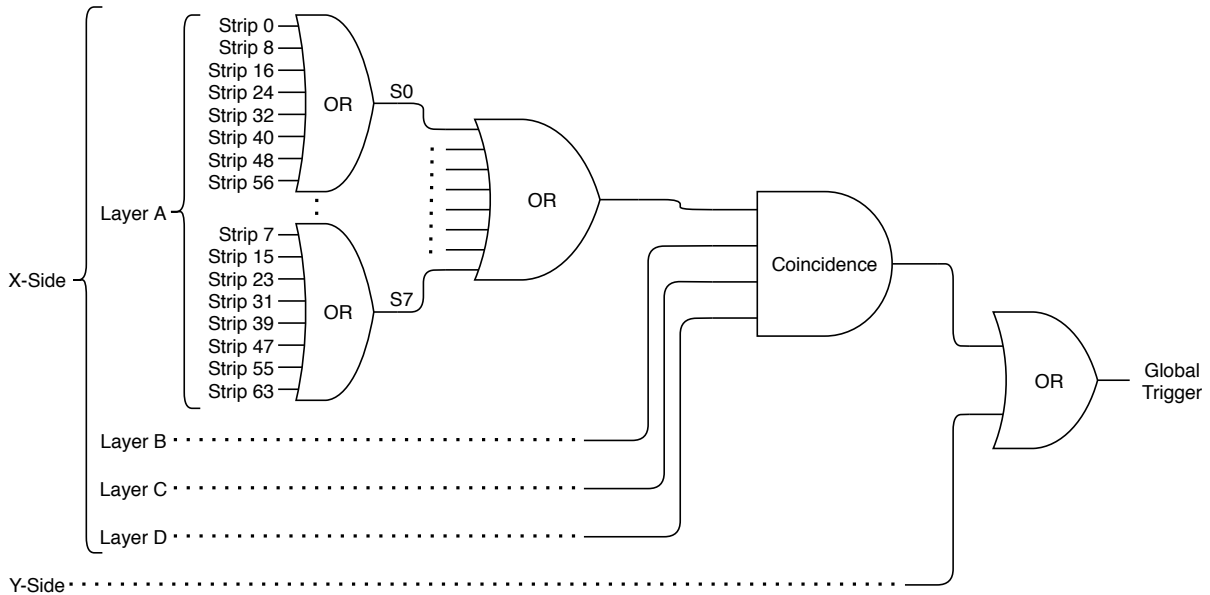
Figure 3.2: Trigger Scheme of the Detector Setup.

The hit signals in the RPCDAQ board stretched to 1 μs to overcome trigger latency of 770 ns from Trigger System to RPCDAQ. Based on the arrival of trigger signals to RPCDAQ, the event

signals are latched and sent to the Data Concentrator and Event Builder via Network Switch. The trigger system's 'dead-time' is set at 500 ns after generation of a trigger to process and store the triggered event. The flow of signals in the detector setup is shown in the Figure 3.3. The
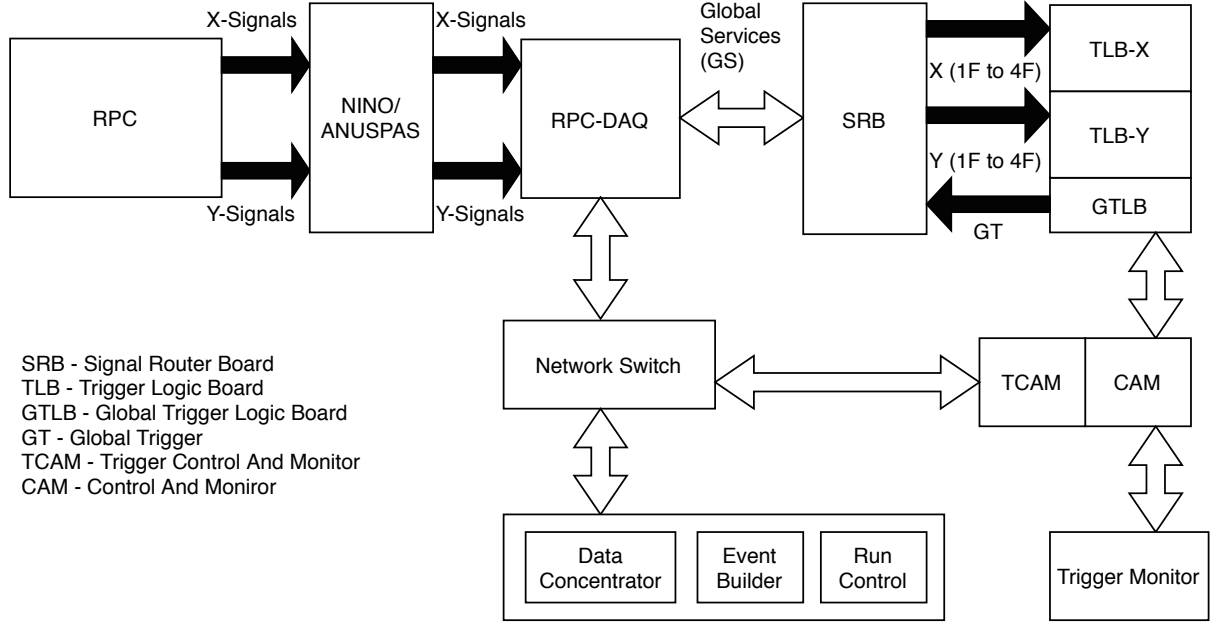
Figure 3.3: The Flow of Signals in the Detector Setup.

detailed description of signal processing and the Data Acquisition system (DAQ) can be found in [59]. The present work is based on the coincidence of pre-Triggered signals from layers 4, 5, 6 and 7 within a coincidence window of 100 ns. While the layers in the middle portion of the detector are used to form the trigger, the layers in both the top and bottom portions of the detector also contributes in forming an event, which in turn maximises the length of the track in the detector.

The stretched signals get latched for recording when the trigger reaches the RPCDAQs. Ideally, the signals occurring only within the coincidence window should get latched. But for this setup, the signals for any other particles as well as noise occurred outside the coincidence window may also get recorded due to stretching of the hit signals and trigger latency. A generalised timing diagram of an event which includes the hits from two particles is shown in the Figure 3.4 to illustrate this. If a particle, generating the trigger, has passed through the detector at time t_1, then all other signals within the period of t_1 to $t_1 + 770$ ns also get recorded due to the trigger latency of 770 ns. On the other hand, the signals generated within the time period $t_1 - 230$ ns to t_1 also get recorded as well but only in the following situations.
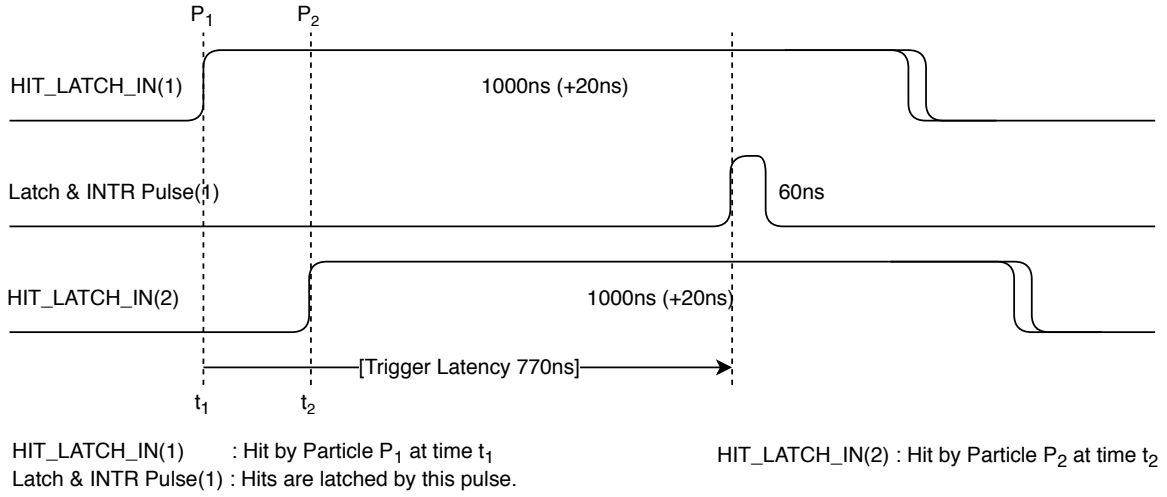
Figure 3.4: Timing diagram of an event.

- **Case 1:** The hits generated by the other particle did not satisfy the trigger criteria.

- **Case 2:** The hits generated by the other particle satisfied the trigger criteria, but failed to generate a trigger as it occurred within the 'dead-time' of the trigger system.

- **Case 3:** The hits generated by any of the particles in the event did not satisfy the trigger criteria individually. But hits generated by both particles altogether satisfy the trigger criteria.

An event typically contains hit information (one logic bit per strip indicating the signal in that strip) for each strip and 16 time signals for each layer; 8 for X-side and other 8 for Y-side. One TDC (Time-to-Digital Converter) channel with least-count of 0.1 ns records time signals coming from every alternating 8th strips (S0 to S7). Approximately 250 millions of cosmic ray events recorded in the detector during the total observation period between August 23, 2017 to September 8, 2017 with a trigger rate of ~230 Hz are used for the analysis.

3.3 Monte-Carlo Simulation

The Monte-Carlo Simulation for this study has been executed in two stages. The Extensive Air Shower (EAS) has been simulated by the CORSIKA simulation package[55]. The information of daughter particles generated by the EAS at the Earth's surface level has been extracted and used as the input data to the detector simulation. The detector simulation has been executed with the help of the GEANT4 toolkit[56].

3.3.1 Extensive Air Shower

The CORSIKA (COsmic Ray SImulations for KAscade) is developed to study the evolution of the EAS in the atmosphere created by primary cosmic ray. Though the CORSIKA has been developed initially for a specific experiment, this package is now developed into a tool that is used by many groups studying cosmic rays and EAS. In the current study, existing extrapolations of hadronic interaction models of high energy particles in the EAS are based on various theoretical models, which have large uncertainties. The current experimental data at the collider experiments is insufficient to verify the extrapolation of the hadronic interactions at very high energies. In the CORSIKA package, several different hadronic interaction models are available. In this study, for simulating the behaviour of hadrons for higher energy range, the QGSJET (Quark Gluon String model with JETs)[55] has been adopted and for the low energy range (less than 80 GeV in laboratory frame), the GHEISHA model has been used.

In this study, the primary cosmic ray shower has been simulated using the CORSIKA(v7.6300) Package. The energy of the primary rays in the CORSIKA is generated using the power-law spectrum, $E^{-2.7}$, within the energy range of 10–10^6 GeV for different primaries (H, He, C, O, Si and Fe). The zenith and azimuth angle of the primary cosmic particles are generated uniformly within the range of 0–85° and 0–360°, respectively. The rigidity cutoff due to the Earth's magnetic field has been implemented as per the location of the detector. The minimum energy cutoffs for secondary hadrons, muons, electrons and photons in the simulation are kept at 50 MeV, 10 MeV, 1 MeV and 1 MeV, respectively. These cutoff values are much smaller than the minimum momentum cutoff for the charged particles in the vertical direction, ∼ 110 MeV, which is mainly due to 22 cm of concrete roof of the building where the detector is housed. The momentum spectra of secondary charged particles generated by the CORSIKA simulation is shown in the Figure 3.5.

The secondary particles generated by the CORSIKA which are reaching the observation surface are provided as an input to the detector simulation. The observation plane has been divided into squares of the size of 2 m × 2 m which is shown in the Figure 3.6. An event is formed using the information of the particle(s) reaching to each of these squares shown as shaded region in the Figure 3.6.
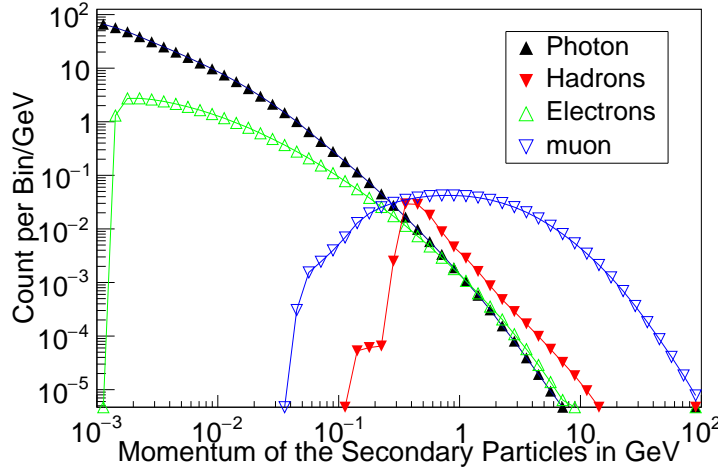
Figure 3.5: CORSIKA generated momentum of secondary particles at observation level.

3.3.2 Detector Simulation

The detector simulation has been accomplished using the GEANT4(v4-10.0.2) toolkit. The events generated in the CORSIKA simulation are propagated event-by-event in the detector simulation. A realistic depiction of the detector setup including the building where the detector is housed has been constructed in the GEANT4 environment. The materials of the various detector components and the laboratory buildings are chosen based on the knowledge of the setup. The uncertainty of the material budget is taken as a systematic error. The physics processes of matter-particle interactions like electromagnetic, ionisation, decay and hadronic interactions (QGSP_BERT_HP), which are available within the GEANT4 toolkit[56] are considered in the simulation.

The various detector parameters (efficiency, noise, strip multiplicity and resolution) are calculated using the cosmic rays passing through the detector stack. The current setup is a tracker type detector consisting of 12 layers of RPCs. When one layer of the setup is studied for the detector parameters, the rest of the layers in the setup serve as the tracker for the passing particles. Since the layers forming the coincidence cannot be studied for the detector parameters, the data sets with two more different trigger combinations (using layers 1,2,3,4 and 7,8,9,10 to form coincidences) of the duration of one day, are used in order to study all the RPCs in the setup.

The efficiency of a RPC gap is defined as the probability of getting a signal from a RPC
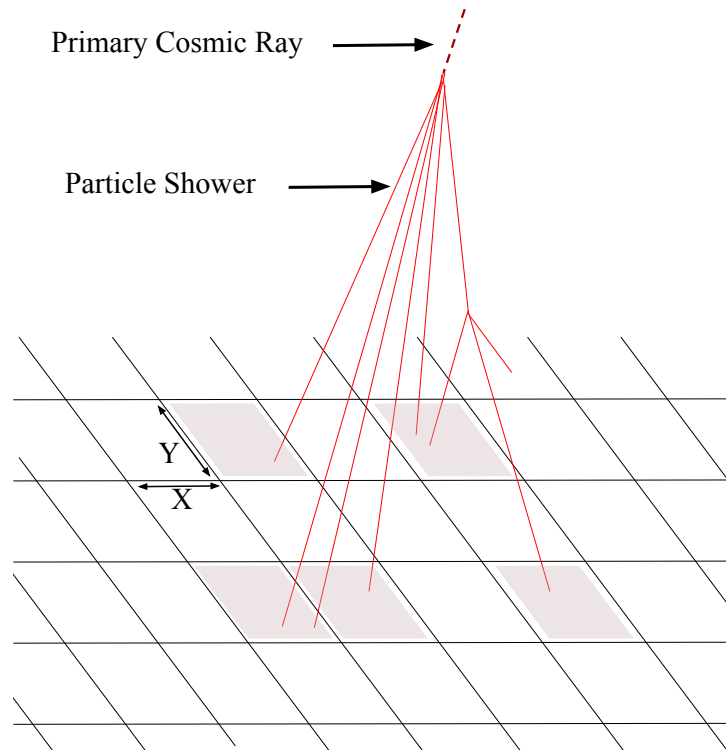
Figure 3.6: Shower of particles initiated by primary cosmic ray reaching observation surface.

when a particle has passed through it. Each of the RPC detectors can be divided into a matrix of
pixels of size 3 cm× 3 cm. The efficiencies of each of the pixels are calculated and represented
as the efficiency map for each of the RPCs. The track(s) of the particle(s) in an event is fitted
with the straight line by excluding the RPC layer being studied from the fit. For each pixel in
that RPC layer, the total number of particles passed through it is estimated from the extrapolated
position in that layer. The ratio of the number of events with valid hit signal in X- (or Y-) strips
of that pixel to the total number of particles passed through it is taken as the efficiency for
the X- (or Y-) side of that pixel. The noise in a RPC is defined as the hits occurred farther
from the expected position of the passing particle. The strip multiplicity profile is defined as
the probability of sharing signal between neighbouring strips with respect to the hit position
from the centre of the strip. The strip multiplicity is discussed in the next section. A detailed
study of these parameters are presented in [45]. The efficiency map, noise and strip multiplicity
profile for one of the RPCs in the stack is shown in the Figure 3.7. These observed detector
parameters are included in the digitisation stage of the detector simulation. Both the events from
the observed cosmic ray data and the detector simulation are reconstructed using an algorithm
based on Hough Transformation which is discussed in the next section.

Figure 3.7: (a) Efficiency, (b) Noise and (c) Multiplicity profile of Y side of Layer-2 RPC gap.

3.4 Event Reconstruction and Data Selection

For the event reconstruction, the strip hits are analysed separately, in the 2-dimensional projections namely, X–Z and Y–Z sides. During the passage of a charged particle through a RPC gap, the number of strips on which signal is induced depends on the gain of the gas gap. This sharing of the induced signal between the neighbouring strips i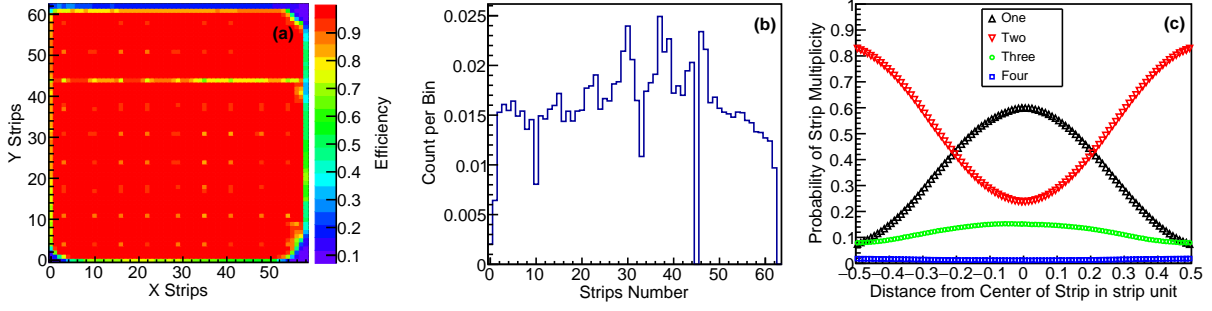s the main reason for the observed strip multiplicity shown in the Figure 3.7(c). In order to prepare the events for this study, the consecutive strips which have recorded signals are clubbed together to form a cluster. During the study, the position resolution is calculated for different strip multiplicities of 1, 2, 3, and 4 and the values observed are ~6 mm, ~8 mm, ~12 mm and ~22 mm respectively. The position resolution for strip multiplicities more than four is larger than the pitch of the strip (3 cm). So in this study, the clusters of hits with more than 4 multiplicities are neglected as the position resolution for higher multiplicities is found to be the worst. A layer which has more than 15 strip hits and/or more than 10 clusters is tagged as 'noisy layer' and not considered in the track reconstruction. The first criterion has been chosen near the maximum number of possible hits if 4 tracks pass through a RPC. In fact, the maximum number of tracks reconstructed in an event is 4 which is discussed in the Result section. The second criterion is set at the first criterion divided by the average strip multiplicity (~ 1.5) in the detector stack to reject noisy events passed through the first criterion. An event which has more than 3 noisy layers is considered as 'noisy event' and discarded. This criterion is set at 3 layers which is 25% of maximum layers available for the event reconstruction. This criterion has been set by considering both the performance of the reconstruction method and number of events lost due to this criterion.

In the first step of track reconstruction, the clusters associated with different tracks are found

and grouped using the method of Hough Transformation[60, 61]. The equation of the straight line, used to find the association between the hits, is given as,

$$r = z \cos \theta + x \, (/y) \sin \theta. \tag{3.1}$$

The r-θ plane (also called as Hough Space) is populated using the concept of Cellular Automaton [62]. For a sample event shown in the Figure 3.8(a), the populated r-θ plane is presented in the Figure 3.8(b). The advantage of using Cellular Automaton technique is the significant
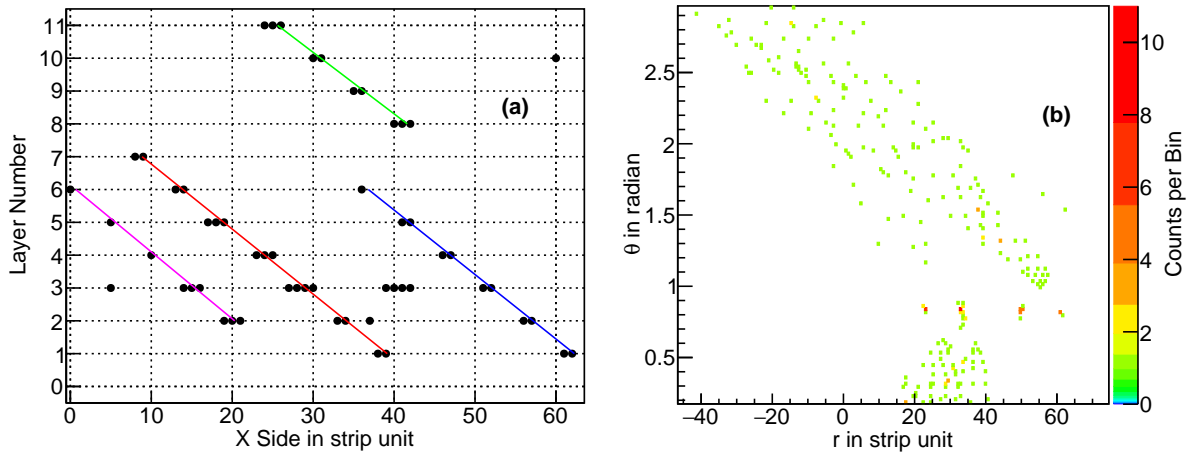
Figure 3.8: (a) Projection of an event in the detector and (b) populated r-θ plane using this event.

reduction of computation time to find a trajectory in the event. This method can detect all the tracks avoiding the noise hits as shown in Figure 3.8(a).

The tracks identified using the Hough Transformation are then fitted by a straight line given by the equation,

$$x \, (/y) = mz + c \tag{3.2}$$

where m and c are the slope and the intersect, respectively. The number of detector layers in the fit and χ^2/ndf of the fit are shown in the Figure 3.9(a) and 3.9(b) respectively. A track is considered as properly reconstructed if the χ^2/ndf is less than 10 and there are more than 4 layers in the track. The reconstruction efficiency is defined as the ratio of the number of events with at-least one reconstructed track to the total number of triggered events. The reconstruction efficiency as a function of time is shown in the Figure 3.10. It can be observed that the
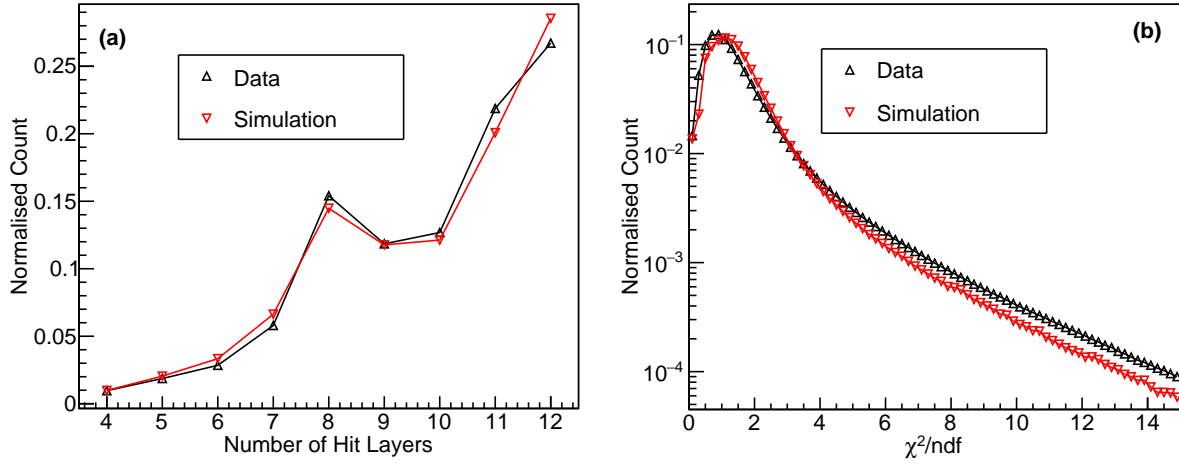
Figure 3.9: (a) Number of hit layer and (b) χ^2/ndf of straight line fit.
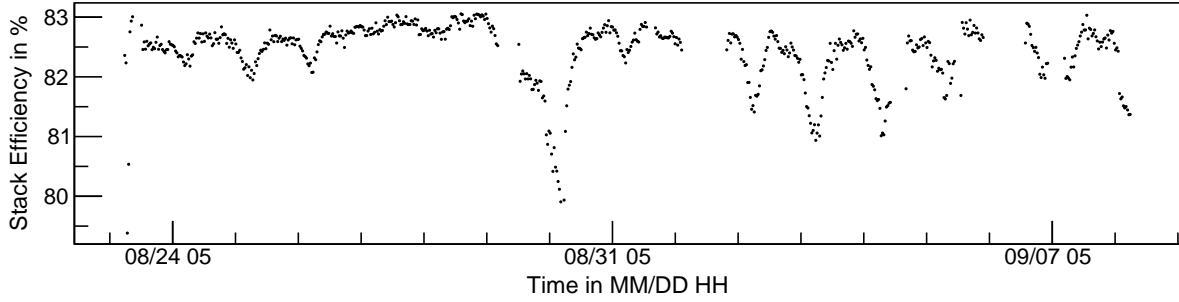
Figure 3.10: Variation of reconstruction efficiency of the detector with time.

reconstruction efficiency varies periodically with time which is correlated to the variation of the ambient pressure and temperature due to the solar atmospheric tides [54]. But this periodic change in the reconstruction efficiency does not affect the relative ratio of the multiple track events. The pure multiple track events are ~0.01% of triggered events. Out of the total triggered events, also 6–7 % of events are due to noises and hadronic showers initiated at the roof. An extreme shower event (which can also be due to the noise) shown in the Figure 3.11 can also imitate a multi-track event. Any such ambiguous events are rejected by the selection criteria used in the study discussed in the following.

The zenith and azimuth angle distributions of the reconstructed tracks are presented in the Figure 3.12(a) and 3.12(b), respectively. The projections from both the X–Z and Y–Z planes are combined to produce the final 3-dimensional track(s). Any ghost tracks formed while combining are discarded by using the timing information recorded for each strip. The events of interest for this study are the events with more than one reconstructed 3-dimensional
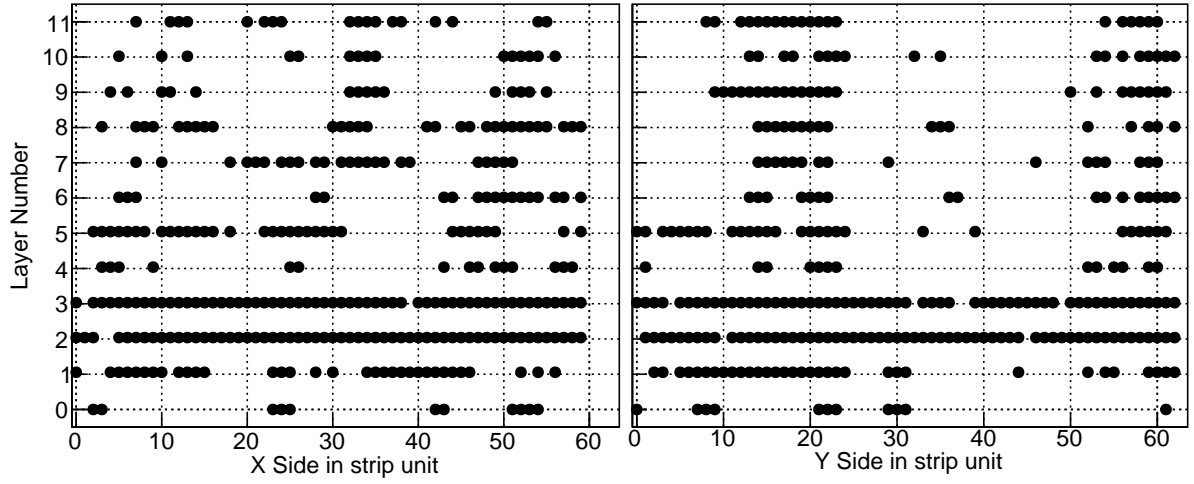
Figure 3.11: Example of an extreme shower event.
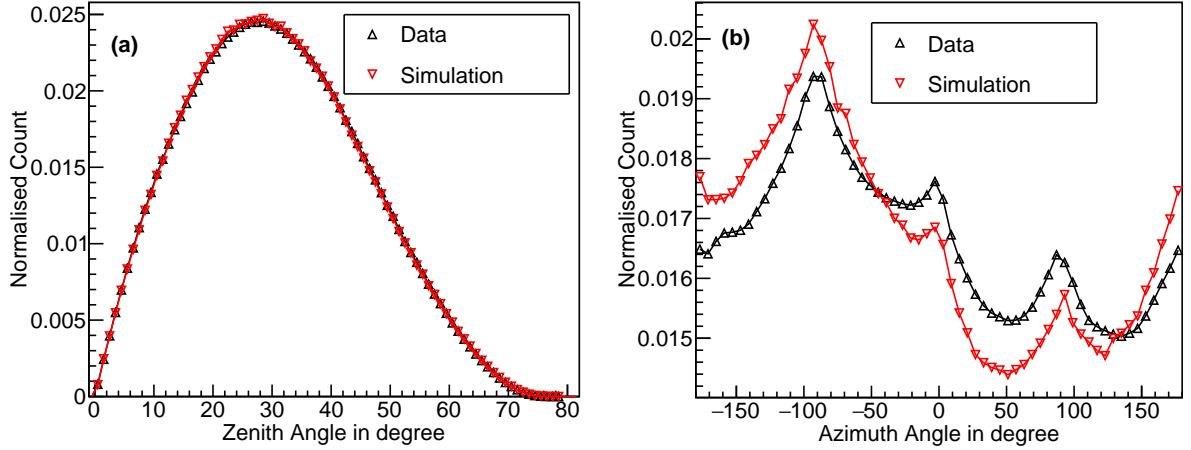
Figure 3.12: (a) Zenith and (b) Azimuth Angle of cosmic rays reaching the detector stack.

track. The distribution of the time separation between each pair of reconstructed tracks for both the simulation and data are shown in the Figure 3.13(a). In the case of data, it can be observed that there is a significant number of events where multiple particles are reaching the detector with large relative time delay. The random coincidence of particles originating in the different cosmic showers is the cause for these events. The random coincidence of particles from different cosmic showers are absent in the simulation as only one shower is simulated at a time in the CORSIKA. So the following procedure is adopted to reject the random coincidences from the events which have been initiated by the same showers.

In the simulation, it is observed that the particles originating from the same shower are detected in the RPC stack as the parallel tracks. This can be verified by calculating the skewed
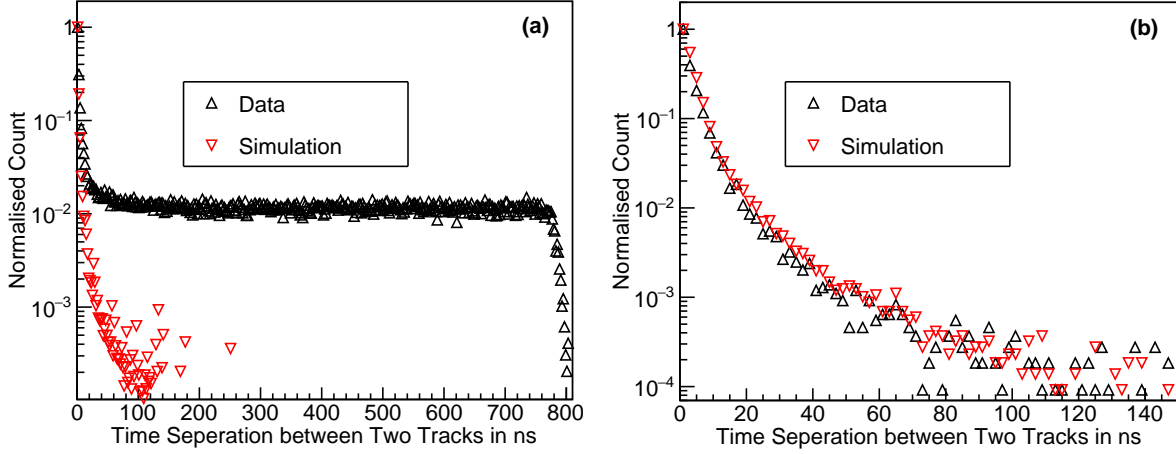
Figure 3.13: Time separation of two tracks for (a) all events and (b) for events with only parallel tracks.

angle between each pair of tracks reconstructed in an event. The value of skewed angle is ide-ally supposed to be zero in case of the parallel tracks, but due to the finite size of the strip width and multiple scattering the distribution of skewed angle has finite width and tail. The distribu-tion of the skewed angle between the each pair of tracks reconstructed from both the simulation and data is shown in the Figure 3.14(a). Now, only the parallel tracks are of the importance in
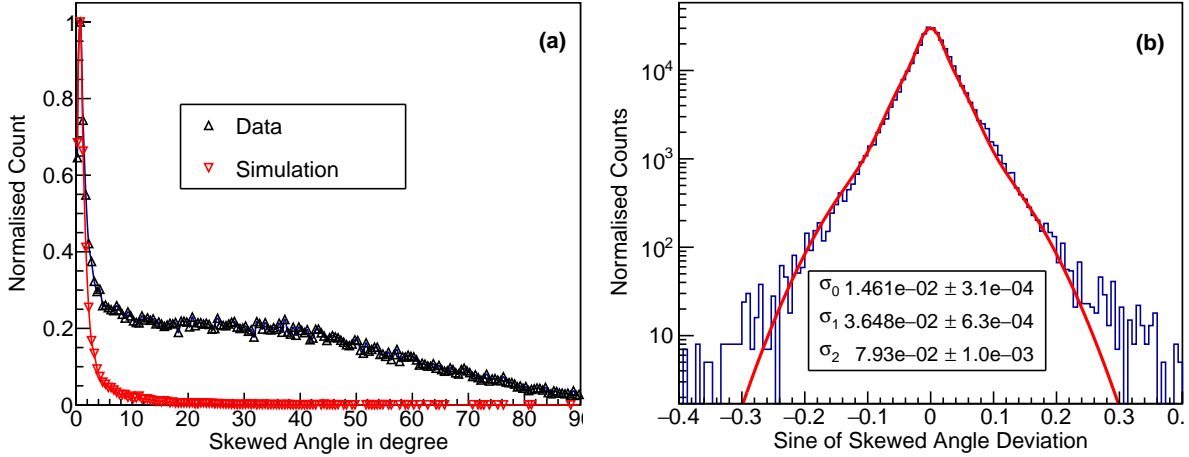
Figure 3.14: (a) Skewed angle between two tracks originating outside of the detector, (b) Skewed angle difference between generated and reconstructed tracks fitted with triple-Gaussian function.

this study because of their same origin. In order to define the parallel tracks reconstructed in this detector setup, good understanding about the resolution of the skewed angle is necessary. To understand the application of the skewed angle, events with multiple particles are simulated in the GEANT4. The skewed angle $\left(s_{gen}\right)$ between the generated pair of tracks in an event is

calculated using their generated directions. The skewed angle (s_{reco}) between the same pair
of tracks is estimated from the track reconstruction also. The distribution of the sine of the
difference of the skewed angle between the generated particles and the skewed angle between
the reconstructed tracks, defined as the $\sin\left(s_{gen} - s_{reco}\right)$, is shown in the Figure 3.14(b). This
distribution is fitted with the triple-Gaussian function. The three components of these angular
resolutions (σ_0, σ_1, σ_2) represent the cases, where (0) no multiple scattering happened for the
pair of tracks, (1) one of the tracks has gone through multiple scattering and (2) both the tracks
have gone through multiple scatterings in the detector medium or in the roof of the building
where the detector is housed, respectively.

Based on these observations, a pair of tracks with a skewed angle less than 2.5° ($\approx 3\sigma_0$)
are considered as parallel to each other. All the pairs of tracks present in a reconstructed event
have to comply with this selection criteria. Thus, in the current study, only the parallel tracks
are considered to select the events generated due to the particles originating from the same
cosmic ray shower. The time difference between a pair of tracks for both the simulated and
observed data after the criteria of parallel track selection is shown in the Figure 3.13(b). It can
be observed that the events from the random coincidences disappear after rejecting the events
with non-parallel tracks.

The particles, originated in the interaction of the secondary particles with the detector
medium or the roof are also not parallel to the interacting particles as shown in the Figure 3.15.
This skewed angle criterion rejects these events as well.

3.5   Results and Discussions

In the present work, the event direction is presumed as a mean direction of all individual tracks
in an event. In the study, the clustering of events towards any specific region in the sky was
not observed for the data recorded in the detector, which can be confirmed by the Figure 3.16.
Also, no significant modulation of the fractions of multiple track events was observed during
the period of observation irrespective of periodic changes in trigger rate. Hence, the assump-
tion of the uniform distribution of the cosmic ray directions which are used in the CORSIKA
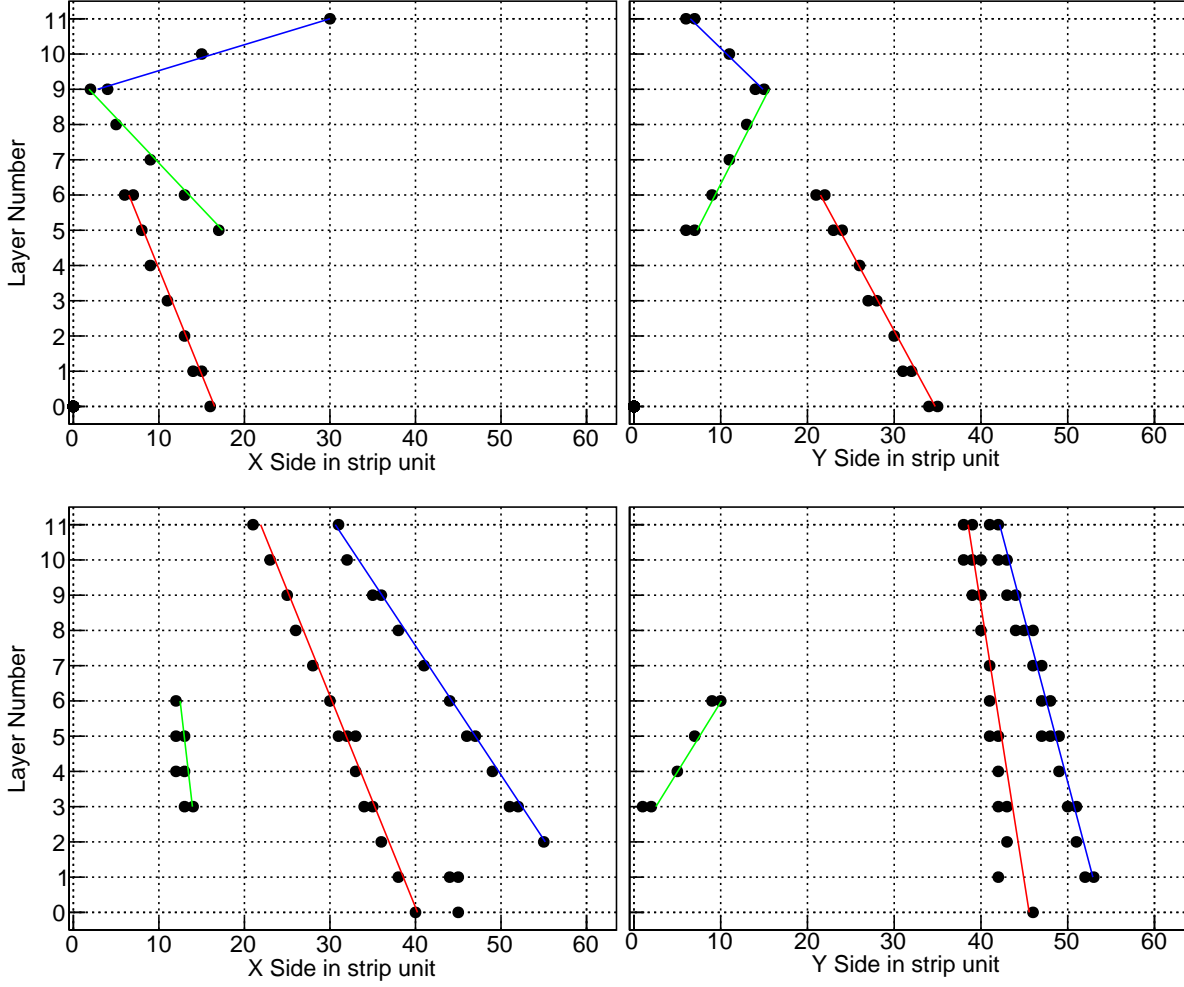
Figure 3.15: Events where the secondary cosmic ray interacted with the detector medium and roof generating multiple particles.

simulations are justified by the absence of anisotropy in the data.

The total number of events with at least one reconstructed track in it is approximately 206 millions. The normalised fraction of the events containing 2, 3 and 4 tracks with respect to single track events are calculated to be $6.35\pm0.05\times10^{-5}$, $5.82\pm0.53\times10^{-7}$ and $1.94\pm0.97\times10^{-8}$, respectively from the cosmic ray data.

The normalised fraction of the events containing 2, 3 and 4 tracks are also calculated from the CORSIKA simulation for different types of cosmic primaries (H, He, C, O, Si, and Fe) and for different hadronic interaction models (QGSJET-II-04 and QGSJET01d), which are shown in the Table 3.1. In order to compare the simulated results with data, all the normalised fraction, calculated for different cosmic primaries are summed with weights where the abundances in the primary composition[27, 63] are used as the weights. The comparison of the data and the

Figure 3.16: Reconstructed direction of the tracks in the detector observed for the data recorded in the detector.

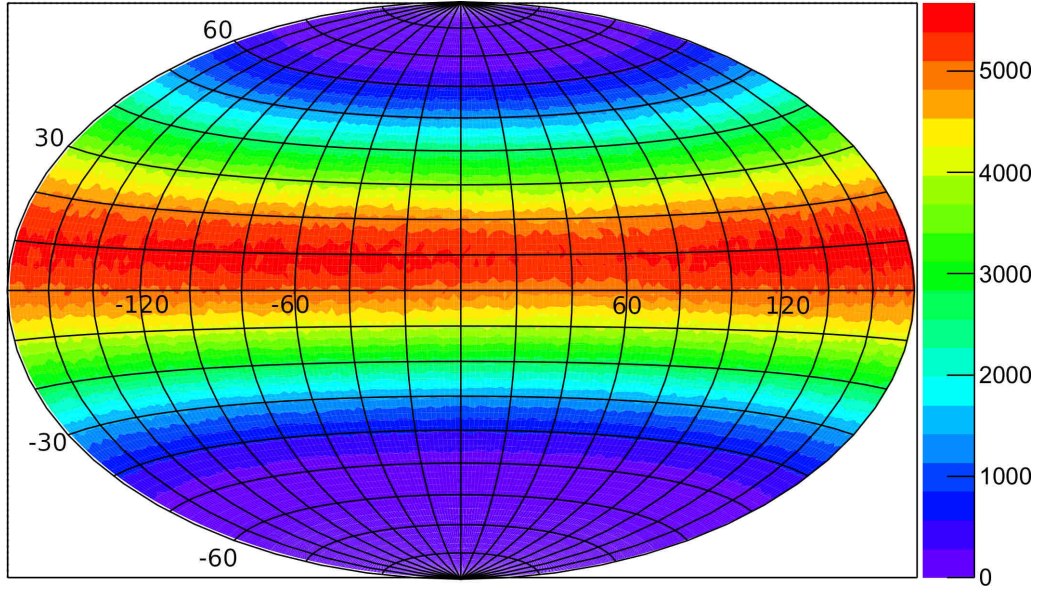| No of Tracks	H	He	C	O	Si	Fe
	QGSJET-II-04					
2	$2.19 \pm 0.12 \times 10^{-5}$	$4.71 \pm 0.19 \times 10^{-5}$	$1.21 \pm 0.02 \times 10^{-4}$	$1.61 \pm 0.02 \times 10^{-4}$	$2.42 \pm 0.02 \times 10^{-4}$	$4.58 \pm 0.03 \times 10^{-4}$
3	$1.02 \pm 0.12 \times 10^{-7}$	$3.04 \pm 0.17 \times 10^{-7}$	$1.78 \pm 0.05 \times 10^{-6}$	$3.11 \pm 0.06 \times 10^{-6}$	$5.57 \pm 0.08 \times 10^{-6}$	$1.61 \pm 0.02 \times 10^{-5}$
4	$1.61 \pm 0.65 \times 10^{-9}$	$8.80 \pm 2.46 \times 10^{-9}$	$5.83 \pm 0.47 \times 10^{-8}$	$1.12 \pm 0.07 \times 10^{-7}$	$2.35 \pm 0.11 \times 10^{-7}$	$1.02 \pm 0.03 \times 10^{-6}$
	QGSJET01d					
2	$2.14 \pm 0.12 \times 10^{-5}$	$4.74 \pm 0.13 \times 10^{-5}$	$1.19 \pm 0.02 \times 10^{-4}$	$1.52 \pm 0.02 \times 10^{-4}$	$2.50 \pm 0.02 \times 10^{-4}$	$4.56 \pm 0.03 \times 10^{-4}$
3	$9.13 \pm 1.22 \times 10^{-8}$	$3.91 \pm 0.18 \times 10^{-7}$	$1.90 \pm 0.04 \times 10^{-6}$	$3.14 \pm 0.08 \times 10^{-6}$	$6.19 \pm 0.07 \times 10^{-6}$	$1.65 \pm 0.02 \times 10^{-5}$
4	$0.75 \pm 0.38 \times 10^{-9}$	$6.48 \pm 1.38 \times 10^{-9}$	$6.00 \pm 0.43 \times 10^{-8}$	$1.07 \pm 0.07 \times 10^{-7}$	$3.39 \pm 0.11 \times 10^{-7}$	$1.16 \pm 0.03 \times 10^{-6}$

Table 3.1: Fraction of track with 2, 3 and 4 tracks obtained from Simulation for different primaries (H, He, C, O, Si and Fe) and different physics packages (QGSJET-II-04 and QGSJET01d).

combined predictions are given in the Table 3.2.

If the abundances of elements in the primary cosmic ray spectrum as observed in [27, 63] are used to estimate the final results from simulation, the normalised track fractions of the events containing 2, 3 and 4 tracks are order of magnitude less than the data. The systematic error due to the uncertainties of roof thickness, material in the detector setup, strip multiplicity, noise and efficiencies are much smaller than the observed discrepancy between data and MC

No of Tracks	Data	QGSJET-II-04	QGSJET01d
2	$6.35 \pm 0.05 \times 10^{-5}$	$2.35 \pm 0.13 \times 10^{-5}$	$2.37 \pm 0.12 \times 10^{-5}$
3	$5.82 \pm 0.53 \times 10^{-7}$	$1.12 \pm 0.13 \times 10^{-7}$	$1.23 \pm 0.13 \times 10^{-7}$
4	$1.94 \pm 0.97 \times 10^{-8}$	$3.21 \pm 0.87 \times 10^{-9}$	$2.43 \pm 0.50 \times 10^{-9}$

Table 3.2: Comparison of track fraction with 2, 3 and 4 tracks obtained from Data and simulation, with combined fractions as par abundances of cosmic ray particles.

prediction. These results clearly demonstrate that there is a discrepancy between the observed data and predictions from cosmic ray particle spectrum, the CORSIKA and finally the GEANT4 simulation.

A few other experiments (KGF[64], ALICE[65], MACRO[66], DELPHI[67], ALEPH[68], KASCADE-Grande[69], etc.) have also studied the multi-muon tracks in the cosmic events in the respective detectors. Except for the KASCADE-Grande, all other experiments were performed under the ground. The underground experiments have observed events with large multiplicities because of the large size of the detectors and the overburden of rock and soil, which block showers with low energy. The multiplicity of the cosmic ray particles observed in a detector is highly dependent on the dimensions, aperture, energy threshold and the detector's location. Hence, it is difficult to compare the results of the aforesaid experiments quantitatively with the small-scale detectors setup in this current study. But all the studies based on the aforesaid experiments have also indicated a similar discrepancy between the CORSIKA spectra and the observed data. The KASCADE-Grande experiment has also concluded that the attenuation length of muons in the atmosphere from the simulation is much smaller than estimation from the observed data[69].

Although, the bulk of primary particles interacts at center-of-mass energies far below $10\,\mathrm{GeV}$ [55], it is observed in the simulation that a significant amount of primaries which are responsible for higher particle multiplicities in the present setup, are in the range beyond the scope of the present collider experiments. The major problem of the EAS simulation programs is the extrapolation of the hadronic interactions in the high energy range which is not covered by the experimental data. The limitation of the experiments in measuring the hadronic interactions at this high energy is mainly due to the limitation of the design of high energy $p\bar{p}$-colliders [55]. In the present $p\bar{p}$- or $p\,p$-colliders, the forward direction is not accessible. The secondary particles which are of the higher importance in the development of EAS programs are undetected in the beam pipe of the colliders. The largest energy fraction of each $p\bar{p}$-collision is carried away by these particles. The maximum attainable energy in these colliders is much lower than those found in cosmic rays. Therefore, the extrapolations based on theoretical models are mainly used by all the EAS programs. While, the energy of the cosmic rays contributing

for the single track events in the current detector setups are well within the boundary of the
current physics models (up-to ~1 TeV), a significant amount of the interactions contributing
for the higher multiplicities are beyond this energy and are not supported by the experimental
data [55].

3.6   Chapter Summary

An experimental setup consisting of 12 layers of glass RPCs of the size of 2 m × 2 m has been
built at IICHEP-Madurai. The cosmic ray data recorded by this detector setup is used to analyse
the secondary cosmic rays reaching the surface of the Earth. In this current study, we probed the
multiplicity of the particles passing through the detector. The recorded data is compared with
the Monte-Carlo simulations. In the period between August 23, 2017 to September 8, 2017,
approximately two hundred million cosmic ray events were recorded. As it is shown above, the
analysis showed a discrepancy in the result predicted by the EAS simulation program which can
be observed in the comparison of the track multiplicity between the data and Monte-Carlo. The
results of the current study reflect that the current physics models of interactions at the Earth's
atmosphere are unable to reproduce the air showers accurately. The earlier measurements of
the muon multiplicity along with the present result can be used to improve the parameters of
the hadronic models at the high energies and/or the cosmic ray spectral index along with the
composition of the primary cosmic rays.

The work presented in this chapter is published in [70].

Chapter 4

Charge Ratio of Atmospheric Muons at IICHEP-Madurai

The study of atmospheric muon charge ratio $\left(R_\mu = N_{\mu^+}/N_{\mu^-}\right)$ is important to the measurement of the neutrino flux precisely, alongside the relevant information in the composition of the primary cosmic rays and the different mechanisms of matter particle interactions.

The shower of secondary particles consists mainly of pions $\left(\pi^\pm, \pi^0\right)$ and kaons $\left(K^\pm, K_S^0, K_L^0\right)$ which are produced due the interactions of primary cosmic rays consisting of mainly proton and a small fraction of higher Z atoms [27, 63] with atmospheric nuclei at the upper atmosphere (mostly at 15-20 km altitude). The neutral pions mainly decay via electro-magnetic interactions, $\pi^0 \rightarrow \gamma + \gamma$ whereas the charged pions decay to muons and neutrinos via weak-interactions, $\pi^+ \rightarrow \mu^+ + \nu_\mu$ and $\pi^- \rightarrow \mu^- + \bar{\nu}_\mu$. The kaons also decay to muons, neutrinos and to pions in different branching fractions. Most of the pions and kaons decay in flight and do not reach the Earth's surface. A small fraction of resultant muons decay into electrons and neutrinos, $\mu^+ \rightarrow e^+ + \nu_e + \bar{\nu}_\mu$ and $\mu^- \rightarrow e^- + \bar{\nu}_e + \nu_\mu$. The γ, $e^\pm$ do not reach the detector directly as they interact with atmospheric nuclei as well as the roof of the laboratory and generate electromagnetic showers, which can be easily distinguished from the muon trajectory in the RPC stack.

Hence, the cosmic ray muons are the most abundant charged particles available at the surface of the Earth. The relativistic muons lose about 2 GeV in ionisation before reaching the sea

level. As the primary cosmic rays are dominated by the proton, air molecule contains proton and neutron, the production of the positively charged kaons/pions/muons are more favoured. Hence the muon charge ratio reflects the excess of π^+ over π^- and K^+ over K^- during the formation of the cosmic ray showers in the forward region. In the TeV range however, the associated production of K^+ ($p + air \rightarrow K^+ + \Lambda + ...$), which has no analog for K^-, largely favours K^+ production over K^-, making the K^+/K^- ratio greater than π^+/π^- ratio [71].

Thus the charge ratio increases with the increasing kaon contribution with the increasing energy of the primary cosmic rays. The measurement of the charge ratio in TeV range thus, allow to limit the production of kaons inaccessible to the collider experiments at present, which is essential for better prediction of neutrino flux and $\nu_\mu/\bar{\nu}_\mu$ ratio.

One of the main aspects of ICAL detector is to distinguish between the μ^+ and μ^- passing through the magnetised iron medium, which is required in determining the mass-hierarchy of the neutrinos with low statistics cosmic neutrino events. So before deploying the main ICAL, a few prototypes of the detector are planned to be build in order to test various aspects. As a part of the ICAL R&D program, a magnetised detector (mini-ICAL) with 10 layers of RPCs has been built and operational at IICHEP, Madurai is situated near the INO site. Being a scale-down model of the ICAL detector, the mini-ICAL is being studied as the prototype of the magnetised ICAL. This prototype is mainly built to study the performance of electronics equipment in the presence of the magnetic field and to test the event reconstruction algorithms. The cosmic ray data collected by the detector setup is also used to calculate the charge ratio (R) of the number of μ^+ to μ^- arriving at the Earth's surface. The testing of the INO-ICAL muon reconstruction algorithms is also another motivation behind this study. By comparing the result from cosmic ray data with extreme air shower (EAS) simulation, this study also signifies the ability of the magnet in identifying the charge of the particle.

4.1 Detector Setup of mini-ICAL

The present setup, named mini-ICAL, is a magnetised iron calorimeter weighing at 85 Tonn. The mini-ICAL detector consists of 11 layers of iron of size $4\,\text{m} \times 4\,\text{m} \times 5.6\,\text{cm}$ with the inter-

layer gap of 4.5 cm. This makes the dimensions of this prototype detector are $4\,m \times 4\,m \times 1.06\,m$. The detector setup is shown in the Figure 4.1. The iron layers in the mini-ICAL magnet is made
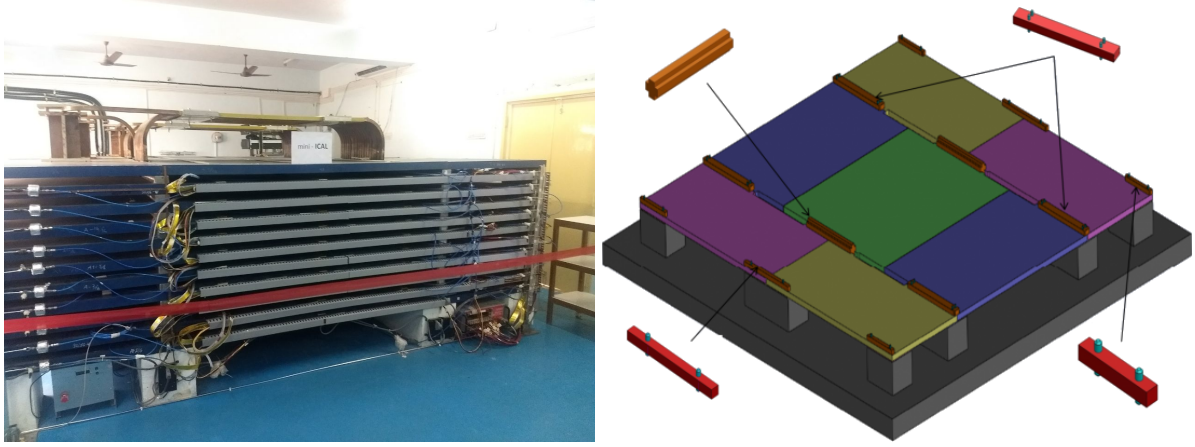

Figure 4.1: (Left) The mini-ICAL Detector Setup (right) and the different sections of one layer of iron and the stainless-steel spacers.

of soft iron with the additional chemical composition of C (0.015%), Mn (0.37%), P (0.012%), S (0.008%), Si (0.188%), Al (0.001%), N (50 ppm). This soft iron has low carbon content which makes it strong enough mechanically to support its own weight, but also allows it to have high permeability with knee point at around ~1.5 T. Each of the layers of iron consists of several different tiles shown in the Figure 4.1. The gap between the layers is maintained with the help of the spacers made of non-magnetic stainless steel (SS-304) are also shown in the Figure 4.1.

There are four slots with dimensions of $80\,cm \times 8\,cm$ to accommodate two sets of current conducting coils to generate magnetic field inside the iron in a similar fashion to the proposed ICAL detector. The coils are made of OFE-grade copper with oxygen content less than 10 ppm. There are 18 turns of coils in each set of coils. Each of the turns are kept at a distance of 40 mm. The coils are hollow inside with the cross section of $30\,mm \times 30\,mm \times \phi17\,mm$. The two sets of coils are electrically connected in series, and a low voltage power supply is used to supply 900 Amp of trough via the coils. A uniform magnetic field of ~1.5 T is obtained in the central region of the detector. The strength of the magnetic field in the iron layer along the X- and Y-axis are shown in the Figure 4.2. It can be seen that most of the field strength is present in the central region of the detector along the (-)Y-direction.

The heat generated by the current in the coils is extracted by a closed-loop low conductivity water cooling system (LCWCS) by flowing chilled water through the bore of the coils.
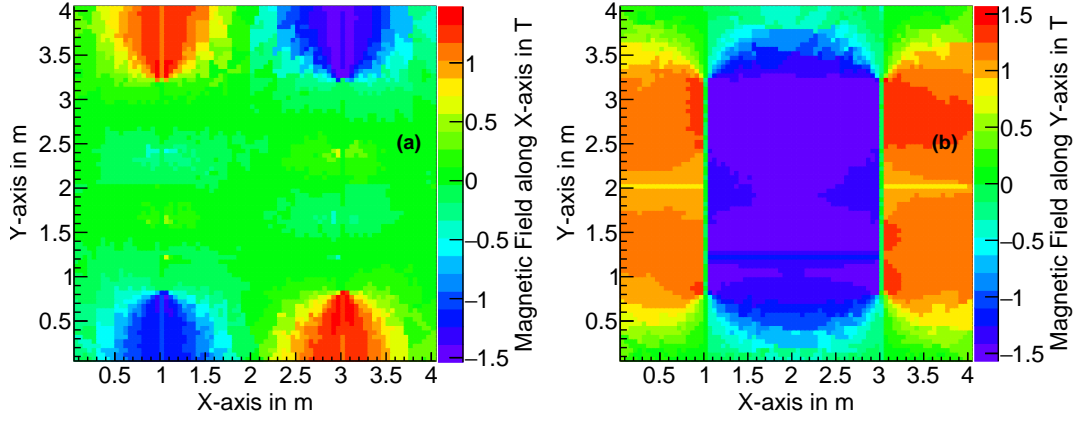
Figure 4.2: The strength of magnetic field in the iron layer along (a) X- and (b) Y- axis.

Ten RPCs of dimensions $174\,cm \times 183.5\,cm$ are used as the active detector. These RPCs are placed in the central region of the detector in between iron layers. An RPC gap is made of two glass electrodes of thickness $3\,mm$ with a gap of $2\,mm$ between them. Uniform gap between these two electrodes is maintained using an array of $2\,mm$ thick poly-carbonate buttons. The glass gap is sealed on the outer edges to make it air-tight. A mixture of gases with the compositions of R134a (95.2%), iso-C_4H_{10} (4.5%) and SF_6 (0.3%) is flown in the RPCs via strategically placed nozzles. This mixture of gasses serves as the target medium of the detector. Both the outer surfaces of the glass gap are coated with a thin layer of graphite. The RPCs are operated by applying a differential supply of $\pm 5\,kV$ to the graphite layers which creates a constant electric field between the glass electrodes. The ionisation of the gas mixture by passage of the charged particles eventually evolves into a avalanche in the presence of the high electric field between the glass electrodes. The avalanche in the RPCs induces signals in the two orthogonal pickup panels placed on both sides of the glass gaps labelled as X-side (bottom panel) and Y-side (top panel). The pickup panels are made of parallel copper strips of width $28\,mm$ with $2\,mm$ gap between two consecutive strips. There are 58 strips on the X-side and 61 strips on the Y-side for each layer.

The DAQ system is similar to the setup discussed in the previous chapter. In this case the cosmic muon data have been collected using the 1-Fold signals from the top 4 layers as trigger. An event data typically contains strip hit and timing information of an event. The strip hit is basically one logic bit per strip indicating the signal in that strip is above the threshold value for that strip. The least count of each of the TDC is $0.1\,ns$. The timing data consist of 16

time signal for each layer where each multi-hit TDC channel records time signals coming from every alternate 8th strips on one side of the layer. The time signal of each hit is recorded for both the leading-edge and the trailing-edge of the induced signal pulse.

4.2 Monte-Carlo Simulation

The Monte-Carlo Simulation for this study has been executed in two parts. The Extensive Air Shower (EAS) has been simulated by the CORSIKA simulation package[55]. The information of daughter particles generated by the EAS at the Earth's surface level has been extracted and used in the detector simulation. The detector simulation has been executed with the help of the GEANT4 toolkit[56]. The schemes of the EAS and the detector simulations are already elaborated in the Chapter 3.

In this study, for simulating the behaviour of hadrons for higher energy range, the SIBYLL has been adopted and for the low energy range, the FLUKA model has been used [55]. The primary cosmic ray shower has been simulated using the CORSIKA(v7.6300) Package. The energy of the primary rays in the CORSIKA is generated using the power-law spectrum, $E^{-2.7}$, within the energy range of 10–10^6 GeV. The zenith and azimuth angle of primary particles are generated uniformly within the range of 0–85° and 0–360°, respectively. The magnetic rigidity cutoff has been implemented according to the location of the detector.

An identical model of the detector, including the building in which it is housed, is prepared in the GEANT4 in order to perform the detector simulation. The material in the simulation is chosen as per the material present in the setup. The model of the setup in GEANT4 is shown in the Figure 4.3. In the detector simulation; the momentum value and the direction of the muons are randomly generated from the CORSIKA spectra. The detector's parameters (efficiency, noise, strip multiplicity and resolution) are calculated using the cosmic ray data without magnetic field in the detector.

Both the events from the observed cosmic ray data and the detector simulation are reconstructed using the track fit algorithm which is discussed in the next section.
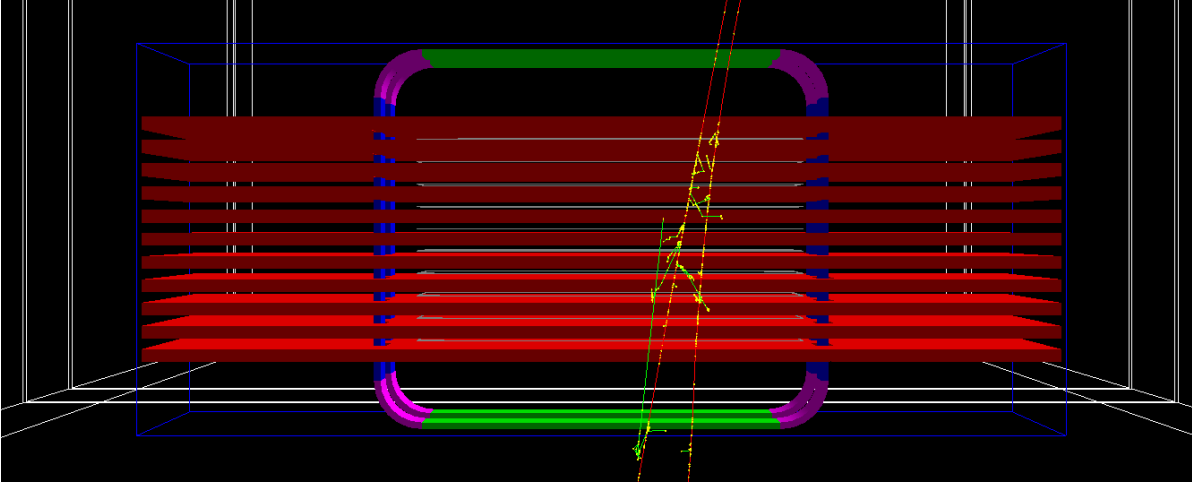
Figure 4.3: Model of the miniICAL magnet system in GEANT4.

4.3   Event Reconstruction and Data Selection

The recorded data is actually the projection of the track on the X–Z and Y–Z sides. During the passage of a charged particle through a RPC gap, the number of strips on which a signal is induced depends on the gain of the gas gap at the place of passing. This sharing of the induced signal between the neighbouring strips is one of the main reasons for the observed strip multiplicity shown in the Figure 3.7(c), whereas other reasons are streamer pulse as well as correlated electronics noise. In order to prepare the events for analysis, the consecutive strips which have recorded signals are clubbed together to form a cluster. The layers with no clusters either or both on X and Y sides are neglected during the track reconstruction.

During the study, the position resolution for strip multiplicities of 1, 2 are ~6 mm. In this study, the clusters of hits with more than 2 multiplicities are neglected as the position resolution for higher multiplicities is found to be the worse. A layer which has more than 15 strip hits and/or more than 10 clusters is tagged as 'noisy layer' and not considered in the track reconstruction. An event which has more than 3 noisy layers is considered as a 'noisy event' and discarded.

A few such events are displayed in the Figure 4.4.

The clusters present in an event then are reconstructed using different reconstruction algorithms to find the momentum of muons which are discussed in the following.
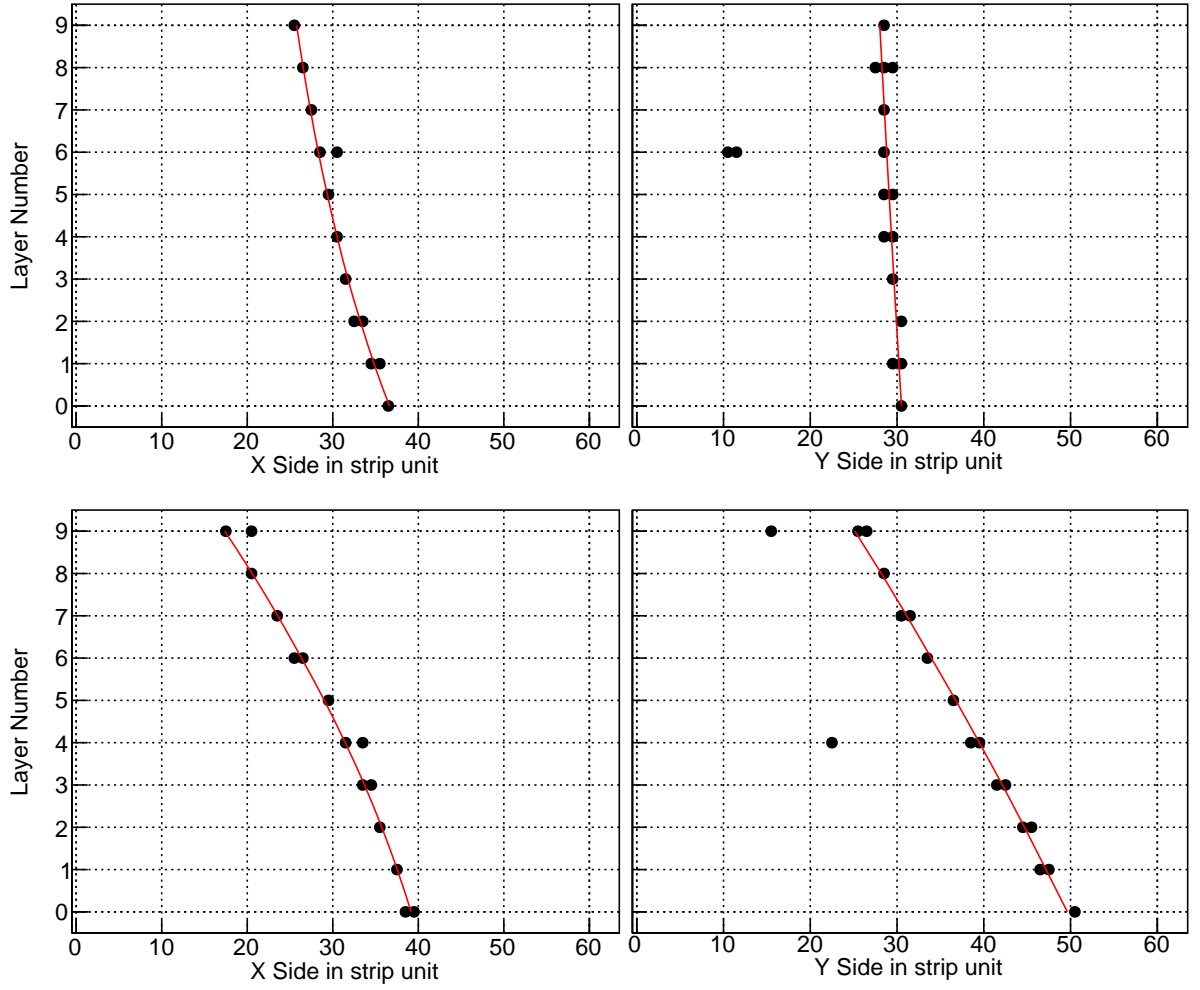
Figure 4.4: Two events with reconstructed track with opposite charge.

4.3.1 Circle Fit

As it was shown earlier, the strength of the magnetic field in the X-direction is very small. So, almost no significant bending is observed in the Y-side of the track which makes the projection of the track on the Y-side to be fit with a straight line. Thus, in the first step of track reconstruction, the clusters on the Y-side associated with the tracks are found and grouped using the method of Hough Transformation[61]. This eliminates the possibility of noise hits on the Y-side getting included in the track reconstruction. Once one valid straight track is found, attention is given on the X-side of the track. As the magnetic field is mainly in the Y-direction, maximum bending of track is observed on the X-side. The clusters on the X-side are then fitted with a circle. The information of the fitted circle helps to reject the noise hits on the X-side as well. Using the radius (r in meter) of the fitted circle, the transverse momentum (p_t in GeV) of

the particle can be roughly estimated by the following equation,

$$p_t = 0.3Br \tag{4.1}$$

where, B is the average magnetic field in Tesla.

The information of the fitted straight line on the Y-side and the circle on the X-side are further used to calculate the direction (zenith and azimuth) of the incident particle. From the direction and the p_t value, the value of the momentum of the particle is estimated.

The events with muons are simulated using GEANT4. The hits obtained at the GEANT4 simulation have been fitted using this method. The estimated momentum vs the generated momentum is shown in the Figure 4.5(a).
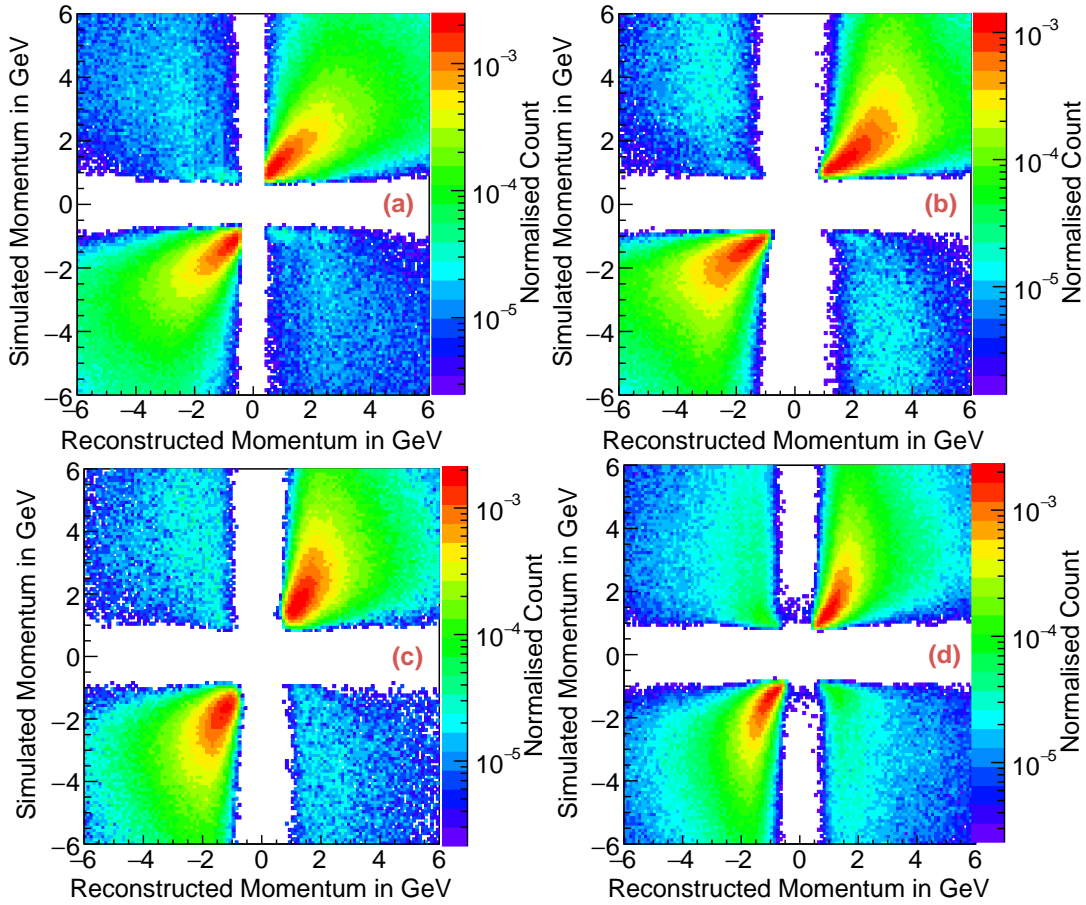

Figure 4.5: Generated momentum vs reconstructed momentum using (a) Circle Fit, (b) Grid-Search, (c) Explicit Track-Model and (d) Kalman-filter.

4.3.2   Grid-Search Method

The information from circle gives the rough estimate of the transverse momentum (p_t) component of the momentum is calculated using the radius of the circle. Combining the fit information from X-Z and Y-Z plane, the track parameters i.e. two position and three momentum components (such as x, y, p_x, p_y, p_z) are calculated. Whereas, the estimated track parameters from above information can be well taken, if there is no energy loss of the particles in detector medium and uniformity of the magnetic field throughout the area. To get the correct values of the track parameters, the energy loss of the material and the non-uniformity in the magnetic field has to be taken care of in the track fitting.

To serve the purpose, the rough track parameters estimated from the circle and straight line fit is fed as seed for the track propagation, which is performed by solving the equation of motion of charged particle in a magnetic field.

By using the s as the free parameter, the equation of motion as given by Lorentz force becomes,

$$\frac{d^2\mathbf{r}}{ds^2} = \frac{q}{p}\frac{d\mathbf{r}}{ds} \times \mathbf{B}(\mathbf{r}) = \lambda(\mathbf{T} \times \mathbf{B}(\mathbf{r})) \tag{4.2}$$

where $\mathbf{T} = d\mathbf{r}/ds$ is the normalised tangent vector to the track, $\mathbf{B}(\mathbf{r})$ is the magnetic field and $\lambda \sim q/p$. The derivative $d\mathbf{r}/ds$ becomes $d\mathbf{r}/vdt = \mathbf{v}/v = \mathbf{T}$.

Analytical solution of the Eqn. 4.2 for a given non-homogeneous magnetic field is impossible. Thus numerical solutions are calculated. There are many numerical methods, among them one group of methods used in tracking is Runge-Kutta Method. For this purpose, the fourth order Runge-Kutta-Nystrom [72] method is adapted.

The step size in the propagation is 3 mm, which includes iron as well as other material. After propagation, the measurement vector ($x(z), y(z)$) are compared with predicted, where the propagation is done using energy loss of muons in the detector medium. The best fit parameters (x, y, p_x, p_y, p_z) for an event is taken when the overall χ^2 for X- and Y-plane is minimum. This estimation is done by varying the initial seed track parameters and then the particle is propagated one by one and done for all five parameters.

The hits obtained at the GEANT4 simulation have been reconstructed using this method.

The constructed momentum vs the generated momentum is shown in the Figure 4.5(b).

4.3.3   Explicit Track Model Fit

The momentum was also reconstructed by the global track fitting using the least-squares method (LSM) [73]. The track model is the set of solutions of the equation of motion. The track model in the LSM is the linear expansion of the function $f(p)$, where f is a deterministic function of the track parameter p. At a reference surface, p is defined by the (x, y) coordinates and the momentum vector. As per the first approximation,

$$f(p) = f(p_0) + A \cdot (p - p_0) + O(p - p_0)^2 + \cdots \tag{4.3}$$

where $A = \frac{\partial f(p)}{\partial p}$ at $p = p_0$.

In the track model, the weight-matrix W is defined as the inverse of the covariance-matrix V. Since the measurement errors are uncorrelated, then

$$(W)_{ij} = \frac{\delta_{ij}}{\sigma_j^2} \tag{4.4}$$

where σ_j is the standard deviation on the jth measurement. But Generally, W will have non-zero off-diagonal terms in the case of multiple scatterings. During the track reconstruction, the LSM tries to minimise the function,

$$\chi^2 = [f(p_0) + A \cdot (p - p_0) - m]^{\text{T}} \cdot W \cdot [f(p_0) + A \cdot (p - p_0) - m] \tag{4.5}$$

where,

$m = m(_i)$, vector of measurements, e.g., θ, ϕ (2×N, number of track points)

$f = (f_i)$, vector of function corresponding to m, e.g., $\{x, y, dx/dz.dy/dz, q/p\}$

V, the covariance matrix of m, e.g., inverse of error matrices, (both position and effect of multiple scattering)

p_0, the approximate initial value of track parameters

$A = \partial f / \partial p$, at the point p_0

The solution of the least-squares problem,

$$p = p_0 + (A^T V^{-1} A)^{-1} A^T V^{-1} (m - f(p_0))$$

and covariance matrix of p, $C(p) = (A^T V^{-1} A)^{-1}$.

The initial values of the track parameters are assigned to this fit using a similar method discussed in the beginning of the Grid-Search. The constructed momentum vs the generated momentum in the GEANT4 is shown in the Figure 4.5(c).

4.3.4 Kalman-Filter Fit

This reconstruction method is a Kalman-filter based algorithm, where every track is initiated by a state vector $X_0 = (X, Y, dX/dZ, dY/dZ, q/p)$. The state vector contains the position of the starting hit (X, Y, Z), the charge-weighted inverse momentum which is taken to be zero and the initial direction (the slopes dX/dZ, dY/dZ) which is estimated from the first two layers. The initial state vector is then extrapolated to the next layer using an extrapolation algorithm based upon the equation of motion of a particle in a magnetic field. The extrapolated state vector is then filtered and improved using the Kalman-filter based algorithm. In this algorithm, the corresponding error propagation is predicted by a propagation matrix [74]. The Kalman-filter also takes the process of the multiple-scattering as described in [75] and the energy loss in matter according to the Bethe formula [76]. The extrapolated point is then judged with the actual position of the hit in that layer, if any, and the process is iterated. The best fit track is obtained from the complete iteration. The q/p determines the magnitude of the momentum along with the reconstructed direction using dX/dZ and dY/dZ, which are the zenith and azimuth angles respectively.

In short, State vector at any step is the combination of extrapolation from previous measurement and measurement at that point,

$$p_k^k = K_k^1 p_k^{k-1} + K_k^2 m_k, \qquad\qquad p_k^{k-1} = F_{k-1} p_{k-1}$$

where, K_k^1 and K_k^2 are two weight factors, p_k^{k-1} is the expected state vector from previous measurements. The weight factors is calculated (for true state vector, p) from the minimisation of

$$\chi^2 = (m_k - f(p))^T \, V^{-1} \, (m_k - f(p)) + (p - p_k^{k-1})^T \, (C_k^{k-1})^{-1} \, (p - p_k^{k-1})$$

which has the following matrix algebra for each step

$$
\begin{aligned}
V &= (V_k + A_k \, C_k^{k-1} \, A_k^T) \\
C_k^{k-1} &= F_{k-1} \, C_{k-1} \, F_{k-1}^T + Q_{k-1} \\
K_k &= C_k^{k-1} \, A_k^T (V_k + A_k \, C_k^{k-1} \, A_k^T)^{-1} \\
p_k &= F_{k-1} \, p_{k-1} + K_k(m_k - A_k \, F_{k-1} \, p_{k-1}) \\
p_k &= (I - K_k \, A_k) \, p_k^{k-1} + K_k \, m_k \\
C_k &= (I - K_k \, A_k) \, C_k^{k-1}
\end{aligned}
$$

where,

- p_k : State vector $\{x, y, dx/dz, dy/dz, q/p\}$, (5×1)

- C_k : State covariance matrix, (5×5)

- F_k : Propagator matrix of state vector p_k, (5×5)

- Q_k : Noise matrix due to multiple scattering/ionisation loss, (5×5)

- m_k : X(Y) position measurement, (2×1)

- V_k : Error matrix of m_k, (2×2)

- A_k : Measurement function ($\partial f / \partial p_k$ from experiment $m_k = f(p_k)$), (2×5)

- K_k : Kalman gain factor, (5×2)
  $K_k^1 = (I - K_k \, A_k)$ and $K_k^2 = K_k$

The hits obtained from the GEANT4 simulation are reconstructed using this method. The constructed momentum vs the generated momentum is shown in the Figure 4.5(d).

4.4 Charge Ratio Spectra of Cosmic Ray Muons

It can be observed in the Figure 4.5 that the particles with momentum less than 0.8 GeV are not reconstructed. This is because of the minimum momentum cutoff due to the minimum layer criteria of 7. Also the insignificant curvature of the tracks at higher momentum coupled with the strip width of the pickup panels, constrains the reconstruction for larger momentum.

In order to compare the the fit methods quantitatively, the Mean and RMS of the $\left(P_{reco} - P_{gen}\right)$ plot is calculated for different interval of P_{gen} values, which is shown in the Figure 4.6. It is
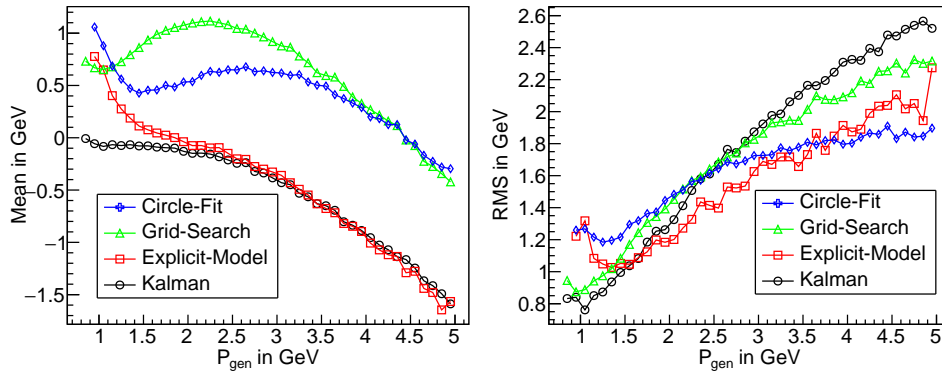

Figure 4.6: the Mean and RMS of the $\left(P_{reco} - P_{gen}\right)$ plot for different values of P_{gen}.

clear from plots in 4.5 that Kalman filter techniques shows a saturation of reconstructed momentum at around 2 GeV, which is mainly due to the large uncertainty in position measurement and limited number of measured points. That is true to some extent for the explicit Track-Model also. Due to the saturation of the magnetic field, there is a gradual shift in the mean of $\left(P_{reco} - P_{gen}\right)$ for these two cases. The circle fit has a bias mainly due to ionisation energy loss, which was not incorporated there. Apparent bias in Grid Search techniques is mainly due to momentum ranges in generated MC samples. But, there is almost no difference in RMS in those four fitting techniques due to larger tails in the distributions.

The $\left(P_{reco} - P_{gen}\right)$ plots for different intervals of P_{gen} are also fitted with *Landau* function. The maximum probable value (MPV) and σ of the plots are shown in the Figure 4.7. In the fitted μ (4.7(b)), the same bias is there for Kalman fit and explicit track fit models, whereas due to less effect of tails part, bias in the grid search model has reduced drastically. The apparent better σ in the 4.7(b) from Kalman fit and explicit track fit models are due to saturation effects, which is really not a good resolution.
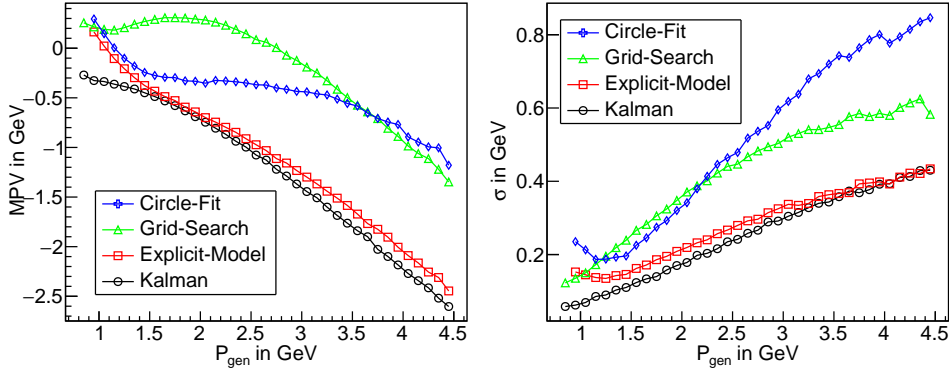
Figure 4.7: The MPV and σ of the $\left(P_{reco} - P_{gen}\right)$ plot for different values of P_{gen}.

Each model also has its limitation in the efficiency and the capacity of determining the charge of the particle. The efficiency is defined as the ratio between the number of particles reconstructed to that of particles generated provided the charge of the particles are identified properly. The efficiency of the fit methods are shown in the Figure 4.8(a). The amount of mis-identification of the charge of a particle is represented in the Figure 4.8(b).
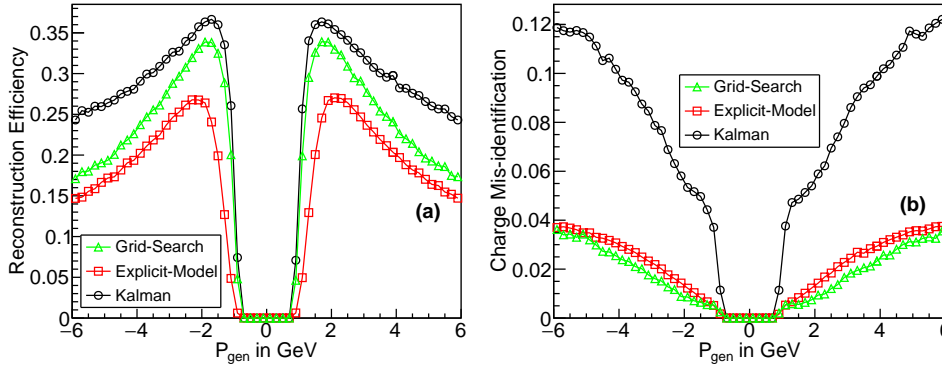

Figure 4.8: (a) Efficiency of the fit methods and (b) Particle charge mis-identification plotted against P_{gen}.

Taking the performance of the fit methods on the basis of charge mis-identification, overall momentum resolution and saturation of reconstructed momentum; the Grid Search Method has been accepted to further study the charge ratio of the cosmic ray muons.

The measured momentum spectra in the detector is biased because of the housing building covering the detector, limited acceptance of the detector, resolution and other systematic effects on the detector. This can be represented by the following equation,

$$\mathbf{A}\mathbf{x} + \mathbf{b} = \mathbf{y} \tag{4.6}$$

where, **A** is the 'response matrix', **x** is the 'truth' spectra, **b** is the 'background' and **y** is the 'measured' spectra. The procedure of estimating the *truth* spectra using known *response matrix* and *background* spectra is called data-unfolding. So to compare the experimental measurement with previous prediction, the reconstructed spectra is unfolded to eliminate the detector's effects. The unfolding method used for the current study is iterative Bayesian Unfolding [77].

In order to determine the number of iterations required in the unfolding process, the following procedures have been adopted.

- The MPV and σ, found in the case of Grid Search method (shown in the Figure 4.7), are used to smear the randomly generated momentum values. The generated and smeared values of the momentum are then filled in a histogram to create the response matrix, which is shown in the Figure 4.9(a).

- The above step is then repeated again with different seeds, but for this time to create the spectra to be unfolded. The spectra created using randomly generated momentum value is the *truth*, and the spectra created by using the smeared momentum is the *measured*.

- The *measured* spectra created in the previous step is then unfolded using the iterative Bayesian technique for different numbers of iterations. The unfolded spectra is then compared with the *truth*. The difference between the unfolded spectra and the *truth*, termed as χ^2, is plotted against the number of iterations which are shown in the Figure 4.9(b). It can be seen that the unfolding is minimised at iteration number 4.
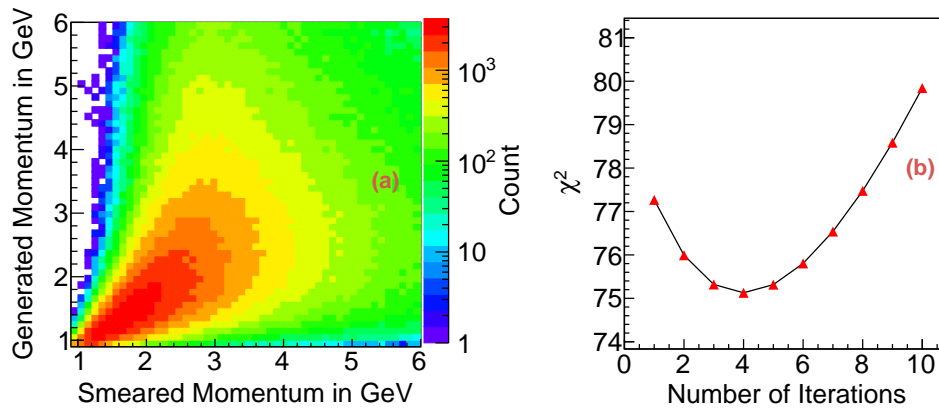

Figure 4.9: (a) Generated Response Matrix and (b) χ^2 vs Number of Iteration.

The cosmic ray events collected in the mini-ICAL detector are constructed using the Grid search method. The reconstructed momentum spectra is then unfolded using the response matrix calculated from GEANT4 simulation (shown in the Figure 4.5(c)). In the Bayesian technique, the background in each reconstructed momentum bin and efficiency of each true momentum bin are calculated. The reconstructed data and MC are also corrected for fake rate. The unfolded momentum spectra for μ^+ and μ^- is shown in the Figure 4.10(a). The charge ratio (R) of the atmospheric muons is then found by dividing the spectra for μ^+ with the spectra for μ^-, which is shown in the Figure 4.10(b).
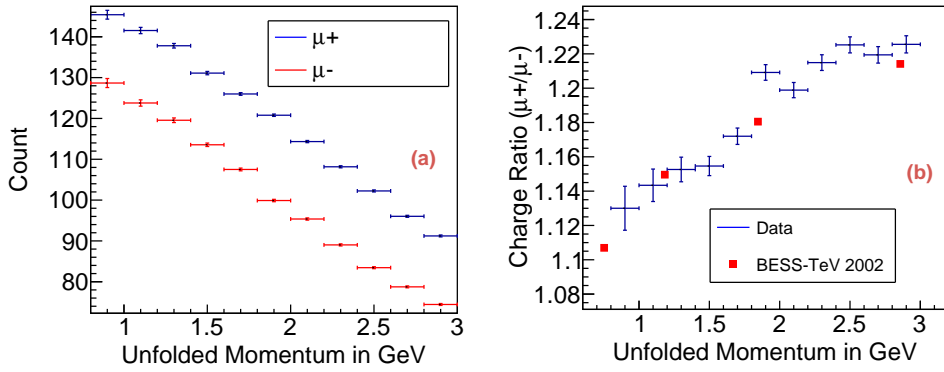

Figure 4.10: (a) Unfolded momentum spectra for μ^+ and μ^- reconstructed from data, (b) Charge ratio of muons compared with BESS-TeV'02 calculation [2].

The reconstructed spectra from data are unfolded up-to 3 GeV as the reconstructed energy saturates beyond this energy [78, 79]. A new detector setup, named as Engineering Module is going to be built in the near future. This setup is going to have 20 layers of RPC detectors. The Grid Search method is giving better results for a 10 layer setup, but it is taking too much time to simulate it. Also, is it expected that with larger hit points, explicit track fit model will give better resolution. Thus to reduce the reconstruction time explicit track fit model is used to reconstruct muons at 20 layers Engineering module. A preliminary simulation is performed with this setup by assuming the position of the RPCs in the central region of the detector. The events with more than 14 layers of hits are reconstructed. The response matrix found from this simulation is shown in the Figure 4.12. The efficiency of reconstruction and mis-identification of the charge of the particles are shown in the Figure 4.13. In the Engineering Module, the momentum should be reconstructed up-to 12 GeV along with better charge identification and particle detection efficiency.
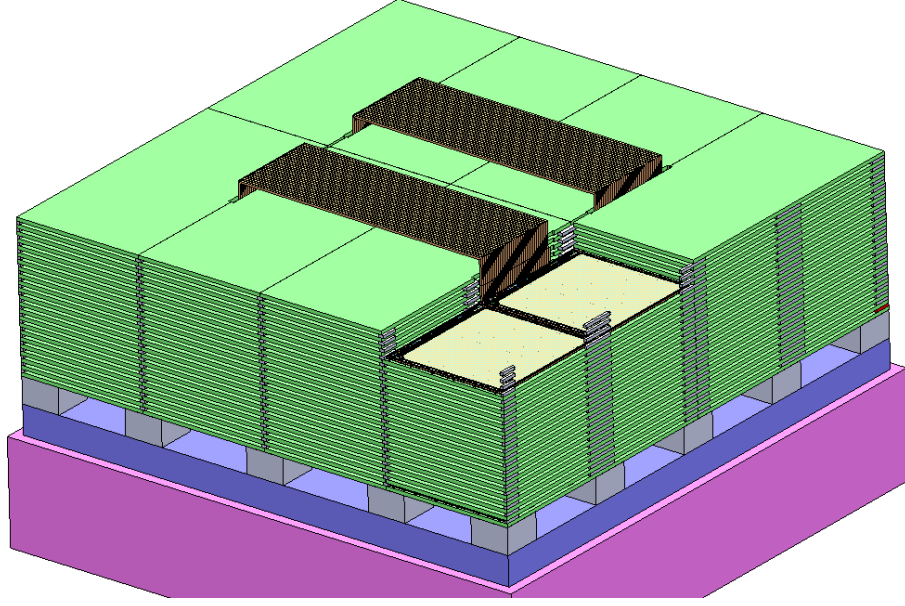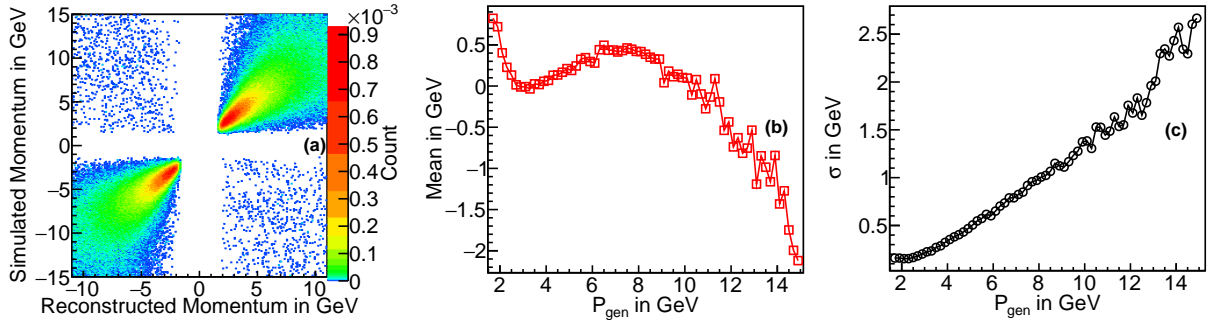
Figure 4.11: Model of the Engineering Module.

Figure 4.12: (a) Response Matrix, (b) Mean and (c) σ for the Engineering Module.

4.5   Chapter Summary

As a part of the ICAL R&D program, a magnetised detector (named mini-ICAL) with 10 layers of RPCs interspersed with 56 mm iron layers have been built and operational at IICHEP, Madurai situated near the INO site. The cosmic ray data collected by the detector setup is used to calculate the charge ratio (R) of the number of $\mu+$ to $\mu-$ arriving at the Earth's surface. Using the iterative Bayesian Unfolding technique, the charge ratio of muons is observed and compared with the BESS-TeV'02 calculation [2]. From the study, it is seen that the ratio between μ^+ and μ^- more or less matches in the range of 0.8-3 GeV. The reconstruction of momentum beyond this energy range fails due to the insignificant curvature of the tracks created by the particles, poor position resolution of RPCs, limited number of tracker layers and the low-energy cutoff in this detector setup.
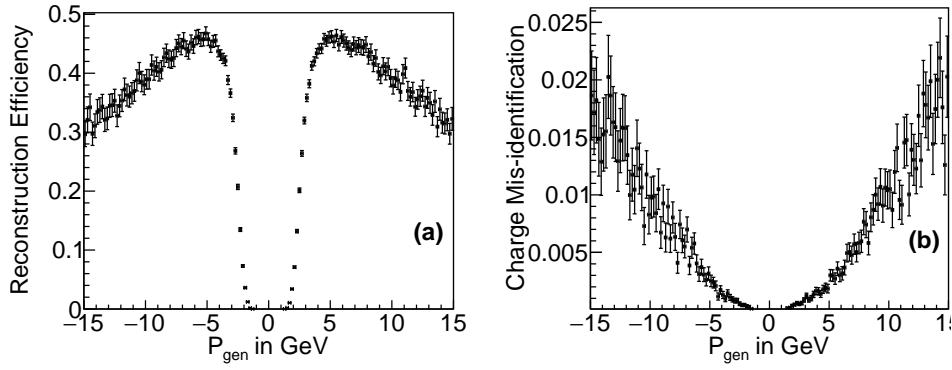
Figure 4.13: (a) Efficiency of reconstruction and (b) Particle charge mis-identification plotted against P_{gen} for Engineering Module.

A new detector setup with 20 layers of RPC and 8 times larger in volume, INO Engineering Module is going to be built in few years at IICHEP Madurai. With more detectors, the momentum should be reconstructed up-to 12 GeV with the same momentum resolution at ~3 GeV at present setup. That data will be able to compete with other experiments in the world to measure the momentum spectra and charge ratio of cosmic ray muons at the Earth's surface.

Chapter 5

Thesis Summary

The main goal of the INO-Collaboration is to investigate the neutrino oscillation in the atmospheric neutrinos with the ICAL detector. The ICAL is primarily designed to observe the CC-interactions of the $\nu_\mu/\bar{\nu}_\mu$s with the ability to distinguish between the charged leptons, mainly μ^+ and μ^-, which are being produced in the interactions. The research and development program is ongoing keeping the ICAL detector in the mind. Several prototype detectors have been built to study the performance and stability of the RPC detector and electronics. The detector's parameters like efficiencies of the RPCs, position and time resolutions of the detector, strip multiplicities and noise in the detectors, etc. are calculated using these detectors.

The RPCs in the ICAL detector are proposed to operate for more than 20 years. For the success of the experiment, each of the RPCs used in this experiment will be in operation without showing any significant degradation of performances during the period of operation. Hence, a proper leak test has to be performed on all the glass gaps at the time of production as well as during operation. The method of testing gaps for leakage and quantifying the leak is developed. The leak-test setups, both wired and wireless, are operational and are being used at various facilities and industries working along with INO-Collaboration. The test setups have decreased the average time required per gap significantly. The knowledge gained in this study also gives us more opportunity to better understand the structural integrity of the glass RPCs against various atmospheric parameters.

As a part of the ICAL R&D program, a 12 layer stack of $2\,\text{m} \times 2\,\text{m}$ RPCs has been opera-

tional at IICHEP, Madurai since the last few years to study the various detector properties. The cosmic ray data acquired at this stack is studied for charged-particle multiplicity. The charged-particle multiplicity in the obtained data is compared with the air shower simulation. The main aim of this study is to test the capability of the cosmic ray simulation packages. It reflects that the current physics models of interactions at the Earth atmosphere are unable to reproduce the air showers accurately. The earlier measurements of muon multiplicity which have similar conclusions along with the present result can be used to improve the parameters of the hadronic model at high energies and/or cosmic ray spectral index.

A magnetised detector (mini-ICAL) with 10 layers of RPCs also has been operational at IICHEP, Madurai to study the performance of electronics equipment in the presence of magnetic field and to test the event reconstruction algorithms. One of the motivations of the magnetised mini-ICAL detector was to estimate the muon charge ratio at Madurai and compare the result with the theoretical predictions which are very near to the INO site. The cosmic ray data collected by the detector setup is used to calculate the charge ratio (R) of the number of $\mu+$ to $\mu-$ arriving at the Earth's surface. Using the iterative Bayesian Unfolding technique the momentum spectra is made free of detector bias, and the charge ratio of muons is observed and compared with the BESS-TeV'02 calculation. From the study, it is seen that the ratio between μ^+ and μ^- more or less matches in the range of 0.8-3 GeV. The reconstruction of momentum beyond this energy fails due to the low-energy cutoff in this detector setup, the insignificant curvature of the tracks created by the particles, poor position resolution of RPCs and limited number of tracker layers. The result of this study can also be used to improve the hadronic interaction models and for better neutrino flux prediction. This study will also intend to improve the charge and momentum sensitivity in the ICAL detector.

References

[1] A Kumar, AM Vinod Kumar, Abhik Jash, Ajit K Mohanty, Aleena Chacko, Ali Ajmi, Ambar Ghosal, Amina Khatun, Amitava Raychaudhuri, Amol Dighe, et al. Invited review: Physics potential of the ICAL detector at the India-based Neutrino Observatory (INO). *Pramana*, 88(5):79, 2017. DOI: 10.1007/s12043-017-1373-4.

[2] Sadakazu Haino, T Sanuki, K Abe, K Anraku, Y Asaoka, H Fuke, M Imori, A Itasaki, T Maeno, Y Makida, et al. Measurements of Primary and Atmospheric Cosmic-Ray Spectra with the BESS-TeV Spectrometer. *Physics Letters B*, 594(1-2):35–46, 2004. DOI: 10.1016/j.physletb.2004.05.019.

[3] Allan Franklin. The road to the neutrino. *Physics Today*, 53(2):22–28, 2000. DOI: 10.1063/1.882961.

[4] ANToINE HENRI Bécquerel. Sur les radiations invisibles émises par les corps phosphorescents. *CR Acad. Sci. Paris*, 122:501–503, 1896.

[5] Ernest Rutherford. Uranium Radiation and the Electrical conduction Produced by it. *The London, Edinburgh, and Dublin Philosophical Magazine and Journal of Science*, 47(284):109–163, 1899. DOI: 10.1080/14786449908621245.

[6] CD Ellis and WA Wooster. The average energy of disintegration of radium E. *Proc. R. Soc. London*, 117 (776):109, 1927. DOI: 10.1098/rspa.1927.0168.

[7] Lise Meitner and Wilhelm Orthmann. Über eine absolute Bestimmung der Energie der primären β-Strahlen von Radium E. *Zeitschrift für Physik*, 60(3-4):143–155, 1930. DOI: 10.1007/BF01339819.

[8] L Meitner. Letter to C. D. Ellis. *cited in Sime*, page 105, 14 February 1928.

[9] Frederick Reines and Clyde L Cowan. The Neutrino. *Nature*, 178(4531):446–449, 1956. DOI: 10.1038/178446a0.

[10] Gaillard Danby, Jean Maurice Gaillard, Konstantin Goulianos, Leon M Lederman, N Mistry, M Schwartz, and J Steinberger. Observation of High-Energy Neutrino Reactions and the Existence of Two Kinds of Neutrinos. *Physical Review Letters*, 9(1):36, 1962. DOI: 10.1103/PhysRevLett.9.36.

[11] K Kodama, N Ushida, C Andreopoulos, N Saoulidou, G Tzanakos, P Yager, B Baller,

D Boehnlein, Walter Freeman, B Lundberg, et al. Observation of tau neutrino interactions. *Physics Letters B*, 504(3):218–224, 2001. DOI: 10.1016/S0370-2693(01)00307-0.

[12] Salvatore Mele. The measurement of the number of light neutrino species at LEP. In *60 Years of CERN Experiments and Discoveries*, pages 89–106. World Scientific, 2015. DOI: 10.1142/9789814644150_0004.

[13] Sheldon L Glashow. The renormalizability of vector meson interactions. *Nuclear Physics*, 10:107–117, 1959.

[14] Steven Weinberg. A model of leptons. *Physical review letters*, 19(21):1264, 1967. DOI: 10.1103/PhysRevLett.19.1264.

[15] Salam Abdus. Weak and Electromagnetic Interactions. *Conf. Proc.*, C680519:367–377, 1968.

[16] Sheldon L Glashow. Partial-symmetries of weak interactions. *Nuclear Physics*, 22(4):579–588, 1961. DOI: 10.1016/0029-5582(61)90469-2.

[17] FJ Hasert, Helmut Faissner, Wulf Dieter Krenz, J Von Krogh, D Lanske, J Morfin, K Schultze, H Weerts, Ghislaine Coremans, Jacques Lemonne, et al. Search for elastic muon-neutrino electron scattering. *Physics letters. Section B*, 46(1):121–124, 1973. DOI: 10.1016/0370-2693(73)90494-2.

[18] FJ Hasert, Helmut Faissner, Wulf Dieter Krenz, J Von Krogh, D Lanske, J Morfin, K Schultze, H Weerts, Ghislaine Coremans, Jacques Lemonne, et al. Observation of neutrino-like interactions without muon or electron in the gargamelle neutrino experiment. *Physics letters. Section B*, 46(1):138–140, 1973. DOI: 10.1016/0370-2693(73)90499-1.

[19] FJ Hasert, S Kabe, W Krenz, J Von Krogh, D Lanske, J Morfin, K Schultze, H Weerts, G Bertrand-Coremans, Jean Sacton, et al. Observation of neutrino-like interactions without muon or electron in the Gargamelle neutrino experiment. *Nuclear Physics B*, 73(1):1–22, 1974. DOI: 10.1016/0550-3213(74)90038-8.

[20] A Benvenuti, DC Cheng, D Cline, WT Ford, R Imlay, TY Ling, AK Mann, F Messing, RL Piccioni, J Pilcher, et al. Observation of Muonless Neutrino-Induced Inelastic Interactions. *Physical Review Letters*, 32(14):800, 1974. DOI: 10.1103/PhysRevLett.32.800.

[21] Christian Spiering. Towards high-energy neutrino astronomy. *The European Physical Journal H*, 37:515–565, 2012. DOI: 10.1140/epjh/e2012-30014-2.

[22] Steven Weinberg. *Gravitation and Cosmology*. John Wiley & Sons, New York, 1972.

[23] Raymond Davis Jr, Don S Harmer, and Kenneth C Hoffman. Search for neutrinos from the sun. *Physical Review Letters*, 20(21):1205, 1968.

[24] T Araki, S Enomoto, K Furuno, Y Gando, K Ichimura, H Ikeda, K Inoue, Y Kishimoto, M Koga, Y Koseki, et al. Experimental investigation of geologically produced antineutrinos with KamLAND. *Nature*, 436(7050):499–503, 2005. DOI: 10.1038/nature03980.

[25] G Bellini, J Benziger, S Bonetti, M Buizza Avanzini, B Caccianiga, L Cadonati, Frank Calaprice, C Carraro, A Chavarria, F Dalnoki-Veress, et al. Observation of geo-neutrinos. *Physics Letters B*, 687(4-5):299–304, 2010. DOI: 10.1016/j.physletb.2010.03.051.

[26] John N Bahcall. Solar Neutrinos. I. Theoretical. *Physical Review Letters*, 12(11):300, 1964. DOI: 10.1103/PhysRevLett.12.300.

[27] MM Shapiro, R Silberberg, and CH Tsao. Relative abundances of cosmic rays at their sources. In *Proceedings of the 11th International Conference on Cosmic Rays in 1969*, volume 1(29), page 479, 1970.

[28] B Pontecorvo. Mesonium and Antimesonium. *Sov. Phys. JETP.*, 6(2):429–431, 1957.

[29] B Pontecorvo. Neutrino Experiments and the Problem of Conservation of Leptonic Charge. *Sov. Phys. JETP.*, 6(2):984–988, 1968.

[30] Ziro Maki, Masami Nakagawa, and Shoichi Sakata. Remarks on the unified model of elementary particles. *Progress of Theoretical Physics*, 28(5):870–880, 1962. DOI: 10.1143/PTP.28.870.

[31] Makoto Kobayashi and Toshihide Maskawa. CP-violation in the renormalizable theory of weak interaction. *Progress of theoretical physics*, 49(2):652–657, 1973. DOI: 10.1143/PTP.49.652.

[32] Mathieu Ribordy and A Yu Smirnov. Improving the neutrino mass hierarchy identification with inelasticity measurement in pingu and orca. *Physical Review D*, 87(11):113007, 2013. DOI: 10.1103/PhysRevD.87.113007.

[33] SP Mikheyev and A Yu Smirnov. Resonance enhancement of oscillations in matter and

solar neutrino spectroscopy. *Yadernaya Fizika*, 42:1441–1448, 1985.

[34] Bruce T Cleveland, Timothy Daily, Raymond Davis Jr, James R Distel, Kenneth Lande, CK Lee, Paul S Wildenhain, and Jack Ullman. Measurement of the solar electron neutrino flux with the Homestake chlorine detector. *The Astrophysical Journal*, 496(1):505, 1998. DOI: 10.1086/305343.

[35] Wolfgang Hampel, J Handt, G Heusser, J Kiko, T Kirsten, M Laubenstein, E Pernicka, W Rau, M Wojcik, Yu Zakharov, et al. GALLEX solar neutrino observations: Results for GALLEX IV. *Physics Letters B*, 447(1-2):127–133, 1999. DOI: 10.1016/S0370-2693(98)01579-2.

[36] JN Abdurashitov, EP Veretenkin, VM Vermul, VN Gavrin, SV Girin, VV Gorbachev, PP Gurkina, GT Zatsepin, TV Ibragimova, AV Kalikhov, et al. Solar neutrino flux measurements by the Soviet-American gallium experiment (SAGE) for half the 22-year solar cycle. *Journal of Experimental and Theoretical Physics*, 95(2):181–193, 2002. DOI: 10.1134/1.1506424.

[37] Y Fukuda, T Hayakawa, E Ichihara, K Inoue, K Ishihara, Hirokazu Ishino, Y Itow, T Kajita, J Kameda, S Kasuga, et al. Measurement of the flux and zenith-angle distribution of upward throughgoing muons by Super-Kamiokande. *Physical Review Letters*, 82(13):2644, 1999. DOI: 10.1103/PhysRevLett.82.2644.

[38] Q R Ahmad et al. Measurement of the Rate of $\nu_e + d \rightarrow p + p + e^-$ Interactions Produced by ^8B Solar Neutrinos at the Sudbury Neutrino Observatory. *Phys. Rev. Lett*, 87:071301, 2001. DOI: 10.1103/PhysRevLett.87.071301.

[39] PF De Salas, DV Forero, CA Ternes, M Tortola, and JWF Valle. Status of neutrino oscillations 2018: 3σ hint for normal mass ordering and improved CP sensitivity. *Physics Letters B*, 782:633–640, 2018. DOI: 10.1016/j.physletb.2018.06.019.

[40] M Sajjad Athar, MS Bhatia, SC Ojha, HS Mani, SK Pal, AS Joshipura, DP Mahapatra, BK Nagesh, AK Mohanty, RK Bhandari, et al. India-based Neutrino Observatory: Project Report. Volume I. Technical report, 2006.

[41] R Santonico and R Cardarelli. Development of resistive plate counters. *Nuclear Instruments and Methods in physics research*, 187(2-3):377–380, 1981. DOI: 10.1016/0029-

554X(81)90363-3.

[42] Shiba P Behera, Manmohan S Bhatia, Vivek M Datar, and Ajit K Mohanty. Simulation studies for electromagnetic design of INO ICAL magnet and its response to muons. *IEEE Transactions on magnetics*, 51(2):1–9, 2014. DOI: 10.1109/TMAG.2014.2344624.

[43] Robert M Del Vecchio, Bertrand Poulin, Mary-Ellen F Feeney, Pierre T Feghali, Dilipkumar M Shah, Rajendra Ahuja, and Dillipkumar M Shah. *Transformer design principles: with applications to core-form power transformers*. CRC press, 2001.

[44] VM Datar, Satyajit Jena, SD Kalmani, NK Mondal, P Nagaraj, LV Reddy, M Saraf, B Satyanarayana, RR Shinde, and P Verma. Development of glass resistive plate chambers for INO experiment. *Nuclear Instruments and Methods in Physics Research Section A: Accelerators, Spectrometers, Detectors and Associated Equipment*, 602(3):744–748, 2009. DOI: 10.1016/j.nima.2008.12.129.

[45] S Pethuraj, VM Datar, G Majumder, NK Mondal, KC Ravindran, and B Satyanarayana. Measurement of cosmic muon angular distribution and vertical integrated flux by 2 m× 2 m RPC stack at IICHEP-Madurai. *Journal of Cosmology and Astroparticle Physics*, 2017(09):021, 2017. DOI: 10.1088/1475-7516/2017/09/021.

[46] Apache Software Foundation. MAGNET. 2008.

[47] S Colafranceschi, R Aurilio, L Benussi, S Bianco, L Passamonti, D Piccolo, D Pierluigi, A Russo, M Ferrini, T Greci, et al. A study of gas contaminants and interaction with materials in RPC closed loop systems. *Journal of Instrumentation*, 8(03):T03008, 2013. DOI: 10.1088/1748-0221/8/03/T03008.

[48] H Sakai, H Sakaue, Y Teramoto, E Nakano, and T Takahashi. Study of the effect of water vapor on a resistive plate chamber with glass electrodes. *Nuclear Instruments and Methods in Physics Research Section A: Accelerators, Spectrometers, Detectors and Associated Equipment*, 484(1-3):153–161, 2002. DOI: 10.1016/S0168-9002(01)02032-0.

[49] J Pfitzner. Poiseuille and his law. *Anaesthesia*, 31(2):273–275, 1976. DOI: 10.1111/j.1365-2044.1976.tb11804.x.

[50] Bosch Sensortec. *Digital pressure sensor*. May 2015. Revision 2.8.

[51] *Raspberry Pi 2 Model B*. https://www.raspberrypi.org/products/

`raspberry-pi-2-model-b/` dated 23rd Nov 2018.

[52] Agus Kurniawan. *NodeMCU Development Workshop*. PE Press, July 2015.

[53] S Mondal, VM Datar, SD Kalmani, G Majumder, NK Mondal, and B Satyanarayana. Leak rate estimation of a resistive plate chamber gap by monitoring absolute pressure. *Journal of Instrumentation*, 11(11):C11009, 2016. DOI: 10.1088/1748-0221/11/11/C11009.

[54] Suryanarayan Mondal, VM Datar, Gobinda Majumder, NK Mondal, KC Ravindran, and B Satyanarayana. Leak test of Resistive Plate Chamber gap by monitoring absolute pressure. *Journal of Instrumentation*, 14(04):P04009, 2019. DOI: 10.1088/1748-0221/14/04/P04009.

[55] Dieter Heck, G Schatz, J Knapp, T Thouw, and JN Capdevielle. CORSIKA: A Monte Carlo code to simulate extensive air showers. Technical report, 1998.

[56] Sea Agostinelli, John Allison, K al Amako, John Apostolakis, H Araujo, P Arce, M Asai, D Axen, S Banerjee, G 2 Barrand, et al. GEANT4–a simulation toolkit. *Nuclear instruments and methods in physics research section A: Accelerators, Spectrometers, Detectors and Associated Equipment*, 506(3):250–303, 2003. DOI: 10.1016/S0168-9002(03)01368-8.

[57] F Anghinolfi, P Jarron, AN Martemiyanov, E Usenko, Horst Wenninger, MCS Williams, and A Zichichi. NINO: an ultra-fast and low-power front-end amplifier/discriminator ASIC designed for the multigap resistive plate chamber. *Nuclear Instruments and Methods in Physics Research Section A: Accelerators, Spectrometers, Detectors and Associated Equipment*, 533(1-2):183–187, 2004. DOI: 10.1016/j.nima.2004.07.024.

[58] VB Chandratre, Sourav Mukhopadhyay, Menka Sukhwani, Satyanarayana Bhesette, Megha Thomas, Ravindra Shinde, and Hari Prasad Kolla. ANUSPARSH-II frontend ASIC for avalanche mode of RPC detector using regulated cascode trans-impedance amplifier. *Proceedings of the 60th DAE-BRNS Symp. on Nucl. Phys.*, 60:928–929, 2015.

[59] S Achrekar, S Aniruddhan, N Ayyagiri, A Behere, N Chandrachoodan, VB Chandratre, D Das, S Dasgupta, VM Datar, U Gokhale, et al. Electronics, Trigger and Data Acquisition Systems for the INO ICAL Experiment. In *International conference on Tech-*

nology and Instrumentation in Particle Physics, pages 291–295. Springer, 2017. DOI: 10.1007/978-981-13-1313-4_55.

[60] Richard O. Duda and Peter E. Hart. Use of the Hough transformation to detect lines and curves in pictures. *Communications of the ACM*, 15(1):11–15, 1972. DOI: 10.1145/361237.361242.

[61] Niu Li-Bo, Li Yu-Lan, Huang Meng, He Bin, and Li Yuan-Jing. Track reconstruction based on Hough-transform for nTPC. *Chinese Physics C*, 38(12):126201, 2014. DOI: 10.1088/1674-1137/38/12/126201.

[62] Zhaoyi Qu, Sadakazu Haino, Paolo Zuccon, and Minggang Zhao. New track finding based on cellar automaton for AMS-02 detector. *Nuclear Instruments and Methods in Physics Research Section A: Accelerators, Spectrometers, Detectors and Associated Equipment*, 869:135–140, 2017. DOI: 10.1016/j.nima.2017.07.007.

[63] Masaharu Tanabashi, K Hagiwara, K Hikasa, K Nakamura, Y Sumino, F Takahashi, J Tanaka, K Agashe, G Aielli, C Amsler, et al. Review of particle physics. *Physical Review D*, 98(3):030001, 2018. DOI: 10.1103/PhysRevD.98.030001.

[64] H Adarkar, SR Dugad, MR Krishnaswamy, MGK Menon, NK Mondal, VS Narasimham, BV Sreekantan, Y Hayashi, S Kawakami, N Ito, et al. A multi TeV muon bundle observed in the KGF underground detector. *Physics Letters B*, 267(1):138–142, 1991. 10.1016/0370-2693(91)90539-3.

[65] ALICE collaboration et al. Study of cosmic ray events with high muon multiplicity using the ALICE detector at the CERN Large Hadron Collider. *Journal of cosmology and astroparticle physics*, 2016(01):032, 2016. 10.1088/1475-7516/2016/01/032.

[66] The MACRO Collaboration. Multiple muon measurements with MACRO. *Proceedings, Very High Energy Cosmic Ray Interactions*, C94-07-24:711–722, 1994. hep-ex/9410001.

[67] The DELPHI Collaboration. Study of multi-muon bundles in cosmic ray showers detected with the DELPHI detector at LEP. *Astroparticle Physics*, 28(3):273–286, 2007. 10.1016/j.astropartphys.2007.06.001.

[68] V Avati, L Dick, K Eggert, J Ström, H Wachsmuth, S Schmeling, T Ziegler, A Brühl, and C Grupen. Cosmic multi-muon events observed in the underground CERN-LEP tunnel

with the ALEPH experiment. *Astroparticle Physics*, 19(4):513–523, 2003.

[69] WD Apel, JC Arteaga-Velázquez, K Bekk, M Bertaina, J Blümer, H Bozdog, IM Brancus, E Cantoni, A Chiavassa, F Cossavella, et al. Probing the evolution of the EAS muon content in the atmosphere with KASCADE-Grande. *Astroparticle Physics*, 95:25–43, 2017. 10.1016/j.astropartphys.2017.07.001.

[70] Suryanarayan Mondal, VM Datar, Gobinda Majumder, NK Mondal, KC Ravindran, and B Satyanarayana. Study of Particle Multiplicity of Cosmic Ray Events using $2\,\mathrm{m} \times 2\,\mathrm{m}$ Resistive Plate Chamber Stack at IICHEP-Madurai. *Journal of Instrumentation*, 51:17–32, 2020. DOI: 10.1007/s10686-020-09685-6.

[71] P Adamson, C Andreopoulos, KE Arms, R Armstrong, DJ Auty, S Avvakumov, DS Ayres, B Baller, B Barish, PD Barnes Jr, et al. Measurement of the atmospheric muon charge ratio at TeV energies with the MINOS detector. *Physical Review D*, 76(5):052003, 2007. DOI: 10.1103/PhysRevD.76.052003.

[72] Espen Lund, Lars Bugge, Igor Gavrilenko, and Are Strandlie. Track parameter propagation through the application of a new adaptive Runge-Kutta-Nyström method in the AT-LAS experiment. *Journal of Instrumentation*, 4(04):P04001, 2009. DOI: 10.1088/1748-0221/4/04/P04001.

[73] Rudolf K Bock, H Grote, and D Notz. Data Analysis Techniques for High-Energy Physics (Chapter 3). *Cambridge University Press*, 11, 2000.

[74] John Stuart Marshall. A study of muon neutrino disappearance with the MINOS detectors and the NuMI neutrino beam. 2008. DOI: 10.2172/935002.

[75] EJ Wolin and LL Ho. Covariance matrices for track fitting with the Kalman filter. *Nuclear Instruments and Methods in Physics Research Section A: Accelerators, Spectrometers, Detectors and Associated Equipment*, 329(3):493–500, 1993. DOI: 10.1016/0168-9002(93)91285-U.

[76] Hans A Bethe and Julius Ashkin. Experimental Nuclear Physics. *Wiley, New York*, 1953.

[77] Giulio D'Agostini. A multidimensional unfolding method based on Bayes' theorem. *Nuclear Instruments and Methods in Physics Research Section A: Accelerators, Spectrometers, Detectors and Associated Equipment*, 362(2-3):487–498, 1995. DOI: 10.1016/0168-

9002(95)00274-X.

[78] S. Mondal, S. Pethuraj, and G. Majumder. Cosmic muon momentum spectra at Madurai. In *XXIV DAE High Energy Physics Symposium*, 2020.

[79] S. Mondal, S. Pethuraj, and G. Majumder. Muon charge ratio at Madurai. (in preparation).